Electrooptical Properties of Montmorillonite Suspended in Aqueous Media

Ryo Sasai

Department of Materials Science, Faculty of Science, Hiroshima University,

1-3-1 Kagamiyama, Higashi-Hiroshima 739, Japan

— *Contents* —

page

Contents I

Abstract i

Chapter I. *General Introduction* 1

References 5

Chapter II. *Electrooptical Methods*

II. 1. Introduction 6

II. 2. Reversing-Pulse Electric Birefringence Method 9

References 13

Chapter III. *Instrumentation*

III. 1. Introduction 14

III. 2. Optical System 15

III. 3. Reversing-Pulse Generator 16

III. 4. Characterization of Reversing-Pulse Generator 19

References 20

Chapter IV. *Theory*

IV. 1. Introduction 21

IV. 2. RPEB Transient Theory 22

IV. 2. 1. Potential

IV. 2. 2. Diffusion Equation in Orienting Field

IV. 2. 3. RPEB Expressions in the Kerr-Law Region

IV. 2. 4. Theoretical Curves of Newly Derived Theory

IV. 2. 5. Comparison with Experimental RPEB Signal

IV. 3. Orientation Function 33

IV. 3. 1. Electric Moments

IV. 3. 2. Orientation Function

IV. 3. 3. General Behavior of PD-SUSID Orientation Function
IV. 3. 4. Two Limiting Cases of Field Orientation
IV. 3. 5. Comparison with Experimental Data of Montmorillonite
IV. 4. Rotational Relaxation 51
References 53

Chapter V. Effect of Particle Concentration, Ionic Strength, and Valence of Electrolyte on Electrooptical Properties of Montmorillonite Particles in Aqueous Media
V. 1. Introduction 55
V. 2. Experimental 56
V. 2. 1. Preparation of Montmorillonite Suspension
V. 2. 2. Electron Microscopic Photogragh of Montmorillonite Particles
V. 3. Na-montmorillonite Suspensions 57
V. 3. 1. Reversing Transient Signals
V. 3. 2. Field-Strength Dependence of Steady-State Electric Birefringence
V. 3. 3. Comparison with RPEB Theoretical Curves
V. 3. 4. Field-Strength Dependence of $<\tau>_{EB}$
V. 3. 5. Effect of Particle Concentration and Ionic Strength on the Diameter
V. 4. Mg-montmorillonite Suspensions 67
V. 4. 1. RPEB Signals
V. 4. 2. Field-Strength Dependence of Steady-State Electric Birefringence
V. 4. 3. Field-Strength Dependence of $<\tau>_{EB}$
References 72

Chapter VI. Conclusions 73

Acknowledgements 75

— *Abstract* —

To clarify the electrooptical property of clay particle suspended in aqueous media with a reversing-pulse electric birefringence (RPEB) method, the new RPEB transient theories and orientation function were derived, and the reversing pulse generator, which is also applicable to large particle such as clay, was newly constructed. The transient RPEB theory was derived on the basis of the interaction of applied electric pulse with two electric dipole moments of the macroion: one is due to the ion-atmosphere polarizability α_3 with a single relaxation time τ_1 for the distortion of ion-atmosphere along the longitudinal axis and the other is due to the intrinsic molecular (instantaneously field-induced) polarizability anisotropy $\Delta\alpha'$ ($= \alpha_{33} - \alpha_{11}$) between the longitudinal (3) and transverse (1) axes of the macroion. The new orientation function was derived for disklike model. It was assumed that the disklike particle possessed the following three electric dipole moments: (1) permanent dipole moment, (2) saturable induced dipole moment, which is induced in a finite time and saturated at an electric field strength, and (3) unsaturable induced dipole moment, which is instantaneously induced dipole moment by an external electric field. In the newly constructed reversing pulse generator, a field-effect transistor (MOS-FET) was used instead of a vacuum tube as the switching element. This pulse generator has the following characteristics: (1) a stable output voltage in the 5—300V range, (2) a widely variable output pulse duration in the 10 μs—1.2 s range, and (3) a very short time constant of electric pulse (in most cases, 150 ns for buildup and reverse and 50 ns for decay). Moreover, this generator could deliver a single rectangular pulse and/or a reversing pulse to high-ionic strength samples, e.g., 0.2 moldm^{-3} NaCl or $MgCl_2$, because of a high electric current resistance of MOS-FET. The theories and reversing pulse generator newly developed were applied to study the effects of particle concentration, the ionic strength, and valence of electrolyte on the electrooptical and hydrodynamic properties of montmorillonite particles suspended in aqueous media. It was clear that both these theories and generator were very useful for the study of clay particle suspended in aqueous media. RPEB data of Na-montmorillonite particle indicated that the particle possesses no *permanent dipole moment*, but an *ionic polarization* makes a large contribution to the field orientation. Since the contribution of the *ionic polarization* increased with an increase of ionic strength, the distortion of sodium ions trapped on the cation-exchangeable sites may be responsible for this *ionic polarization*. The Na-montmorillonite particles form aggregates of *card-house structure*, which is an irregular structure, at increased concentrations of added sodium ions, since the optical anisotropy decreases and the diameter of particle increases with increasing ionic strength of added sodium ions. In contrast to the Na-montmorillonite particle, the RPEB

signals of Mg-montmorillonite suspensions showed longer average rotational relaxation times, and the optical anisotropy of Mg-montmorillonite particle increased with an increase in concentrations of added magnesium ions. Moreover, the RPEB signals could not be analyzed theoretically. Therefore, Mg-montmorillonite particles form larger aggregates of *book-house structure*, which is a regular structure.

The present study has confirmed that the reversing-pulse electrooptical methods are very useful to characterize the structure and properties of clay particles. These findings give us some fundamental information for application of clay particles. In the future, the analysis methods of reversing-pulse electric birefringence newly developed in this study will be successfully extended to many colloidal particle systems other than clay particles.

— *Chapter I.* —
General Introduction

Clay minerals are silicate minerals, whose diameter is less than ca. 2 μm, created by weathering of rocks and/or in the process of soil formation.[1,2] The structure of clay minerals is composed of the unit structure, which is defined as the combinations of tetrahedral layer of silicate and octahedral layer of $Mg(OH)_2/Al(OH)_3$, as shown Figure I-1[1,2]. Montmorillonite

(a) Tetrahedral layer of Silica

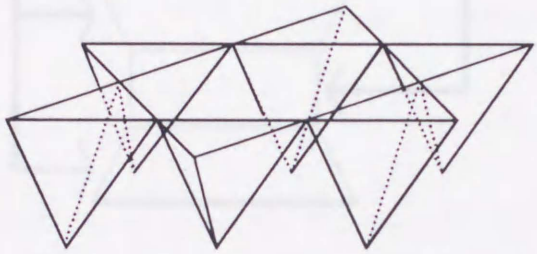

(b) Octahedral layers ($Mg(OH)_2$ and/or $Al(OH)_3$)

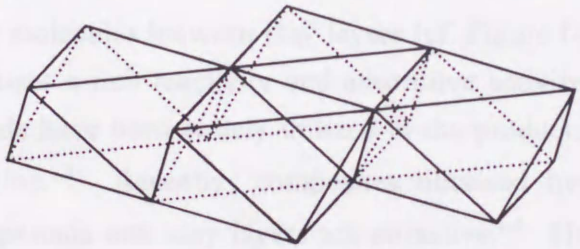

Figure I-1. Constitutive elements of clay mineral. (a) A silicon atom is located at the center of tetrahedron and an oxygen at each corner. (b) A magnesium and/or aluminium atom is located at the center of octahedron and a hydroxyl group or oxygen at each corner.

particle used in the present study is a kind of 2:1 type clay mineral, in which an octahedral layer is located between two tetrahedral layers (cf. Figure I-2). Clay minerals plasticize by the heat drying, or disperse as stable colloid particles in aqueous media.[1,2] The surface of clay minerals has negative charges because of isomorphous cation substitution of the tetra- and octahedral layers, i.e., $Si^{4+} \rightarrow Li^+$ (in the tetrahedron), $Al^{3+} \rightarrow Mg^{2+}$, Fe^{2+}, and $Mg^{2+} \rightarrow Li^+$ (in the octahedron).[1,2] To compensate the lack of positive charge, various cations (Na^+, K^+, Ca^{2+}, and so on) are adsorbed onto clay layers. Then, clay minerals are well known as a kind of cation-exchangeable inorganic polymers.[1-3] The present montmorillonite particle holds exchangeable

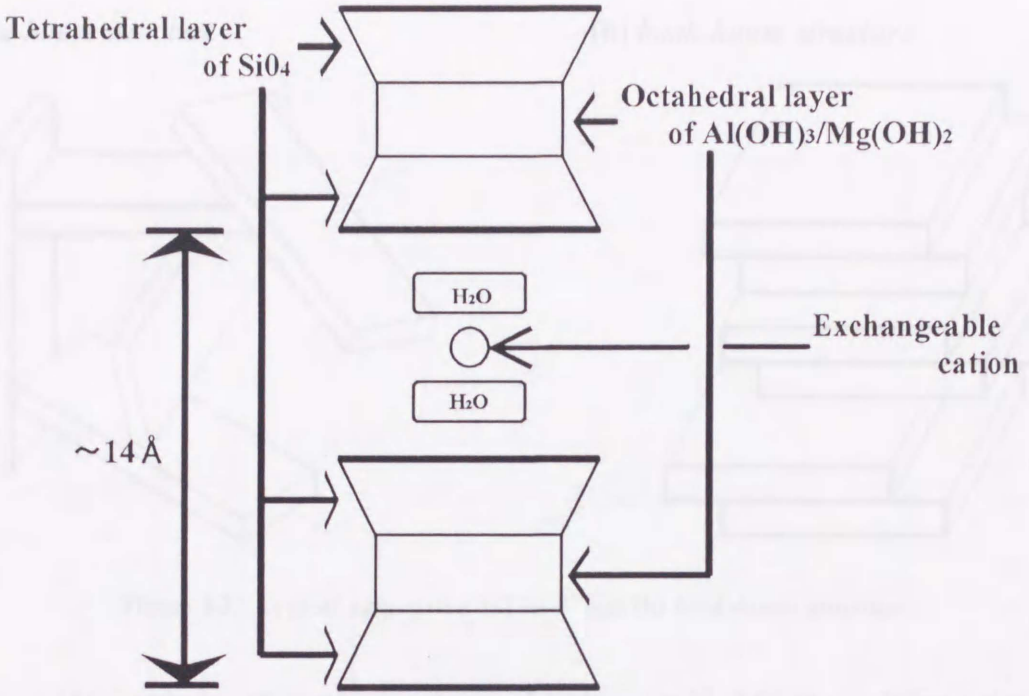

Figure I-2. Schematic montmorillonite layers structure composed of two a octahedral and two octahedral layers.

cations and a few H_2O molecules between clay layers (cf. Figure I-2). Therefore, the surface of clay minerals possesses a rich reactivity and adsorptive activity. Because of these novel properties, clay minerals have been widely utilized in the products such as ceramics, paints, cosmetics, and medicine.[1,2] Recently, composites obtained by intercalation of various organic/inorganic compounds into clay layers are attractive.[1-4] The intercalated compounds display various unique reactions and properties, e.g., photochemical reaction and photochroism. Therefore, new functional materials could be developed by selecting the molecules intercalated into clay minerals.[3,4]

Clay itself displays a lot of interesting phenomena, too, e.g., swelling, aggregation (*card-* and *book-house structure*: cf. Figure I-3), and gelation.[1-3,5] Details of these phenomena and properties of clay as such, however, have not been clear enough yet. Physicochemical methods will help us to understand these phenomena and properties. X-ray diffraction, nuclear magnetic resonance, and thermal analyses have been performed for powder states or concentrated dispersion, but have not been studied for diluted dispersion, in which properties of clay as such are remarkable.[1-3,5] Electrooptical method used in this study makes it possible to study clay minerals in diluted dispersions. Since dispersed particles are oriented by an electric field and an anisotropy of the particle is detected in the electrooptical method, this method yields more useful information on the electrical and optical properties of dispersed

(a) *card-house structure* (b) *book-house structure*

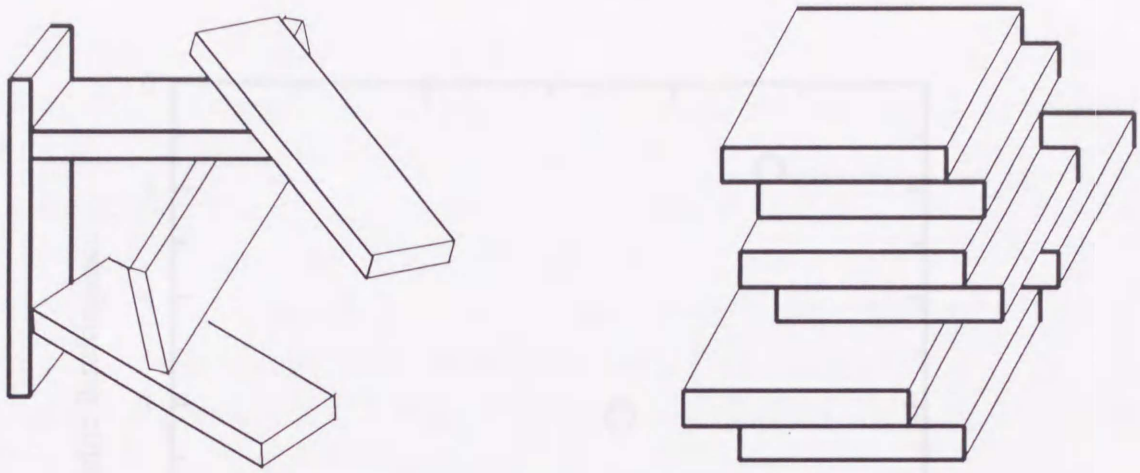

Figure I-3. Typical aggregates: (a) *card-* and (b) *book-house structure*.

particle, unobtainable by other physicochemical techniques.[6,7] Moreover, information of ion atmosphere and electric double layer around particle, and structure of particle can be obtained by this electrooptical method.[6,7] The electrooptical study of clay minerals in aqueous media was started by O'Konski and Zimm with a dc electric field.[8] They carried out an electric birefringence measurement of montmorillonite particle dispersed in aqueous media, and found that a sign of steady-state electric birefringence reverses from negative to positive with increasing field strengths (cf. Figure I-4).[8] Shah *et al.* have explained this phenomenon by assuming the out-of-plane transverse *permanent dipole moment* in the disklike particle.[9] From the electric birefringence measurements with samples at various concentrations and diameters of particles, Yoshida *et al.*, however, suggested that the particle possessed no such transverse *permanent dipole moment*.[10] It is not clear what the sign inversion phenomenon is responsible for. Clarifying this phenomenon should give an insight into the electrooptical properties of montmorillonite particle. However, the experimental application of electrooptical method for clay minerals dispersed in aqueous media was slow, because there are no reversing pulse generators for large size particles and theories for enough analyzing experimental data. An author carried out the construction of the reversing pulse generator applicable to large size particles such as clay minerals (details will be given in ***Chapter III.***) and derivations of theories for analyzing experimental data of disklike particles dispersed in aqueous media (details will be given in ***Chapter III.***).

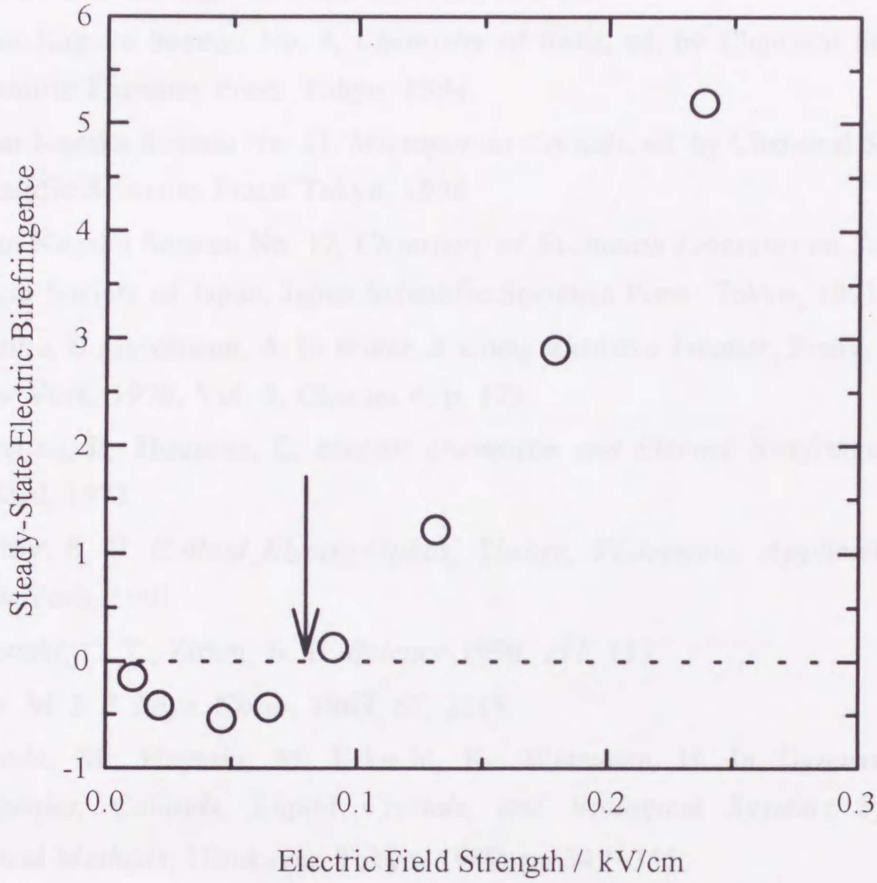

Figure I-4. Electric field strength dependence of the steady-state electric birefringence of montmorillonite dispersed in aqueous media. Symbols are experimental data. Arrow indicates the electric field strength where the sign of the steady-state electric birefringence reverses.

In the present study, the reversing-pulse electric birefringence (hereafter abbreviated as RPEB) was applied to montmorillonite dispersed in aqueous media for making clear the following problems by using this apparatus and these theories.

1. Origin of the sign reversal of steady-state electric birefringence from negative to positive which occurs on increasing field strengths.

2. Electrical, optical, and hydrodynamic properties of montmorillonite dispersed in aqueous media.

3. Effects of particle concentration, and ionic strength and valence of added salts on the field orientation of montmorillonite particles dispersed in aqueous media.

References

1. *Clay Handbook*; Giho-do Co., Ltd.: Tokyo, 1976.

2. Kikan Kagaku Sosetsu No. 4, *Chemistry of Soils*, ed. by Chemical Society of Japan, Japan Scientific Societies Press: Tokyo, 1994.

3. Kikan Kagaku Sosetsu No. 21, *Microporous Crystals*, ed. by Chemical Society of Japan, Japan Scientific Societies Press: Tokyo, 1994.

4. Kikan Kagaku Sosetsu No. 12, *Chemistry of Excitation Processes on Solid Surface*, ed. by Chemical Society of Japan, Japan Scientific Societies Press: Tokyo, 1991.

5. Forslind, E.; Jacobsson, A. In *Water, A Comprehensive Treatise*; Frank, F., Ed.; Plenum Press: New York, 1978; Vol. 5, Chapter 4, p. 173.

6. Fredericq, E,; Houssier, C. *Electric Dichroism and Electric Birefringence*; Clarendon Press: Oxford, 1973.

7. Stoylov, S. P. *Colloid Electro-Optics*: *Theory, Techniques, Applications*; Academic Press: New York, 1991.

8. O'Konski, C. T.; Zimm, B. H. *Science* **1950**, *111*, 113.

9. Shah, M. J. *J. Phys. Chem.* **1963**, *67*, 2215.

10. Yoshida, M.; Hayashi, M; Kikuchi, K.; Watanabe, H. In *Dynamic Behavior of Macromolecules, Colloids, Liquid Crystals, and Biological Systems by Optical and Electrooptical Methods*; Hirokawa: Tokyo, 1989; pp 349–355.

— Chapter II. —
Electrooptical Method

II. 1. Introduction

The optical anisotropy of a particle as such cannot be observed in solvent systems because of Brownian motion of particles, even if particle itself possesses the optical anisotropy (cf. Figure II-1-1a). However, if a particle possesses the electrical anisotropy, i.e., permanent

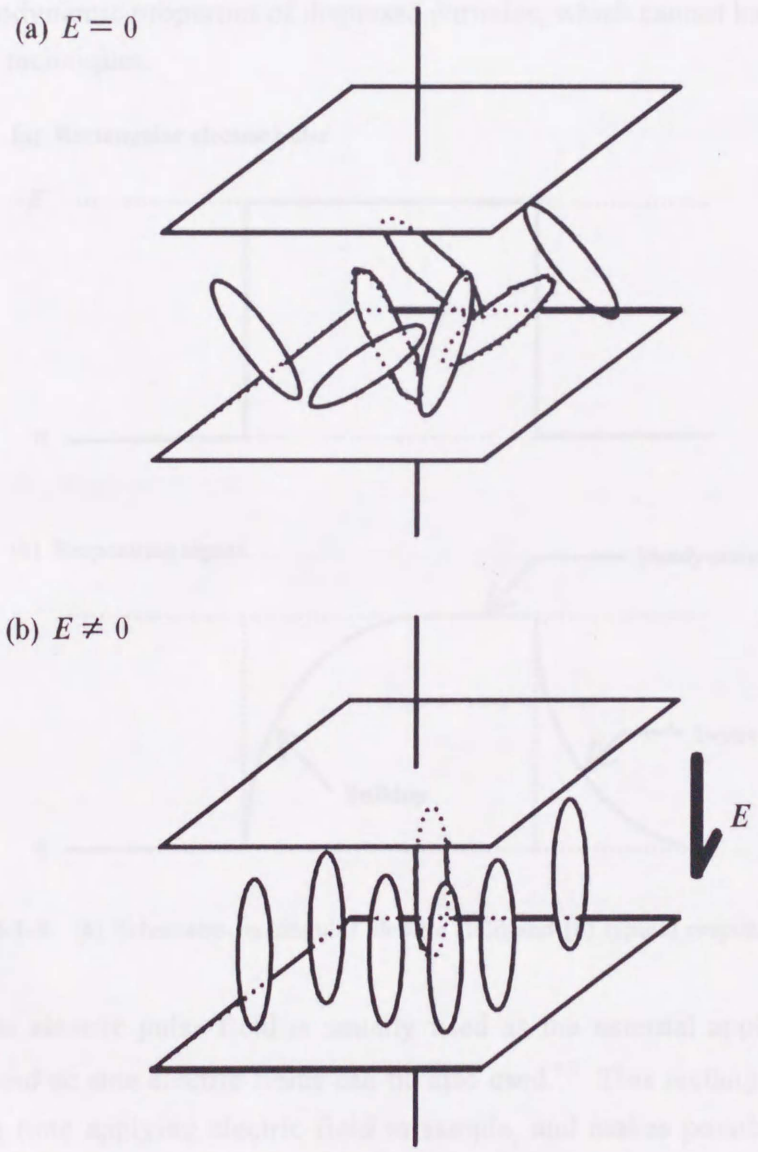

Figure II-1-1. Schematic field orientation behavior of particle with electric anisotropy. (a) $E = 0$ and (b) $E \neq 0$.

dipole moment and electric dipole moment induced by an external field, then the particle is oriented parallel to the direction of applied external electric field (Figure II-1-1b). Then, various types of anistropic properties can be observed. The optical anisotropy induced by applying an external electric field is called the electrooptical effect.[1,2] When particles have the anisotropy of the optical polarizability, there appears the difference between refractive indices parallel ($n_{\parallel}$) and perpendicular ($n_{\perp}$) to the direction of applied field. This difference is *electric birefringence* Δn ($= n_{\parallel} - n_{\perp}$).[1,2] The difference of absorption is called *electric linear dichroism* ΔA ($= A_{\parallel} - A_{\perp}$), and the difference of intensity of light scattering is called *electric light scattering* ΔI ($= I_{\parallel} - I_{\perp}$).[1,2] These parameters yield useful information on the electric, optical, and hydrodynamic properties of dispersed particles, which cannot be obtained by other physicochemical techniques.

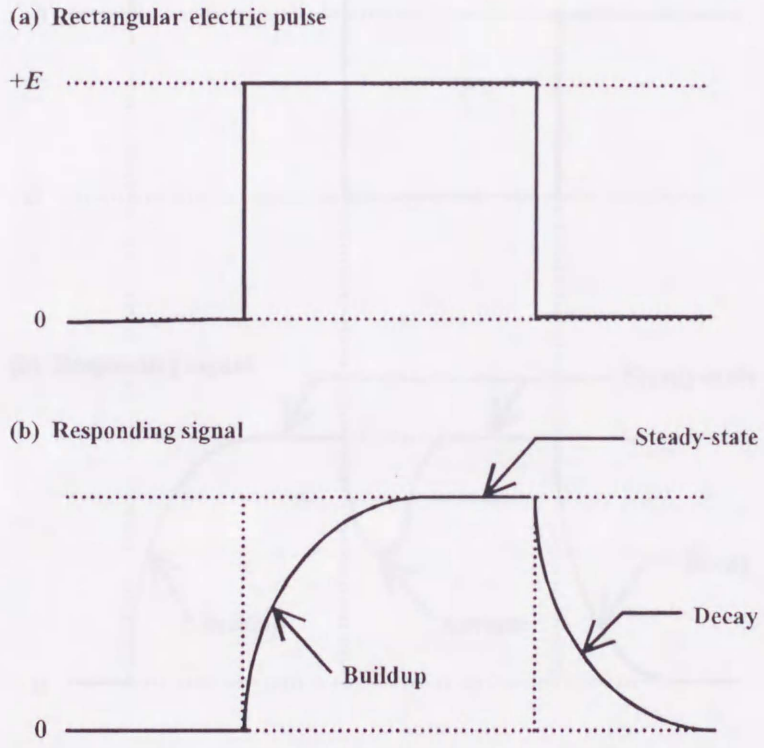

Figure II-1-2. (a) Schematic rectangular electric field and (b) typical response signal.

The rectangular electric pulse field is usually used as the external applied electric field, though dc static and ac sine electric fields can be also used.[1,2] This rectangular electric pulse can minimize the time applying electric field to sample, and makes possible the analysis of transient phenomenon. When the rectangular electric pulse is applied to sample, the obtained electrooptical signal changes with the passage of time as shown in Figure II-1-2. This

response signal is divided into three parts, i.e., buildup process, steady-state, and decay process. O'Konski and Pytkowicz used a reversing-pulse electric field, which is a consecutive pulse with a positive- and negative-going polarity, as the applied electric field.[3] The response signal against the reversing-pulse electric field is shown in Figure II-1-3. This transient signal contains some informations on the electric dipole moments of particle in a reverse process because of instantaneous change of polarity of electric pulse.

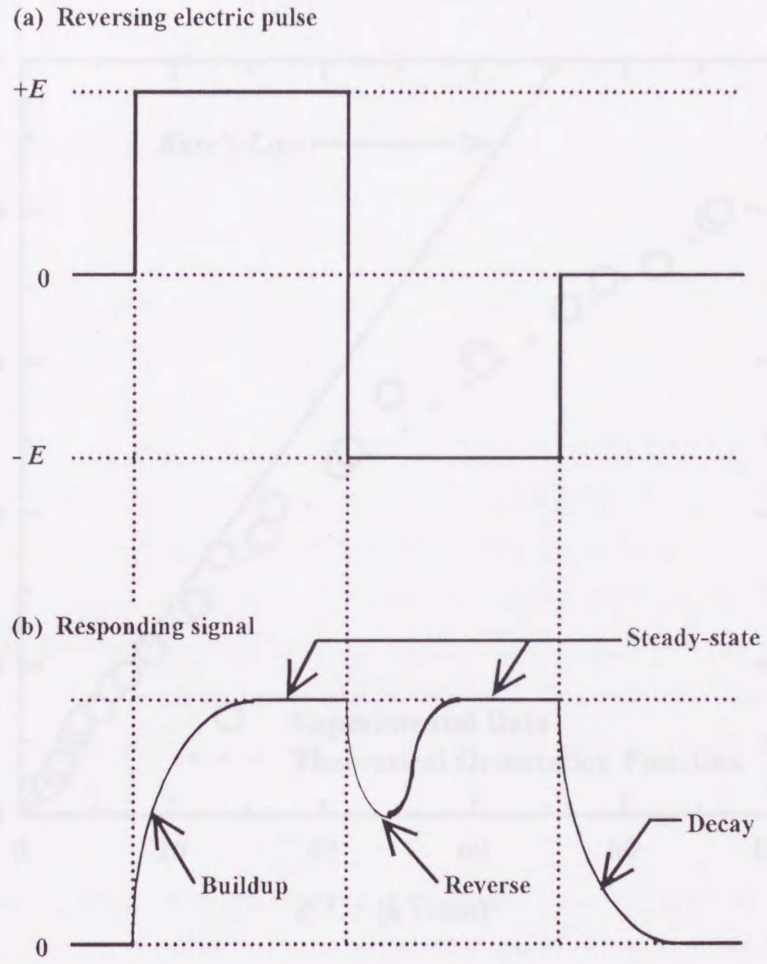

Figure II-1-3. (a) Schematic reversing electric pulse and (b) typical response signal.

II. 2. Reversing-Pulse Electric Birefringence Method

The Δn value is in proportion to the second power of electric field strength E at low electric fields. This behavior is called *Kerr's law* (cf. Figure II-2-1).[1,2] In this theory, the Δn is related

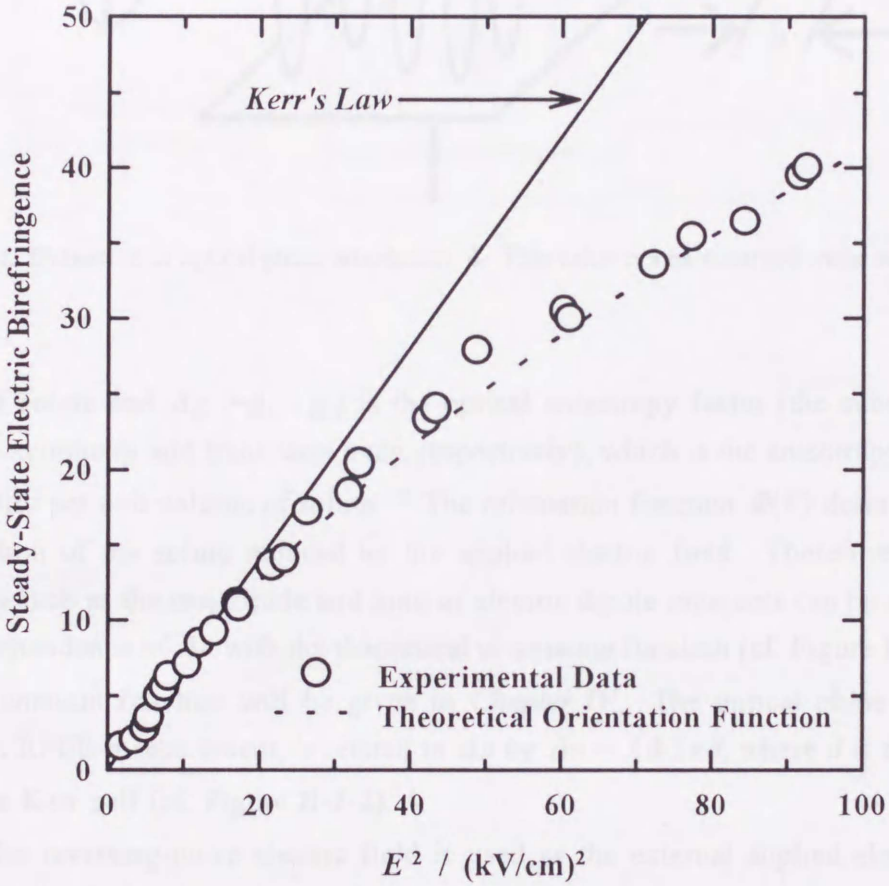

Figure II-2-1. Field-strength dependence of steady-state electric birefringence. Symbols are experimental data. Solid line shows *Kerr's law*. Broken line is theoretical orientation function.

to E by $\Delta n = KnE^2 = B\lambda E^2$, where n is the refractive index in the absence of electric field, λ is the wavelength of incident light, and K (or B) is a Kerr constant.[1,2] When the E value becomes high, however, the electric field strength dependence of Δn cannot be explained with *Kerr's law* (cf. Figure II-2-1). Considering the difference between *Kerr's law* and the experimental data, the Δn is expressed as $\Delta n = 2\pi C_v \Delta g \times \Phi(E)/n$, where C_v is the volume

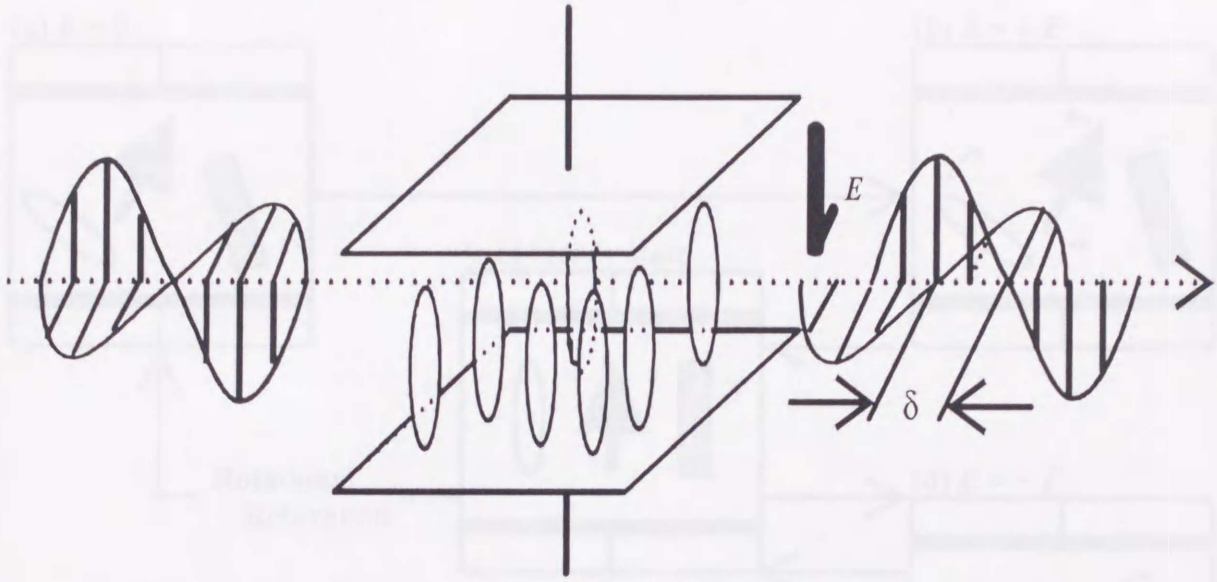

Figure II-2-2. Definition of optical phase retardation, δ. This value can be observed when the external field is applied.

fraction of solute and Δg ($=g_3 - g_1$) is the optical anisotropy factor (the subscripts 3 and 1 denote the symmetry and transverse axes, respectively), which is the anisotropy of the optical polarizability per unit volume of solute.[1,2] The orientation function $\Phi(E)$ describes the degree of orientation of the solute induced by the applied electric field. Therefore, the electrical parameters such as the magnitude and kind of electric dipole moments can be estimated from the field dependence of Δn with the theoretical orientation function (cf. Figure II-2-1). Details on the orientation function will be given in ***Chapter IV***. The optical phase retardation δ, detected in RPEB measurement, is related to Δn by $\Delta n = \lambda\delta/2\pi d$, where d is the optical path length of a Kerr cell (cf. Figure II-2-2).[1,2]

When the reversing-pulse electric field is used as the external applied electric field, the response signal shows the various patterns depending on the kind of electric dipole moment of solute. Figure II-2-3 shows the behavior of solutes with various electric dipole moments under the reversing-pulse electric field. Solutes shown by each symbol in Figure II-2-3 possess the following electric dipole moments; (1) the instantaneously field-induced electric dipole moment(ellipsoid), for which the electronic polarizability is responsible, (2) permanent dipole moment (thick arrow), and (3) the electric dipole moment induced in a finite time (rectangle), which is caused by ionic polarizability. When the electric field is applied to solution, the solute having the electrical anisotropy is oriented to the direction of electric field and the orientation of solute reaches to the steady state. When the polarity of electric field is reversed, some different behaviors are observed by each electric dipole moment. (1) Solute

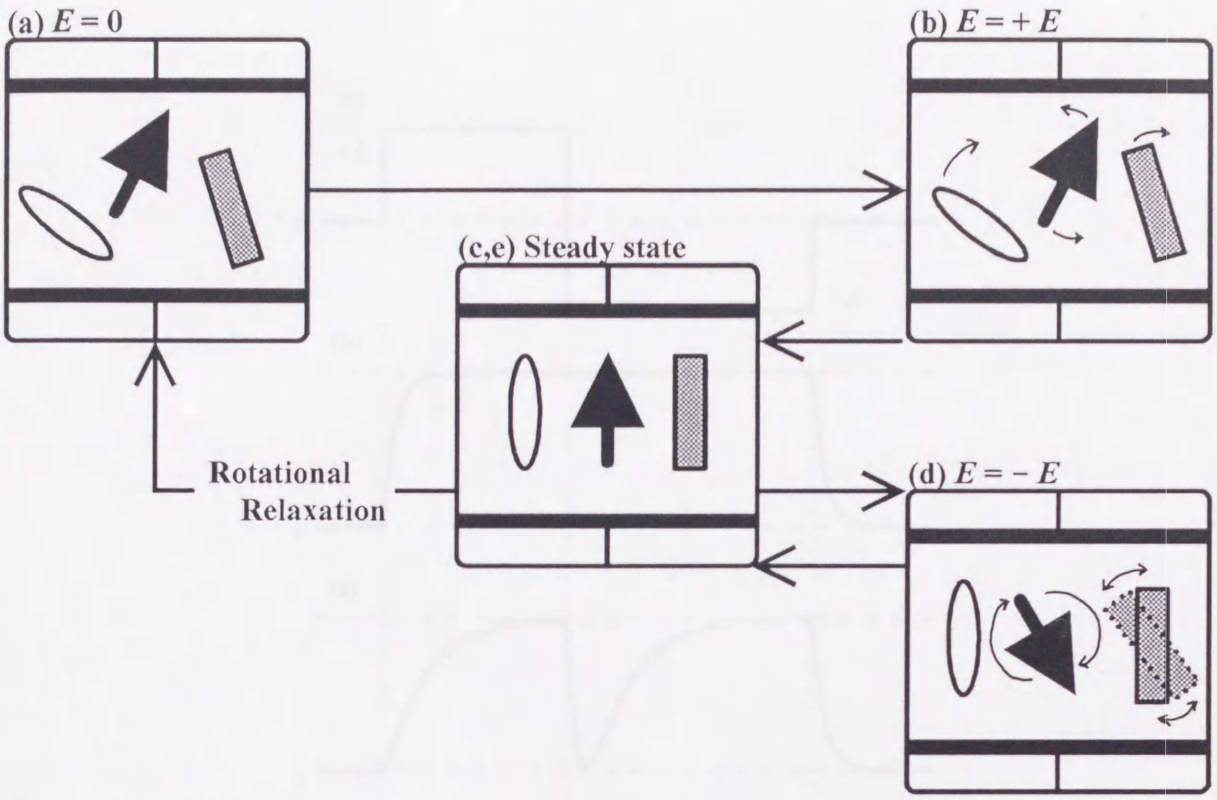

Figure II-2-3. Behavior of solutes with various electric moments against reversing-pulse electric field. Arrow shows solutes with permanent dipole moment. Ellipse displays solutes with instantaneously induced dipole moment (time independence). Rectangle presents solutes with time-dependent induced dipole moment.

itself is not moved by the electric field because the direction of electric dipole moment can be instantaneously reversed.[1,2] (2) Since the configuration of solute is responsible for the permanent dipole moment, the solute as such rotates with inversion of the polarity of the electric field.[1,2] (3) Solute itself starts to rotate as soon as the polarity of electric field changes. Since this induced dipole moment possesses a finite relaxation time, the direction of this moment reverses and the rotation of the particle is restrained.[1,2] After that, all of solutes reach to the steady state. When the electric field is instantaneously removed, the solute displays the rotational relaxation phenomenon. Figure II-2-4 shows the typical response signals of solute with the dipole moments (1), (2), and (3), respectively. The signal of solute-(1) has no change in reverse region (cf. Figure II-2-4b) because of instantaneous inverse of the direction of the induced dipole moment.[1,2] The signals of solute-(2) and -(3) have a dip in the reverse region (cf. Figure II-2-4c, d). The dip of signal (c) is very deep and approaches to baseline. This behavior indicates that the solute rotates with reversing the polarity of electric pulse field.[1,2] In Figure II-2-4d, the dip is shallower than that of (c), indicating the

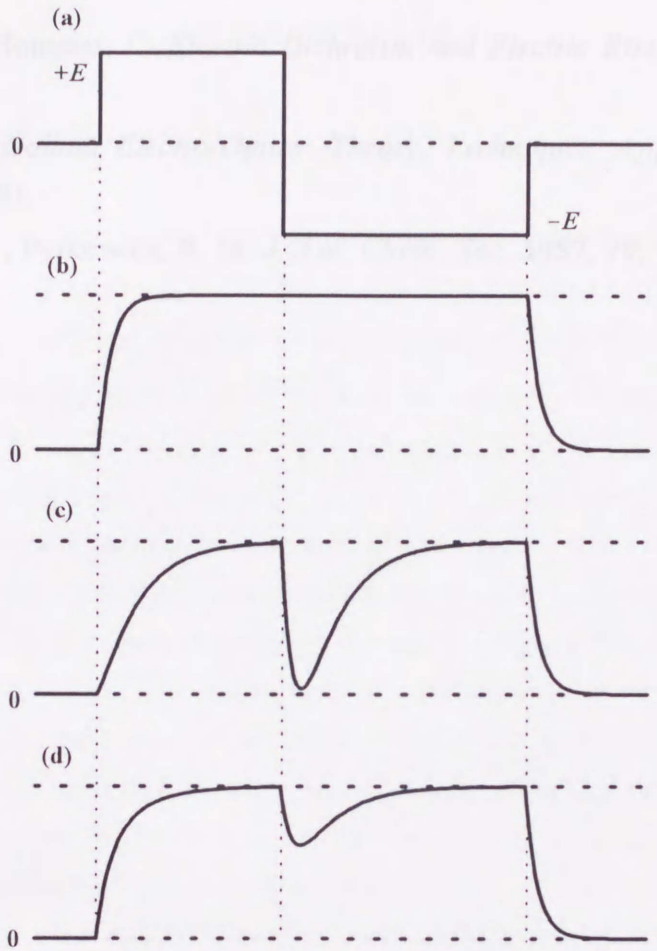

Figure II-2-4. Typical response signals of solute with various electric moments to reversing electric pulse. (a) Schematic reversing electric pulse and (b—d) responding signals.

presence of the electric dipole moment induced in a finite time.[1,2] The field-off signals are expressed by exponential curves.[1,2] Details on the field-off signals will be given in ***Chapter IV***.

EB measurement with reversing-pulse electric field gives electrical properties of solutes. In practice, solutes possess a few kinds of electric dipole moment. Therefore, some theory is necessary for extracting independently each electric dipole moment. These theories will be given in ***Chapter IV***.

References

1. Fredericq, E.; Houssier, C. *Electric Dichroism and Electric Birefringence*; Clarendon Press: Oxford, 1973.

2. Stoylov, S. P. *Colloid Electro-Optics: Theory, Techniques, Applications*; Academic Press: New York, 1991.

3. O'Konski, C. T.; Pytkowicz, R. M. *J. Am. Chem. Soc.* **1957**, *79*, 4815.

— *Chapter III.* —

Instrumentation

III. 1. Introduction

The apparatus for the electric birefringence measurement is constructed of two parts, i.e., *optical* and *electrical systems*.[1] The *optical system* consists of sample cell, to which the electric field can be applied, and detector.[1] The *electrical system* is constituted of the electric pulse generator applying the electric pulse field to the sample.[1] These parts are controlled by the personal computer.[2,3] In the electric pulse generator, an ideal electric field pulse should satisfy the following conditions: (1) the production of a wide and continuously variable pulse voltage, (2) the short time constants for an output electric field pulse at buildup, reverse, and decay, (3) the continuously variable pulse duration over a wide time scale, (4) the application of an electric field pulse to high-conductivity samples, and (5) the easy generation of a reversing-electric pulse form. The electrooptical measurement is often performed on an apparatus which fulfills only some of the above-mentioned conditions. The switching of electric pulses is usually achieved by vacuum tubes in a reversing-pulse generator.[2] This apparatus is quite effective for the output of the high-voltage electric pulse but practically ineffective for the low-output voltage electric pulse.

It is difficult to produce a well-defined short-width field pulse with a vacuum-tube pulse generator.[2] The transient signal from a sample solution involving particles of small hydrodynamic size is always influenced by the instrumental time constant of comparable magnitudes. Moreover, the pulse field results in sagging, when a long-width field pulse is applied; this is a severe drawback for measuring the large-size particles. The single-square wave line-pulse generator[4] can deliver a field pulse with a short time constant to the sample, suitable for the high-field short-duration pulse, and can be applied to samples having a high-conductivity. However, the line pulser as well as vacuum-tube pulser is not convenient for the long-duration reversing pulse for the measurement of large particles such as clays and biocolloids, because an extremely low-field strength and long-width field pulse must be employed to measure the transient electrooptical effect, which is often saturated in the low field region ($\leq$ 1 kV/cm).[5-8] Therefore, a new reversing-pulse generator, which field effect transistor is used, should be designed to be applicable for large-size particles in aqueous media.[3] In this ***Chapter***, the RPEB measurement apparatus will be introduced together with the newly constructed reversing pulse generator.

III. 2. Optical System

Figure III-2-1 shows the block diagram of optical system of RPEB instrument. An NEC GLG5350 5mW He-Ne gas laser is used as the light source. The polarization plane of the incident light beam is oriented at 45° relative to the direction of the applied electric field by a polarizer. The elliptically polarized light generated by a sample solution passes through a quartz quarter-wave plate and an analyzer, to a Hamamatsu R1398 head-on type photomultiplier. The photoelectric current is amplified by an operation amplifier and detected with a digital TCDE-4000 two-channel wave memory (Riken Denshi Co., Tokyo). The signals are accumulated and stored in a microcomputer. Kerr cell with electrodes, which are made of stainless steel, is a cylindrical and demountable type.[2] The optical path length is 4 cm and the electrode gap is 0.443 cm, allowing us to detect a weak signal at extremely low fields. The detailed description of the optical system is given elsewhere.[1-3]

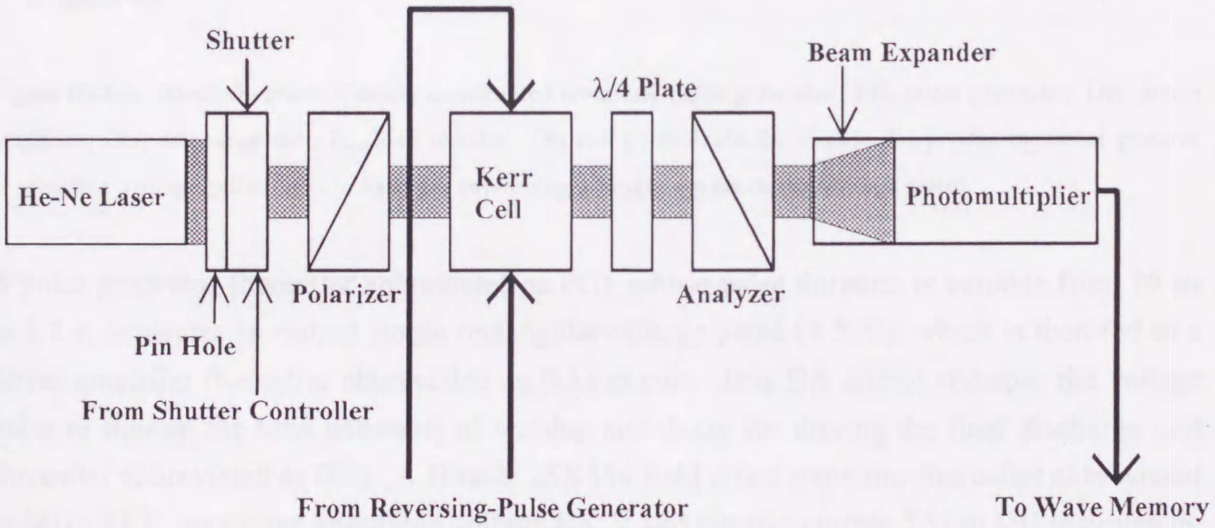

Figure III-2-1. Block diagram of optical system of reversing-pulse electric birefringence apparatus.

III. 3. Reversing-Pulse Generator

Figure III-3-1 shows the block diagram of a newly constructed reversing-pulse generator.

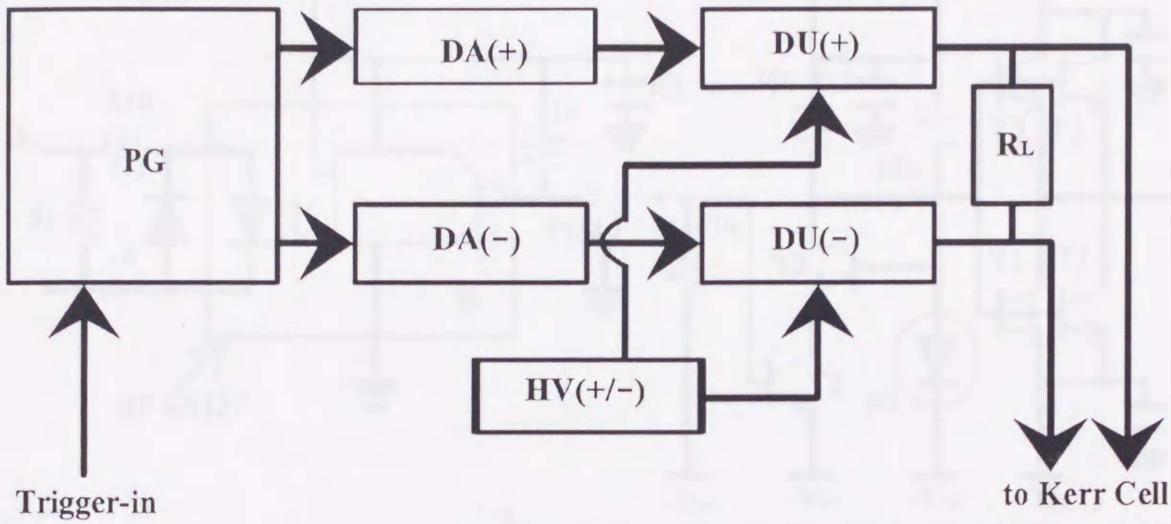

Figure III-3-1. Block diagram of newly constructed reversing-pulse generator. PG, pulse generator; DA, driver amplifier; DU, discharge unit; R_L, load resistor. (+) and (-) indicate the circuits for producing either positive or negative voltage pulse. (+) is used for producing a single square-wave voltage pulse.

A pulse generator (hereafter abbreviated as PG), whose pulse duration is variable from 10 μs to 1.2 s, generates an output single rectangular-voltage pulse (+ 5 V), which is then fed to a driver amplifier (hereafter abbreviated as DA) circuit. This DA circuit reshapes the voltage pulse to shorten the time constants of buildup and decay for driving the final discharge unit (hereafter abbreviated as DU). A Hitachi 2SK534 field effect transistor (hereafter abbreviated as MOS-FET: maximum endurable voltage 800 V and electric-current 5A) in DU is driven by an output single rectangular pulse from DA. The DU generates a high-voltage single square pulse at the same voltage, as supplied from the DC stationary-voltage power supply (hereafter abbreviated as HV). This new reversing-pulse generator can generate not only a single rectangular-voltage pulse but also a reversing-voltage pulse, with an instantaneous polarity reversal. The reversing pulse is generated as follows. The PG generates two independent single-rectangular voltage pulses of the same polarity, in which the second output single-square voltage pulse fed to DA(−) is delayed exactly by the pulse duration of the first and generated. This two voltage pulses are fed to the DA(+) and DA(−) and are transformed to voltage pulses with different polarities in the DU(+) and DU(−). The output voltage pulses with different polarities are combined at a load resistor (R_L) to deliver a reversing voltage

pulse to the Kerr Cell.

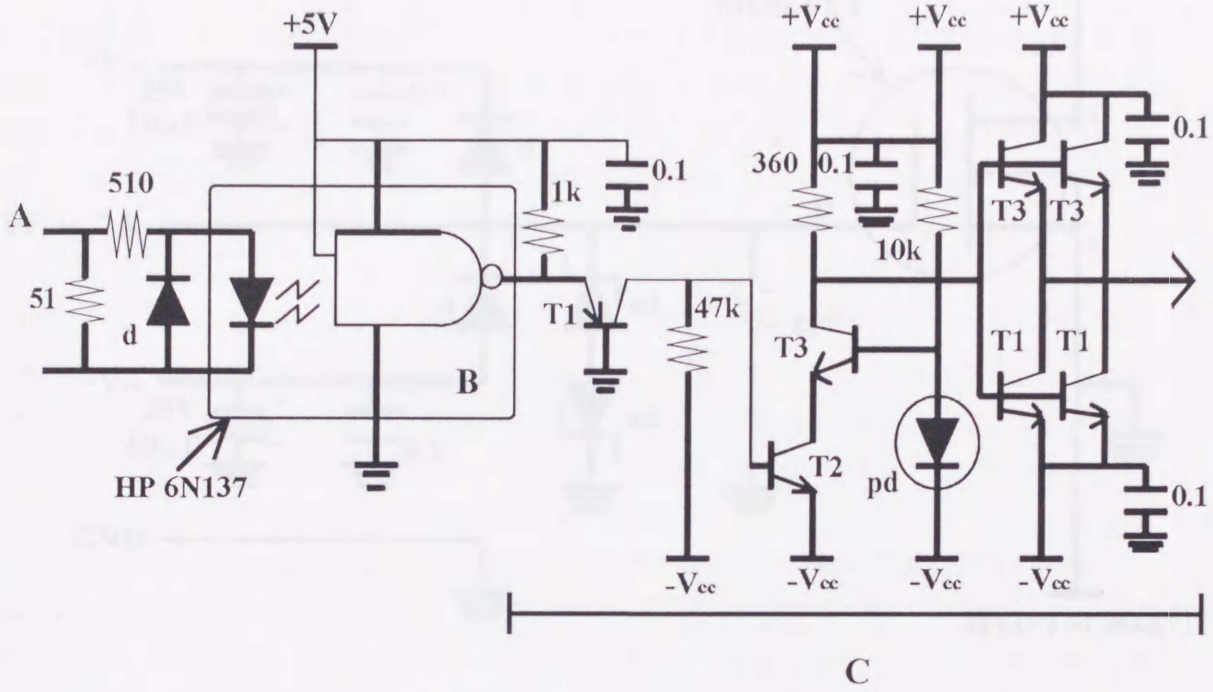

Figure III-3-2. Driver amplifier circuit. Element B photocupler HP 6N137 separates circuit A from the remaining circuit C electrically. Two identical units are needed for generating a reversing pulse of opposite polarities. d, diode; pd, photodiode; T, transistor (T1, SA1160; T2, SC1815; T3, SC2500); zd, Zener diode. The resistance is in Ω, unless otherwise stated. The capacity is in microfarads, unless otherwise stated.

Figure III-3-2 shows the detailed circuitry of DA. An input voltage pulse (+ 5 V) is electrically isolated from PG by element B, a photocoupler (HP 6N137), to shut out electric noise from PG entering the DA unit for stable high-speed response. The rectangular voltage pulse is amplified and reshaped, and the rectangular output pulse with a magnitude higher than + 10 or − 10 volts is produced for driving DU. Figure III-3-3 shows the detailed circuitry of DU. The HV always supplies the high voltage to the *drain* (D of Figure III-3-3) of MOS-FET. When a driver pulse from DA is fed to the *gate* (G of Figure III-3-3) of MOS-FET, the rectangular pulse, which had the same voltage as that of HV, supplies to R_L from the *source* (S of Figure III-3-3) of MOS-FET.

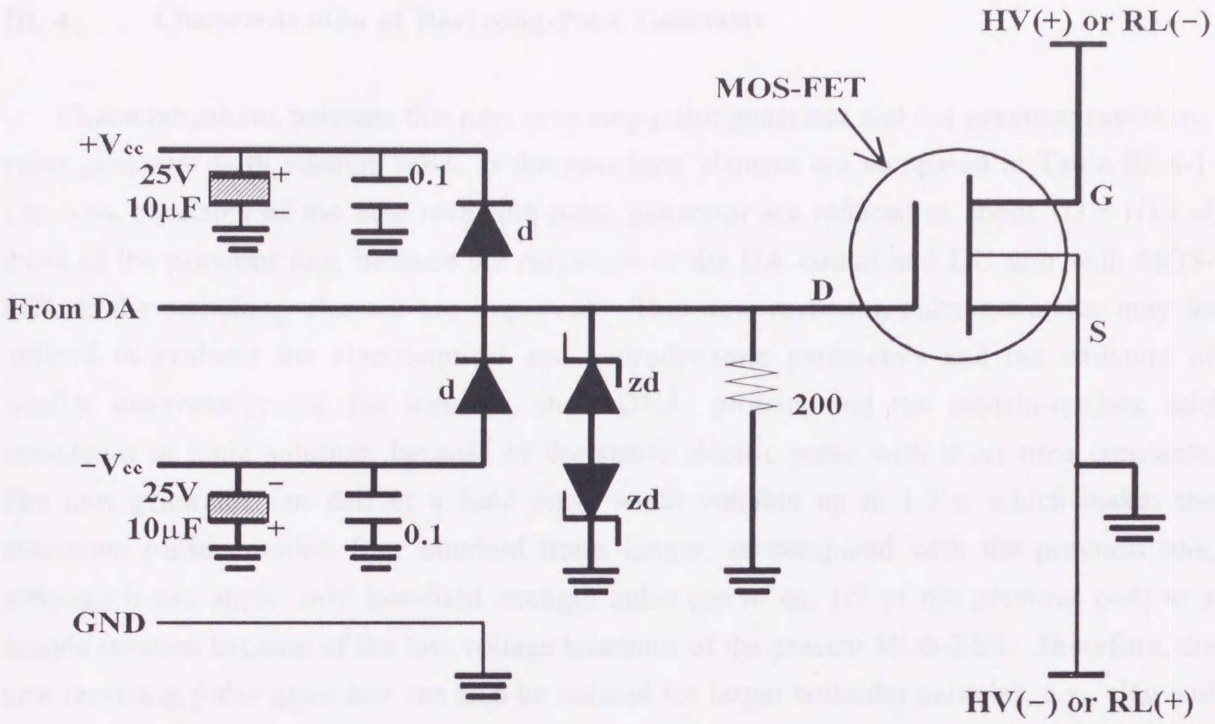

Figure III-3-3. MOS-FET is used as a switching element. When a single square-wave pulse is produced from this pulse generator, the (+) unit is used (HV(+)—R_L(+) in combination). When the reversing pulse is produced from this pulse generator, two discharge units must be used simultaneously (HV(+)—R_L(+) and HV(-)—R_L(-) in combinations). A Kerr cell is connected parallel to R_L. HV: the high-voltage direct-current power supply. d, diode; pd, photodiode; T, transistor (T1, SA1160; T2, SC1815; T3, SC2500); zd, Zener diode. The resistance is in Ω, unless otherwise stated. The capacity is in microfarads, unless otherwise stated.

III. 4. Characterization of Reversing-Pulse Generator

Characterizations between this new reversing-pulse generator and our previous reversing-pulse generator with vacuum tubes as the switching element are compared in Table III-4-1. The time constants of the new reversing-pulse generator are reduced to about 1/3－1/10 of those of the previous one, because the responses of the DA circuit and DU unit with MOS-FET as the switching element are improved. This new reversing-pulse generator may be utilized to evaluate the electrooptical and hydrodynamic parameters and the structure of smaller macromolecules, for instance, short DNA, protein, and the protein-nucleic acid complexes in ionic solution, because of the stable electric pulse with short time constants. The new generator can deliver a field pulse width variable up to 1.2 s, which makes the maximum pulse duration four hundred times longer, as compared with the previous one, although it can apply only low-field strength pulse (up to ca. 1/7 of the previous one) to a sample solution because of the low voltage tolerance of the present MOS-FET. Therefore, the new reversing-pulse generator can also be utilized for larger colloidal particles, e.g., clay and bacteria. The DU circuitry with MOS-FET can deliver a stable electric pulse to a sample solution with high conductivity (up to 0.2 $moldm^{-3}$ NaCl and/or $MgCl_2$) or under the physiological condition (0.15 $moldm^{-3}$ NaCl solution). When such a long pulse is applied to a high-conductivity sample, however, the temperature jump probably occurs unavoidably due to the Joule heat. When a reversing pulse is applied, it is possible to deliberately change a pulse duration as well as a field strength of the first relative to the second pulse, because each circuitry can independently generate these two pulses.

Table III-4-1. Comparison Between New and Old Reversing-Pulse Generators

	Pulse shape	voltage	duration	Time constant			Is^*
				t_B[a] / ns	t_R[b] / ns	t_D[c] / ns	
New	Single-square	5－300V	10μs－1s	150	—	50	0－0.2
	Reversing	5－200V	10μs－1s	150	150	50	0－0.2
Old†	Single-square	300V－6kV	10μs－10ms	400	—	600	0－0.01
	Reversing	300V－6kV	10μs－10ms	400	800	600	0－0.01

*) Ionic strength.

a, b, and c) The time constants of the buildup, reverse, and decay part, respectively.

†) Details of the old reversing-pulse generator are described in ref 2.

References

1. Fredericq, E.; Houssier, C. *Electric Dichroism and Electric Birefringence*; Clarendon Press: Oxford 1973.

2. Yamaoka, K.; Fukudome, K.; Matsumoto, S.; Hino. Y. *J. Colloid Interface Sci.* **1994**, *168*, 349.

3. Sasai, R.; Ikuta, N.; Yamaoka, K. *J. Phys. Chem.* **1996**, *100*, 17266.

4. Pörschke, D.; Obst, A. *Rev. Sci. Instrum.* **1991**, *62*, 818.

5. Shah, M. J. *J. Phys. Chem.* **1963**, *67*, 2215.

6. Yoshida, M.; Hayashi, M.; Kikuchi, K.; Watanabe, H. In *Dynamic Behavior of Macromolecules, Colloids, Liquid Crystals and Biological Systems by Optical and Electrooptical Methods*; Hirokawa Publ. Co.: Tokyo, 1989; pp. 249−355.

7. Sasai, R.; Yamaoka, K. *J. Phys. Chem.* **1995**, *99*, 17754.

8. Yamaoka, K.; Tanigawa, M.; Sasai, R. *J. Phys. Chem.* **1994**, *101*, 1625.

— *Chapter IV.* —

Theory

IV. 1. Introduction

Electrooptical method is useful to study the electrical, optical, and hydrodynamic properties of the particles dispersed in solvent, such as biopolymers,[1-13] polyelectrolytes,[11,14-21] clays,[22-27] and so on. The electric birefringence is very suitable for the study of dilute dispersed systems, since this method is very sensitive to difference of properties of particles dispersed in media. The RPEB transient signal gives an information on the kinds of electric dipole moment; the field strength dependence of the steady-state electric birefringence gives the magnitude of electric dipole moments and optical anisotropic factor of dispersed particles; and the hydrodynamic size of particles dispersed in media is evaluated from the field-off signal (cf. ***Chapter II***). The theoretical development of RPEB for particles dispersed in media was rather slow, as compared with experimental applications. Especially, there are few theories for disklike particles such as clay. These RPEB theories, however, are necessary for estimating the electrooptic and hydrodynamic parameters of dispersed particles from experimental data. In this study, two new theories were derived for disklike particle.

IV. 2. RPEB Transient Theory

The first theory for transient RPEB for dispersed particles and/or molecules was formulated by Tinoco and Yamaoka more than three decades ago (hereafter abbreviated as TY theory).[28] In TY theory, an ionized polymer possesses the following two electric dipole moments: (1) permanent dipole moment (μ), and (2) the electric polarizability anisotropy $\Delta\alpha'$ ($= \alpha'_{33} - \alpha'_{11}$). The latter results from the interaction of the external electric field with the electronic and/or instantaneously-saturated (time-independent) polarizabilities of a macroion along the longitudinal (α'_{33}) and transverse (α'_{11}) axes, which are responsible for the field-induced electric moments.[28] The transient signal of this theory is expressed as follows.

$$\begin{aligned}
\Delta_B(t) &= \frac{\Delta n_B(t)}{\Delta n_B(\infty)} = 1 - \frac{3}{2}\left(\frac{Q}{Q+1}\right)e^{-2\Theta t} + \frac{1}{2}\left(\frac{Q-2}{Q+1}\right)e^{-6\Theta t} \\
\Delta_R(t) &= \frac{\Delta n_R(t)}{\Delta n_R(\infty)} = 1 - \left(\frac{3Q}{Q+1}\right)\left(e^{-2\Theta t} - e^{-6\Theta t}\right) \qquad (1) \\
\Delta_D(t) &= \frac{\Delta n_D(t)}{\Delta n_D(0)} = e^{-6\Theta t}
\end{aligned}$$

where $Q = \beta^2/2\gamma$ ($\beta = \mu E/kT$, $\gamma = \Delta\alpha' E^2/2kT$) and Θ is the rotational diffusion coefficient of particle.[28] Figure IV-2-1 shows RPEB transient theoretical curves obtained from eq 1. This theory gives the theoretical curves of various patterns. Therefore, this TY theory has been applied to analyze the various RPEB transient signals experimentally obtained. Based on the original TY theory, some RPEB transient theories have been proposed by various workers.[29-31] No complete theory, however, is yet available that may predict the RPEB transient signal of an arbitrarily shaped molecule in media.

Recently, a new theory on RPEB was developed by Szabo *et al.* for a rodlike macroions.[32] This (SHE) theory is new in that field orientation is solely based on the distortion of ion-atmosphere around a cylindrically symmetric polyion molecule, and that the coupling between the rotational and ion-atmosphere dynamics is taken into account. The SHE theory was applied to interpret a small minimum appearing in a RPEB signal of restriction-enzyme fragmented DNA on the field reversal. A feature of this theory is distinct from previous ones,[28,29,31] in which the relaxation time resulting from the fluctuation of counterions in the surrounding ion-atmosphere is considered, in addition to the rotational relaxation time due to the whole molecule. According to Oosawa's ion-fluctuation theory,[33] this relaxation time is independent of the application of a weak external electric field.

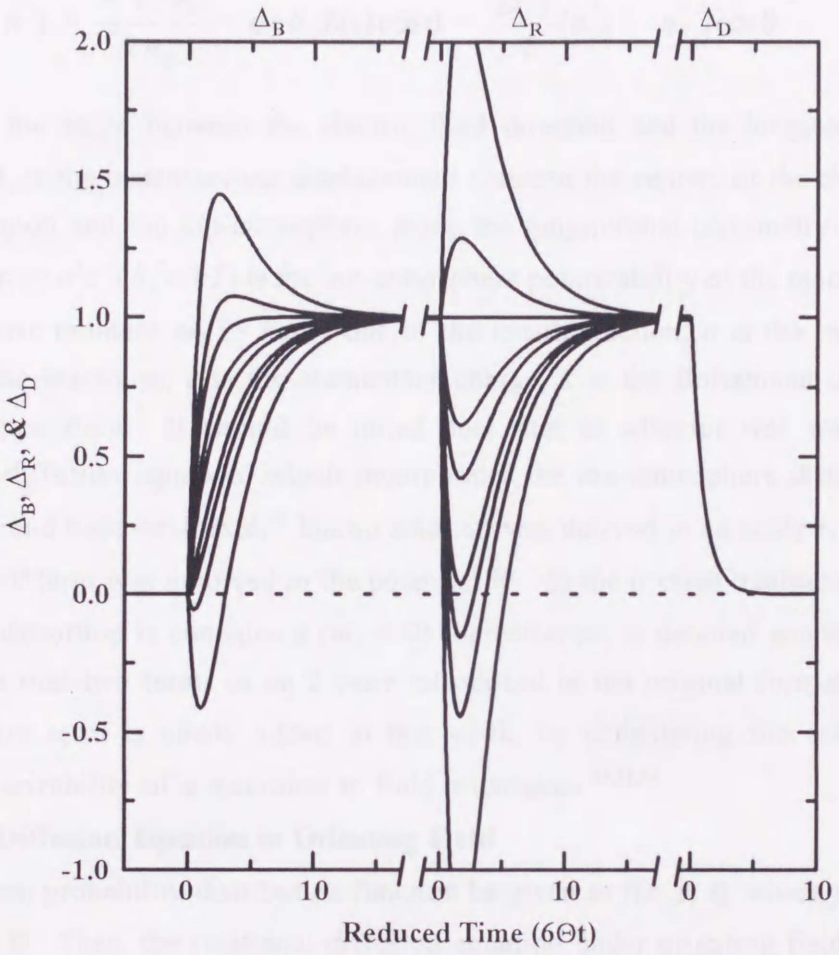

Figure IV-2-1. Theoretical RPEB curves calculated on the basis of the classical orientation mechanism. Parameters, $\beta^2/2\gamma$, of each theoretical curve are -0.5, -0.2, 0 (induced dipole orientation), 0.5, 1, 5, ∞ (permanent dipole orientation), -2, -5 from the top.

We add the intrinsic polarizability anisotropy of a macroion to the SHE theory, and derive new RPEB transient theory. In this section, newly derived RPEB transient theory and its application to the measured signal of montmorillonite suspended in aqueous media will be described.

IV. 2. 1. Potential

Let us consider a cylindrically symmetric macroion molecule, for which the symmetry axis is designated as the 3 axis and the perpendicular axis as the 1 (= 2) axis. A macroion solution is so dilute that any interactions between macroions are negligible. Based on the coupled rotational and ion-atmosphere dynamics,[32] the total potential W of the macroion experienced

by an external pulsed electric field $E(t)$ may be given as follows:

$$W(\theta, \delta_3, \Delta\alpha') = \frac{n^2 e^2 \delta_3^2}{2\alpha_3} - ne\delta_3 E(t)\cos\theta - \frac{E(t)^2}{2}\left(\alpha'_{33} - \alpha'_{11}\right)\cos\theta \qquad (2)$$

where θ is the angle between the electric field direction and the longitudinal axis of the macroion; δ_3 is the instantaneous displacement between the centers of the charge distribution of the macroion and the ion-atmosphere along the longitudinal (symmetry or 3) axis of the macroion, α_3 ($= n^2e^2<\delta_3^2>/kT$) is the ion-atmosphere polarizability of the macroion responsible for the electric moment m_3 ($= ne\delta_3$) due to the ion-fluctuation; n is the number of ionized groups on the macroion; e is the elementary charge; k is the Boltzmann constant; T is the absolute temperature. It should be noted here that an attempt was made to solve the generalized diffusion equation, which incorporates the ion-atmosphere distortions along the longitudinal and transverse axes,[32] but no solution was derived in an analytic form because of the $\delta_1 E(t)\sin\theta$ term was involved in the potential W. In the present treatment, therefore, only the parallel distortion is considered ($m_1 = 0$) (hereafter m_3 is denoted simply as m).

While the first two terms in eq 2 were introduced in the original formalism by Szabo *et al.*,[32] the third term is newly added in this work, by considering the contribution of the intrinsic polarizability of a macroion to field orientation.[28,31,34]

IV. 2. 2. Diffusion Equation in Orienting Field

Let the joint probability distribution function be given as $f(x, y, t)$, where $y = (m^2/2\alpha_3 kT)^{1/2}$ and $x = \cos\theta$. Then, the rotational diffusion equation under orienting field is given as[32]

$$\frac{\partial}{\partial t}f(x,y,t) = \Theta\frac{\partial}{\partial x}\left[(1-x^2)\left(\frac{\partial}{\partial x} + \frac{1}{kT}\frac{\partial W}{\partial x}\right)f(x,y,t)\right] + \frac{n^2e^2}{2\alpha_3 kT}D_I\frac{\partial}{\partial y}\left[\left(\frac{\partial}{\partial y} + \frac{1}{kT}\frac{\partial W}{\partial y}\right)f(x,y,t)\right] \qquad (3)$$

where Θ is the rotary diffusion coefficient of the whole molecule around the transverse axis with the rotational relaxation time τ_θ ($= 1/6\Theta$), W is the potential in eq 2, D_I is the translational diffusion coefficient of the ion-atmosphere along the symmetry axis and equivalent to the relaxation time τ_I ($= \alpha_3 kT/n^2e^2D_I$). According to Szabo *et al.*,[32] the joint distribution function is expanded in a series of the product of the Legendre $P_i(x)$ and Hermete $H_j(y)$ polynomials as

$$f(x,y,t) = \frac{1}{\sqrt{x}}\left[\sum_{i,j=0}^{\infty} a_{i,j}(t)\,P_i(x)\,H_j(y)\,e^{-y^2}\right] \tag{4}$$

Substituting eqs 2 and 4 in eq 3 and neglecting the terms higher than $E(t)^2$, eq 3 is solved. Then, the initial conditions for the buildup process of the birefringence are $a_{11}(0) = 0$ and $a_{20}(0) = 0$, and for the reverse process, $a_{11}(0) = -a_{11}(\infty)$ and $a_{20}(0) = a_{20}(\infty)$.

IV. 2. 3. RPEB Expressions in the Kerr-Law Region

The time-dependent electric birefringence, $\Delta n(t)$, is explicitly given as

$$\begin{aligned}\Delta n(t) &= 2\pi C_v\left(\frac{\Delta g}{n}\right)\left\langle P_2[\cos\theta(t)]\right\rangle \\ &= \int_{-\infty}^{\infty} d\delta \int_{0}^{\pi} \sin\theta d\theta\, P_2(\cos\theta) f(\delta,\theta,t)\end{aligned} \tag{5}$$

This equation was calculated with a single coefficient for the low-field region (up to E^2 terms), where Kerr law holds

$$\left\langle P_2[\cos\theta(t)]\right\rangle = \frac{2}{5}a_{20}(t) \tag{6}$$

The normalized birefringence for the buildup process $\Delta_B(t)$ is given as

$$\Delta_B(t) = 1 - \left[1 + \left(\frac{6\Theta\tau_I}{1-4\Theta\tau_I}\right)\left(\frac{q}{q+1}\right)\right]e^{-6\Theta t} + \left(\frac{6\Theta\tau_I}{1-4\Theta\tau_I}\right)\left(\frac{q}{q+1}\right)e^{-\left(2\Theta+\tau_I^{-1}\right)t} \tag{7}$$

Similarly, the normalized birefringence for the reverse process $\Delta_R(t)$ is given as

$$\Delta_R(t) = 1 - \left(\frac{12\Theta\tau_I}{1-4\Theta\tau_I}\right)\left(\frac{q}{q+1}\right)\left[e^{-6\Theta t} - e^{-\left(2\Theta+\tau_I^{-1}\right)t}\right] \tag{8}$$

Finally, the normalized birefringence for the field-off decay process $\Delta_D(t)$ is given as

$$\Delta_D(t) = e^{-6\Theta t} \tag{9}$$

where $q = \alpha_3/\Delta\alpha'$.

Equations 7 and 8 derived here for the buildup and reverse processes now contain additional terms, which were not present in the SHE formulas and originate from the intrinsic polarizability anisotropy $\Delta\alpha'$, i.e., q-terms. If no field-induced electric moment is present, i.e.,

$\Delta\alpha'$ is zero, then $q/(q+1) = 1$. In this case, eqs 7 and 8 reduce exactly to those derived by Szabo *et al.*[32] Since q is the ratio of the ion-fluctuation polarizability to the field-induced polarizability anisotropy, a value of q can be either positive, zero, or negative. Thus, the versatility of eqs 7 and 8 is evident (vide post).

In the Kerr-law region, the steady-state electric birefringence $\Delta n(t \to \infty)$ is given from eqs 5 and 6 as

$$\Delta n(t\to\infty) = n_{\parallel} - n_{\perp} = 2\pi C_{\nu}\left(\frac{\Delta g}{n}\right)\left[\frac{\langle m^2\rangle}{(kT)^2} + \frac{\Delta\alpha'}{kT}\right]\left(\frac{E^2}{15}\right) \qquad (10)$$

where $\langle m^2\rangle$ ($= n^2e^2\langle\delta^2\rangle$) is the mean-squared electric dipole moment due to ion-fluctuation along the symmetry axis. The first term in the brackets of eq 10 results from the SHE theory, while the second term originates from the present theory, which newly includes the polarizability anisotropy $\Delta\alpha'$ in eq 2. Since the sign of $\Delta\alpha'$ may be either positive or negative, the quantity in the brackets can possibly be negative; hence, the sign of the steady-state birefringence Δn could be either positive or negative, even if the reduced optical anisotropy factor ($\Delta g/n$) is, say, positive. For this case, however, the SHE theory always predicts only the positive sign for Δn. Thus, eq 10 can be applied not only to a prolate but also to an oblate ellipsoid model.[23,34] Thus, the versatility of the present theory is evident.

IV. 2. 4. Theoretical Curves of Newly Derived Theory

Figure IV-2-2 shows theoretical RPEB curves calculated from eqs 7 and 8 with the parameter of q at a fixed τ^* ($=\tau_1/\tau_\theta$) of unity and plotted against the reduced time $6\Theta t$. At $q = 0$, which corresponds to $\alpha_3 = 0$, the field orientation is due only to intrinsic polarizability. The curve rises smoothly with no inflection, showing no change upon field reversal, and it decays exponentially upon field removal. As values of q increase, a minimum appears in the reverse process. At $q = \infty$ or $\Delta\alpha' = 0$, which corresponds to the Szabo *et al.* case,[32] the initial buildup curve rises tangentially with an inflection, and the reverse shows a moderate minimum. The most interesting feature associated with the present theory is the appearance of a deep minimum not only in the reverse but also in the buildup at a certain range of q in such that the minima often cross the base line (horizontal dashed line). These minima are extremely deep, as q values approach -1. Clearly, the present theory can deal with a variety of observed RPEB curves, whereas the SHE theory can possibly give rise to a single curve for the case $q = \infty$.

Figure IV-2-3 shows theoretical RPEB curves for negative value of q in the $-1<q<0$ range. According to the present theory, the curves should show large humps each in the buildup and reverse process. The hump in the buildup becomes less distinct than that in the reverse, as

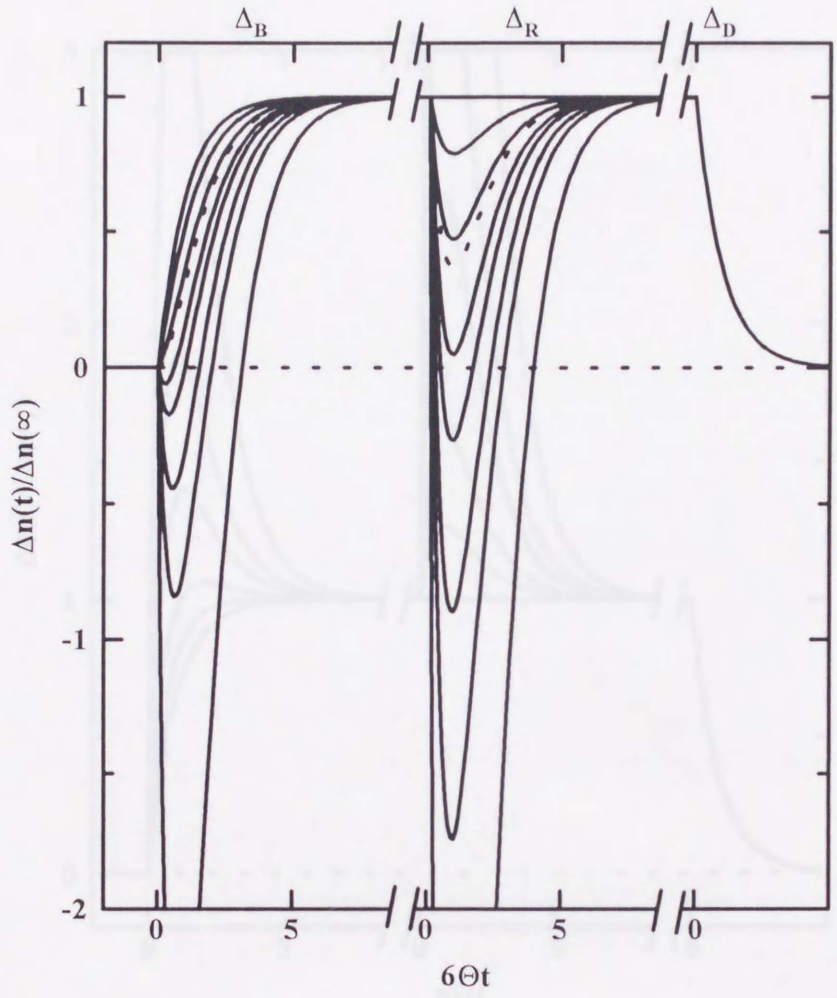

Figure IV-2-2. Theoretical RPEB curves calculated on the basis of eqs 7—9 with various values for the parameter q at a constant τ^* of unity. This case is the disk-shaped model in which dips appear in the build and reverse processes. The ordinate is the normalized birefringence $\Delta n(t)/\Delta n(\infty)$. The abscissa is the reduced time $6\Theta t$. q values are 0, 0.5, 5, ∞ (broken line), -3, -2, -1.5, -1.3, -1.1 from the top. Broken line curve corresponds to the one obtained by the original SHE theory.

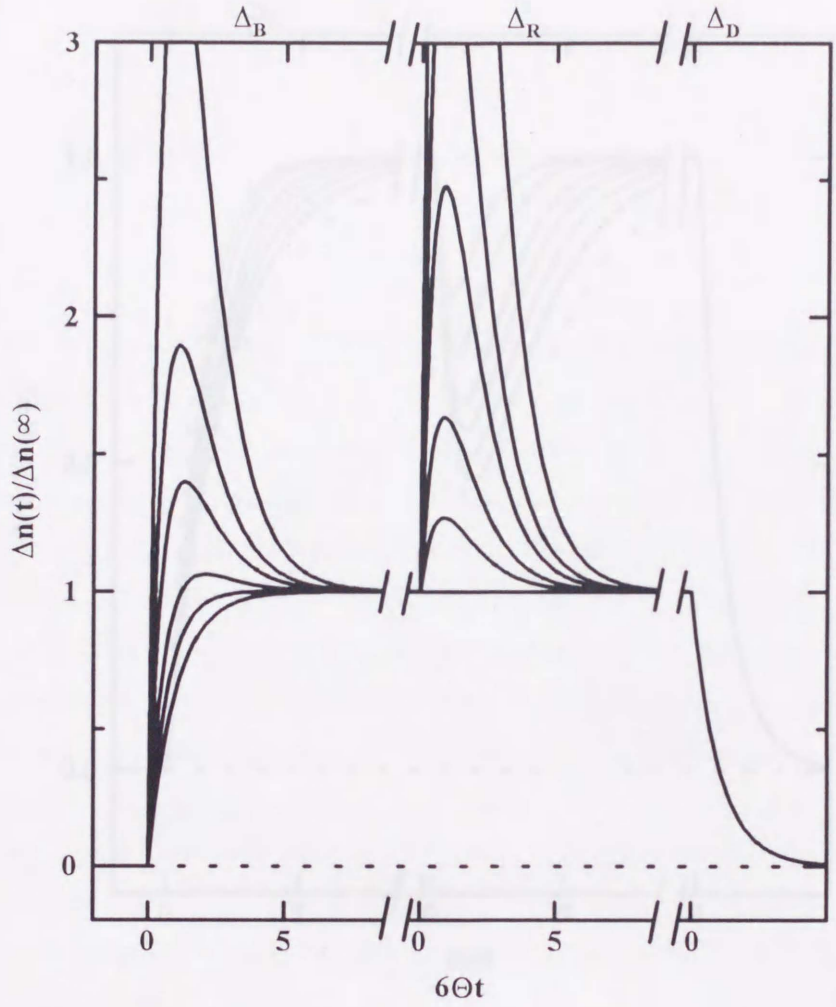

Figure IV-2-3. Theoretical RPEB curves calculated on the basis of eqs 7—9 with various values for the parameter q at a constant τ^* of unity. This case is the disk-shaped model in which humps appear in the buildup and reverse processes. q values are -0.9, -0.8, -0.7, -0.5, -0.3, 0 from the top. Other notations are all the same as those in Figure IV-2-2.

q values approach 0 form the negative side. This appearance of two humps in RPEB curves is a new feature associated with the present extended theory.

Figure IV-2-4 shows another case of RPEB curves in which the parameter τ^* was varied at a fixed q value of unity. Theoretical curves indicate that no minimum appears in the reverse if the ion-atmosphere relaxation time is very fast, as compared with the overall molecular rotational relaxation (τ^*=0). The buildup signal rises more slowly, if the two relaxation times become comparable, with a deep minimum appearing in the reverse. According to Oosawa's

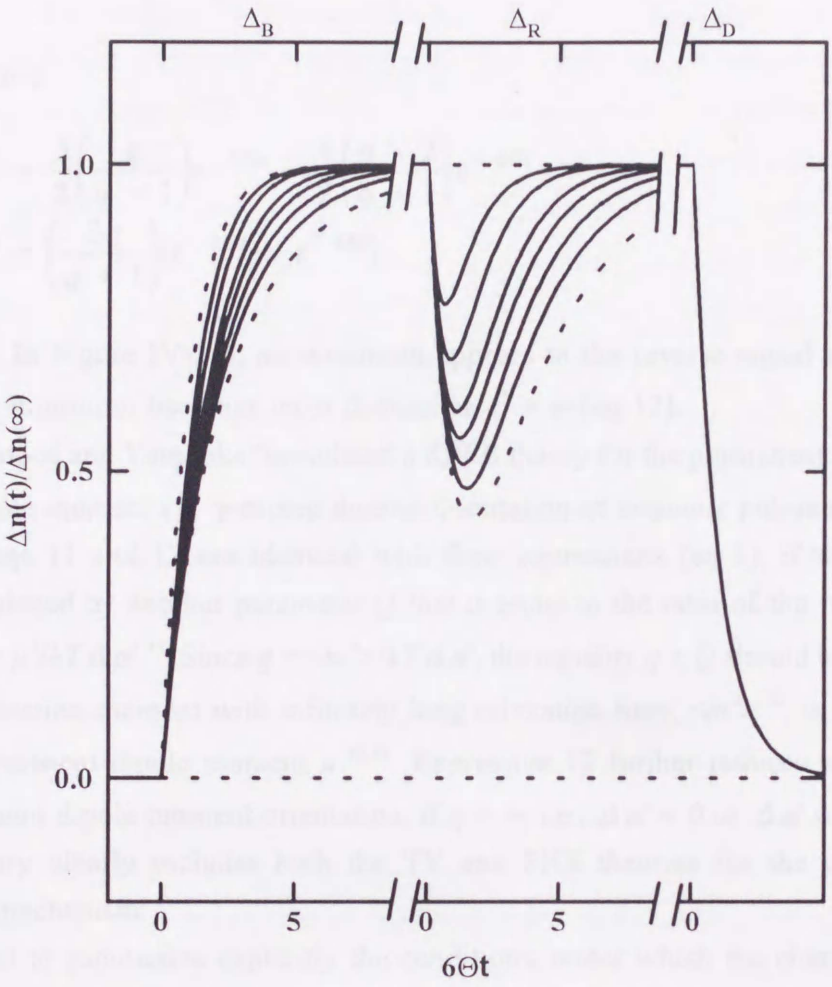

Figure IV-2-4. Theoretical RPEB curves calculated on the basis of eqs 7—9 with various values for the parameter τ^* at a constant q of unity. This case is the cylinder-shaped model in which a dip appears only in the reverse process. τ^* values are 0 (broken line), 0.5, 1, 2, 3, 5, 10, ∞ (broken line) from the top. Broken line curves correspond to those already obtained by the original TY theory. Other notations are all the same as those in Figure IV-2-2.

ion-fluctuation theory, the relaxation time τ_I for the distortion of ion-atmosphere may be very fast ($\tau_I \approx 0$) or very slow ($\tau_I \approx \infty$) in the limiting case. Hence, the electric dipole moment m conceptually reduces either to a classical electronic or instantaneously induced ionic dipole moment $\Delta\alpha' E$ ($\tau^* = 0$) or to the permanent dipole moment μ ($\tau^* = \infty$). In these cases, RPEB expressions 7 and 8 reduce to

$$\Delta_B(t) = 1 - e^{-6\Theta t}$$
$$\Delta_R(t) = 1 \qquad (11)$$

for $\tau^* = 0$, and

$$\Delta_B(t) = 1 - \frac{3}{2}\left(\frac{q}{q+1}\right)e^{-2\Theta t} + \frac{1}{2}\left(\frac{q-2}{q+1}\right)e^{-6\Theta t}$$
$$\Delta_R(t) = 1 - \left(\frac{3q}{q+1}\right)(e^{-2\Theta t} - e^{-6\Theta t}) \qquad (12)$$

for $\tau^* = \infty$. In Figure IV-2-4, no minimum appears in the reverse signal at $\tau^* = 0$ (eq 11), whereas the minimum becomes most distinct at $\tau^* = \infty$ (eq 12).

Earlier Tinoco and Yamaoka formulated a RPEB theory for the permanent and electronically induced dipole moment (β, γ-mixed dipole) orientation of nonionic polymers.[28] It should be noted that eqs 11 and 12 are identical with their expressions (eq 1), if the parameter q is formally replaced by another parameter Q that is equal to the ratio of the two moments, i.e., $Q = \beta^2/2\gamma = \mu^2/kT\Delta\alpha'$.[34] Since $q = \langle m^2\rangle/kT\Delta\alpha'$, the equality $q = Q$ should hold, provided that the ion-fluctuation moment with infinitely long relaxation time, $\langle m^2\rangle^{1/2}$, is considered as the classical permanent dipole moment μ.[32,33] Expression 12 further reduces to the case for the pure permanent dipole moment orientation, if $q = \infty$, i.e., $\Delta\alpha' = 0$ or $\Delta\alpha' \ll \alpha_3$.[28] Hence, the present theory clearly includes both the TY and SHE theories for the classical nonionic orientation mechanism.

It is useful to summarize explicitly the conditions, under which the characteristic features appear in the buildup and reverse processes of theoretical curves as shown in Figures IV-2-2 and -3, provided that $1 - 4\Theta\tau_1 \neq 0$ (cf. Table IV-3-1).

Table IV-3-1. Characteristic Features in the buildup and reverse processes of theoretical curves

Features	Buildup	Reverse
Minimum	$q < -1$	$q > 0$, $q < -1$
Hump	$-1 < q < 0$	$-1 < q < 0$
Monotonic rise	$q > 0$	.....
No change	.....	$q = 0$

IV. 2. 5. Comparison with experimental RPEB signal

Figure IV-2-5 shows curve-fitting of an experimental RPEB signal of montmorillonite particles with the sodium counterion dispersed in aqueous medium to a theoretical curve calculated from eqs 7—9. This montmorillonite (K10) sample, purchased from Aldrich Chemical Co., was suspended in distilled water and then settled on standing. The supernatant was recovered and subjected for sonication at 0°C for 40 min at a power level of 200W (20 kHz). The counterion of the clay particle was converted solely to sodium ion by dialysis. Details of the preparation and characterization of sample solutions are given elsewhere.[26] RPEB measurements were performed at 25°C and 633 nm on a laser RPEB instrument, which was constructed in our laboratory and described in detail in combination with a newly constructed reversing-pulse generator system (cf. ***Chapter III.***). Measured at a very weak field of 30 V/cm, where the Kerr law holds, the observed signal exhibits a minimum in the buildup process and a much deeper second minimum in the reverse. This is a unique feature that was noted for negative q values in Figure IV-2-2. The experimental curve of the decay process was first analyzed with eq 9 to evaluate the rotational relaxation time τ_θ, and then the buildup and reverse processes were fitted by adjusting the parameters q and τ^*. The best-fitted curve is shown with solid lines in Figure IV-2-5, for which the parameters are $q = -1.43$ and $\tau^* = 1.46$ ($\tau_I = 35$ ms and $\tau_\theta = 1/6\Theta = 24$ ms).

Both observed and calculated RPEB curves agree quite well. A negative q value means a negative $\Delta\alpha'$ value, which in turn indicates that the intrinsic polarizability perpendicular to the symmetry axis, i.e., α'_{11}, is larger than the one parallel to the axis, α'_{33}. Thus, the shape of montmorillonite particle should indeed be disklike rather than cylindrical.[23] As judged from τ^* value, the relaxation time of the disklike particle. Thus, the electric dipole moment $\langle m^2 \rangle^{1/2}$, which contributes to the field orientation, does not behave like a permanent dipole μ. It should result from the ion-fluctuation along the symmetry axis, contrary to the original suggestion that a bentonite particle possesses the permanent dipole moment.[23] In order to rule out this notion further, the broken lines in Figure IV-2-5 were calculated from eq 12 by setting $q = 0$ and $\tau^* = \infty$ for field orientation due solely to the permanent dipole moment μ. This disagreement between observed and calculated curves is obvious in this case.

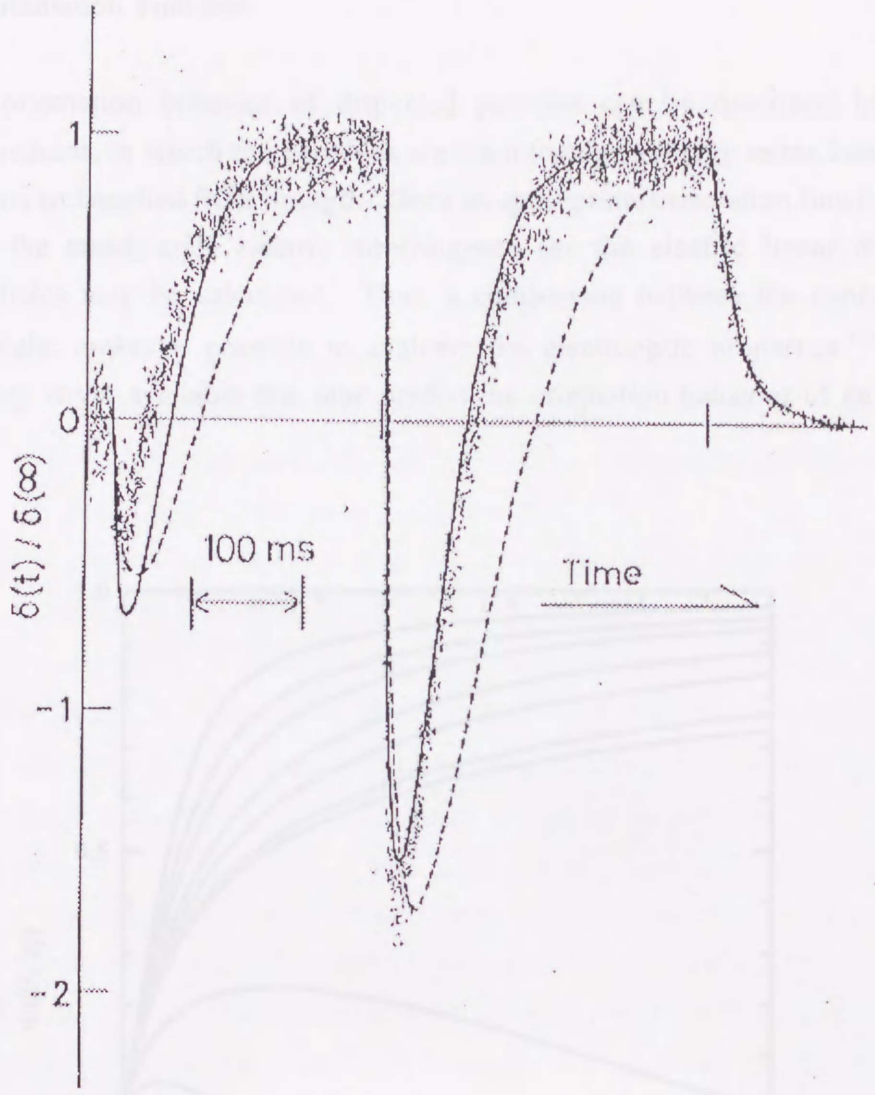

Figure IV-2-5. Experimentally obtained low-field RPEB signal at 30 V/cm for montmorillonite suspended in aqueous medium with sodium ions at 25 °C and the best-fitting theoretical curves for the present theory (solid line) and the TY theory (broken line) with the observed relaxation time τ_θ of 24 ms, which was evaluated from the decay signal. Parameters used for fitting, q = -1.43 and τ_1 = 35 ms (solid line) and q = -1.95 and $\tau_1 = \infty$ (broken line). The sampling time between two successive points in observed signal is 0.2 ms. The sign of $\delta(\infty)$ is negative.

V. 3. Orientation Function

The field orientation behavior of dispersed particles can be described by theoretical orientation functions, in which the variables are the interaction energy terms between electric dipole moments and applied field strength. Once an appropriate orientation function is derived theoretically, the steady-state electric birefringence (or the electric linear dichroism) of dispersed particles may be calculated. Thus, a comparison between the experimental and theoretical results makes it possible to evaluate the electrooptic properties.[5-7,13,14,23,34] No complete theory is yet available that may predict the orientation behavior of an arbitrarily

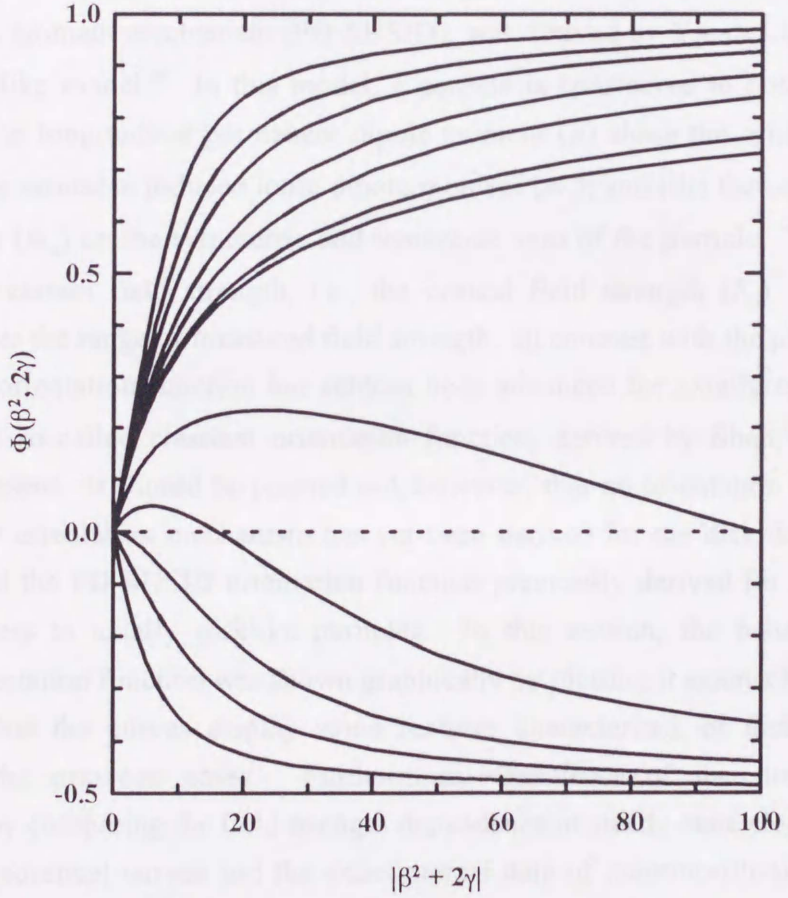

Figure IV-3-1. Theoretical orientation function curves calculated on the basis of classical orientation mechanism. Parameters, $\beta^2/2\gamma$, of each theoretical curve are 0 (induced dipole orientation for rodlike model), 1, 2, 5, 10, 50, 100, ∞ (permanent dipole orientation), -5, -2, -1, -0 (induced dipole orientation for disklike model) from the top.

shaped molecule in aqueous solution. The so-called classical orientation function was first derived by O'Konski *et al.*[34] for an axial symmetric rodlike model and by Shah[23] for an axial symmetric disklike model. In this model, two types of electric moments have so far been considered: (i) the intrinsic permanent electric dipole moment (μ), for which the structure is responsible, and (ii) the instantaneously field-induced covalent dipole moment (m_{el}), which results from the electronic and/or atomic polarizability anisotropy ($\Delta\alpha$). Figure IV-3-1 shows theoretical curves of the classical orientation function. When the parameter $\beta^2/2\gamma$, which is the ratio between μ and m_{el}, is positive, a particle is rodlike shape. In $\beta^2/2\gamma < 0$, a particle is disklike shape. All theoretical curves of classical orientation function approach 1.0 (rodlike model, $\beta^2/2\gamma > 0$) or −0.5 (disklike model, $\beta^2/2\gamma < 0$) with increasing field strengths, but in different fashions, depending on the parameters, $\beta^2/2\gamma$.

Recently, the orientation function, based on the permanent dipole, saturable and unsaturable induced dipole moment mechanism (PD-SUSID), was derived by Yamaoka *et al.* for an axial symmetric rodlike model.[14] In this model, a particle is considered to possess three electric moments: (i) the longitudinal permanent dipole moment (μ) along the symmetric axis of the particle, (ii) the saturable induced ionic dipole moment (m_s), and (iii) the unsaturable induced dipole moment (m_u) on the symmetric and transverse axes of the particle. The moment m_s is saturated at a certain field strength, i.e., the critical field strength (E_0). The m_u remains unsaturated over the range of measured field strength. In contrast with the progress for rodlike polymers, the orientation function has seldom been advanced for axially symmetric disklike particles. The so-called classical orientation function, derived by Shah,[23] is the only one available at present. It should be pointed out, however, that no orientation function based on the PD-SUSID orientation mechanism has yet been derived for the disklike particle.

We extended the PD-SUSID orientation function previously derived for axially symmetric rodlike polymers to axially disklike particles. In this section, the behavior of this new theoretical orientation function was shown graphically by plotting it against field strength, with an emphasis that the curves display some features characteristic of disklike particle, not observed in the previous cases. Furthermore, usefulness of the present theory was demonstrated by comparing the field strength dependence of steady-state electric birefringence between the theoretical curves and the experimental data of montmorillonite dispersion.

IV. 3. 1. Electric Moments.

In order to extended the PD-SUSID orientation mechanism to axially symmetric disklike particle, totally three electric moments are assumed, as shown in Figure IV-3-2. The particle may possess the permanent electric dipole moment μ, the covalent and/or ionic polarizability anisotropy $\Delta\alpha'$ ($=\alpha'_{33} - \alpha'_{11}$), where the subscriptions 33 and 11 indicate the directions of

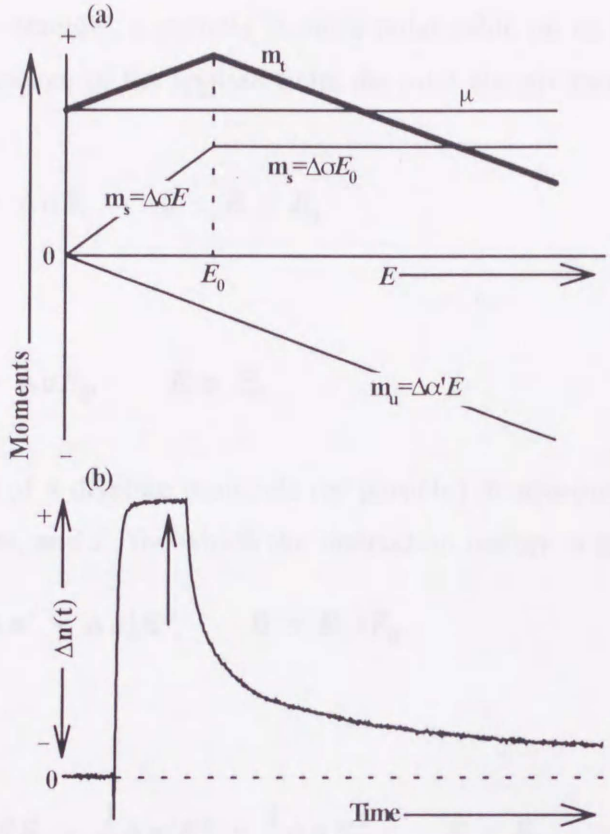

Figure IV-3-2. Dependence of electric dipole moments on applied external field strength E (a) and typical transient electric birefringence signal (b). μ is the electric permanent dipole moment, m_s the saturable induced dipole moment, m_u the unsaturable induced dipole moment, E_0 the critical field strength, and m_t the sum of electric moments. The arrow in (b) indicates the steady state.

symmetric axis (3) and of transverse axis (1) of the disk, responsible for the unsaturated induced dipole moment (m_u (= $\Delta\alpha' E$)), which is instantaneously induced by an external electric field (E), and the ionic polarizability anisotropy $\Delta\sigma$ (=σ_{33} − σ_{11}) responsible for the saturable induced ionic dipole moment (m_s (= $\Delta\sigma E$)), which is induced in a finite time and saturated to be $\Delta\sigma E_0$ at an electric field strength E_0. This field strength E_0 is called the critical field strength, and at any higher field strengths, the moment apparently behaves like the permanent electric dipole moment. After saturation at E_0, the transverse polarizability σ_{11} contributes negligibly, because the σ_{11} cancels out everywhere on the disk surface because of the longitudinal component σ_{33} becomes dominant. The most important feature, introduced into

the instantaneously time-independent induced dipole moment m_u, is that this moment should always be negative. Namely, a particle is more polarizable on its plane surface than out of the plane. In the presence of the applied field, the total electric moments (m_t) of the particle are given as

$$m_t = \mu + \Delta\alpha' E + \Delta\sigma E, \qquad 0 \le E \le E_0 \tag{13}$$

and

$$m_t = \mu + \Delta\alpha' E + \Delta\sigma E_0, \qquad E \ge E_0 \tag{14}$$

The field orientation of a disklike molecule (or particle) in aqueous media occurs due to the interaction between m_t and E, for which the interaction energy is given as

$$W = -\mu E - \frac{1}{2}(\Delta\alpha' + \Delta\sigma)E^2, \qquad 0 \le E \le E_0 \tag{15}$$

and

$$W = -\mu E - \Delta\sigma E E_0 - \frac{1}{2}\Delta\alpha' E^2 + \frac{1}{2}\Delta\sigma E_0^2, \qquad E \ge E_0 \tag{16}$$

IV. 3. 2. Orientation Function.

The following parameters are introduced:

$$\beta = \frac{\mu E}{kT},\ \rho_s = 2\gamma_0 E^* = \frac{\Delta\sigma E_0 E}{kT},\ \rho = \gamma_0 E^{*2} = \frac{\Delta\sigma E^2}{2kT},\ \gamma'' = \frac{\Delta\alpha E^2}{2kT},$$
$$\gamma_0 = \frac{\rho_s^2}{4\rho} = \frac{\Delta\sigma E_0^2}{2kT},\ E^* = \frac{E}{E_0},\ u = \cos\Theta \tag{17}$$

where $\Delta\alpha'' = \alpha'_{11} - \alpha'_{33} = -\Delta\alpha' (\ge 0)$, k is the Boltzmann constant, T is the absolute temperature, and θ is the angle between the symmetry axis of a particle and the direction of applied field. The energy term (W) must be specified by the relative magnitude between E_0 and E; therefore, two cases must be considered separately, i.e., $E^* \ge 1$ and $E^* \le 1$.

I. $E_0 \le E$ ($E^* \ge 1$), i.e., the saturated induced dipole moment is saturated at E_0. In this case, W must be subdivided into three terms (cf. Eqs 15 and 16):

(i) if $-E \le E\cos\theta \le -E_0$,

$$W_1 = -(\mu - \Delta\sigma E_0)E\cos\theta + \frac{1}{2}\Delta\alpha'' E^2\cos^2\theta + \frac{1}{2}\Delta\sigma E_0 \tag{18}$$

(ii) if $-E_0 \le E\cos\theta \le +E_0$,

$$W_2 = -\mu E\cos\theta + \frac{1}{2}(\Delta\alpha'' - \Delta\sigma)E^2\cos^2\theta \tag{19}$$

(iii) if $+E_0 \le E\cos\theta \le +E$,

$$W_3 = -(\mu + \Delta\sigma E_0)E\cos\theta + \frac{1}{2}\Delta\alpha'' E^2\cos^2\theta + \frac{1}{2}\Delta\sigma E_0 \tag{20}$$

The orientation function Φ contains either four (β, ρ_s, ρ, γ'') or three (β, ρ, γ'') variables and is given as

$$\Phi(\beta,\rho_s,\rho,\gamma'') = \frac{3}{2}\left[\frac{\int_{-1}^{1} u^2 e^{-W/kT}du}{\int_{-1}^{1} e^{-W/kT}du}\right] - \frac{1}{2}$$

$$= \frac{3}{2}\left[\frac{\int_{-1}^{-1/E^*} u^2 e^{-W_1/kT}du + \int_{-1/E^*}^{+1/E^*} u^2 e^{-W_2/kT}du + \int_{+1/E^*}^{1} u^2 e^{-W_3/kT}du}{\int_{-1}^{-1/E^*} e^{-W_1/kT}du + \int_{-1/E^*}^{+1/E^*} e^{-W_2/kT}du + \int_{+1/E^*}^{1} e^{-W_3/kT}du}\right] - \frac{1}{2} \tag{21}$$

$$= \frac{3}{2}\left[\frac{I_2 + I_4 + I_6}{I_1 + I_3 + I_5}\right] - \frac{1}{2}$$

$$I_1 = \frac{e^{-\gamma_0 + \frac{(\rho_s - \beta)^2}{4\gamma''}}}{\sqrt{\gamma''}}\left[erf\left(-\frac{\sqrt{\gamma''}}{E^*} - \frac{\rho_s - \beta}{2\sqrt{\gamma''}}\right) - erf\left(-\sqrt{\gamma''} - \frac{\rho_s - \beta}{2\sqrt{\gamma''}}\right)\right] \tag{22}$$

$$I_2 = \frac{e^{-\gamma_0}}{2\sqrt{\gamma''}}\left[\left(\frac{\sqrt{\gamma''}}{E^*} + \frac{\rho_s - \beta}{2\sqrt{\gamma''}}\right)e^{-\frac{\sqrt{\gamma''}}{E^{*2}} + \frac{\rho_s - \beta}{E^*}} - \left(\sqrt{\gamma''} + \frac{\rho_s - \beta}{2\sqrt{\gamma''}}\right)e^{-\gamma'' + \rho_s - \beta}\right]$$
$$+ \frac{e^{-\gamma_0 + \frac{(\rho_s - \beta)^2}{4\gamma''}}}{2\sqrt{\gamma''}}\left[\frac{(\rho_s - \beta)^2}{2\gamma''} + 1\right] \qquad (23)$$
$$\times \left[erf\left(-\frac{\sqrt{\gamma''}}{E^*} - \frac{\rho_s - \beta}{2\sqrt{\gamma''}}\right) - erf\left(-\sqrt{\gamma''} - \frac{\rho_s - \beta}{2\sqrt{\gamma''}}\right)\right]$$

(i) $(\gamma'' - \rho) \geq 0$:

$$I_3 = \frac{e^{\frac{\beta^2}{4(\gamma'' - \rho)}}}{\sqrt{\gamma'' - \rho}} \qquad (24)$$
$$\times \left[erf\left(\frac{\sqrt{\gamma'' - \rho}}{E^*} - \frac{\beta}{2\sqrt{\gamma'' - \rho}}\right) - erf\left(-\frac{\sqrt{\gamma'' - \rho}}{E^*} - \frac{\beta}{2\sqrt{\gamma'' - \rho}}\right)\right]$$

$$I_4 = \frac{e^{\frac{\rho - \gamma''}{E^{*2}}}}{2\sqrt{(\gamma'' - \rho)^3}}\left[\frac{\beta}{2\sqrt{\gamma'' - \rho}}\left(e^{-\beta/E^*} - e^{\beta/E^*}\right) - \frac{\sqrt{\gamma'' - \rho}}{E^*}\left(e^{\beta/E^*} + e^{-\beta/E^*}\right)\right]$$
$$+ \frac{e^{\frac{\beta^2}{4(\gamma'' - \rho)}}}{2\sqrt{(\gamma'' - \rho)^3}}\left(\frac{\beta^2}{2(\gamma'' - \rho)} + 1\right) \qquad (25)$$
$$\times \left[erf\left(\frac{\sqrt{\gamma'' - \rho}}{E^*} - \frac{\beta}{2\sqrt{\gamma'' - \rho}}\right) - erf\left(-\frac{\sqrt{\gamma'' - \rho}}{E^*} - \frac{\beta}{2\sqrt{\gamma'' - \rho}}\right)\right]$$

(ii) $(\gamma'' - \rho) \leq 0$:

$$I_3 = \frac{e^{-\frac{\beta^2}{4\sqrt{\rho - \gamma''}}}}{\sqrt{\rho - \gamma''}} \qquad (26)$$
$$\times \left[F\left(\frac{\beta}{2\sqrt{\rho - \gamma''}} + \frac{\sqrt{\rho - \gamma''}}{E^*}\right) - F\left(\frac{\beta}{2\sqrt{\rho - \gamma''}} - \frac{\sqrt{\rho - \gamma''}}{E^*}\right)\right]$$

$$I_4 = \frac{e^{\frac{\rho - \gamma''}{E^{*2}}}}{\sqrt{\rho - \gamma''}}\left[\frac{\sqrt{\rho - \gamma''}}{E^*}\left(e^{\beta/E^*} + e^{-\beta/E^*}\right) - \frac{\beta}{2\sqrt{\rho - \gamma''}}\left(e^{\beta/E^*} - e^{-\beta/E^*}\right)\right]$$
$$+\frac{e^{\frac{\beta^2}{4(\rho - \gamma'')}}}{2\sqrt{(\rho - \gamma'')^3}}\left(\frac{\beta^2}{2(\rho - \gamma'')} - 1\right) \qquad (27)$$
$$\times\left[F\left(\frac{\beta}{2\sqrt{\rho - \gamma''}} + \frac{\rho - \gamma''}{E^*}\right) - F\left(\frac{\beta}{2\sqrt{\rho - \gamma''}} - \frac{\rho - \gamma''}{E^*}\right)\right]$$

$$I_5 = \frac{e^{-\gamma_0 + \frac{(\rho_s + \beta)^2}{4\gamma''}}}{\sqrt{\gamma''}}\left[erf\left(\sqrt{\gamma''} - \frac{\rho_s + \beta}{2\sqrt{\gamma''}}\right) - erf\left(\frac{\sqrt{\gamma''}}{E^*} - \frac{\rho_s + \beta}{2\sqrt{\gamma''}}\right)\right] \qquad (28)$$

$$I_6 = \frac{e^{-\gamma_0}}{2\sqrt{\gamma''}}\left[\left(\frac{\sqrt{\gamma''}}{E^*} - \frac{\rho_s + \beta}{2\sqrt{\gamma''}}\right)e^{-\frac{\gamma''}{E^{*2}} + \frac{\rho_s + \beta}{E^*}} - \left(\sqrt{\gamma''} - \frac{\rho_s + \beta}{2\sqrt{\gamma''}}\right)e^{-\gamma'' + \rho_s + \beta}\right]$$
$$+\frac{e^{-\gamma_0 + \frac{(\rho_s + \beta)^2}{4\gamma''}}}{2\sqrt{\gamma''}}\left(\frac{(\rho_s + \beta)^2}{2\gamma''} + 1\right) \qquad (29)$$
$$\times\left[erf\left(\sqrt{\gamma''} - \frac{\rho_s + \beta}{2\sqrt{\gamma''}}\right) - erf\left(\frac{\sqrt{\gamma''}}{E^*} - \frac{\rho_s + \beta}{2\sqrt{\gamma''}}\right)\right]$$

where $erf\,(x) = \int_0^x \exp(-t^2)dt$ and $F\,(x) = \int_0^x \exp(t^2)dt$.

II. $E_0 \geq E\,(E^* \leq 1)$, i.e., the saturated induced dipole moment is unsaturated at any measurable electric fields. In this case, W is given over the entire range of field as

$$W = -\mu E\cos\theta + \frac{1}{2}(\Delta\alpha'' - \Delta\sigma)E^2\cos^2\theta \qquad (30)$$

Two cases must be considered here, because $(\gamma'' - \rho)$ can be either positive or negative. The orientation function is given as

$$\Phi(\beta,\rho,\gamma'') = \frac{3}{2}\left\{\frac{\int_{-1}^{1} u^2 e^{-W/kT}du}{\int_{-1}^{1} e^{-W/kT}du}\right\} - \frac{1}{2} \tag{31}$$

(i) $(\gamma'' - \rho) \geq 0$:

$$\Phi(\beta,\rho,\gamma'') = \frac{3}{4(\gamma'' - \rho)}\{e^{\rho - \gamma'' - \frac{\beta^2}{4(\gamma'' - \rho)}} \times \left[\frac{\left(\frac{\beta}{2\sqrt{\gamma'' - \rho}}\right)(e^{-\beta} - e^{\beta}) - \sqrt{\gamma'' - \rho}(e^{-\beta} + e^{\beta})}{erf\left(\sqrt{\gamma'' - \rho} - \frac{\beta}{2\sqrt{\gamma'' - \rho}}\right) - erf\left(-\sqrt{\gamma'' - \rho} - \frac{\beta}{2\sqrt{\gamma'' - \rho}}\right)}\right] + \frac{\beta}{2(\gamma'' - \rho)} + 1\} - \frac{1}{2} \tag{32}$$

(ii) $(\gamma'' - \rho) \leq 0$:

$$\Phi(\beta,\rho,\gamma'') = \frac{3}{4(\rho - \gamma'')}\{e^{\rho - \gamma'' + \frac{\beta^2}{4(\rho - \gamma'')}} \times \left[\frac{\sqrt{\rho - \gamma''}(e^{\beta} + e^{-\beta}) - \left(\frac{\beta}{2\sqrt{\rho - \gamma''}}\right)(e^{\beta} - e^{-\beta})}{F\left(\sqrt{\rho - \gamma''} + \frac{\beta}{2\sqrt{\rho - \gamma''}}\right) - F\left(-\sqrt{\rho - \gamma''} + \frac{\beta}{2\sqrt{\rho - \gamma''}}\right)}\right] + \frac{\beta}{2(\rho - \gamma'')} - 1\} - \frac{1}{2} \tag{33}$$

Equation 32 is reduced to the classical orientation function, derived by Shah,[23] if $\rho = 0$, whereas eq 33 corresponds to the classical orientation function, derived by O'Konski *et. al.* for rodlike particle,[34] if $\rho = 0$. The SUSID orientation function may be derived easily for disklike particle which possesses no permanent dipole moment, if β is set zero in eqs 18—33.

IV. 3. 3. General Behavior of PD-SUSID Orientation Function.

In Figure IV-3-3, some theoretical curves, calculated from eqs. 21, 32, and 33, are plotted against $(\beta^2 + \rho_s^2 \pm \gamma'')$, which is proportional to the second power of field strength. The

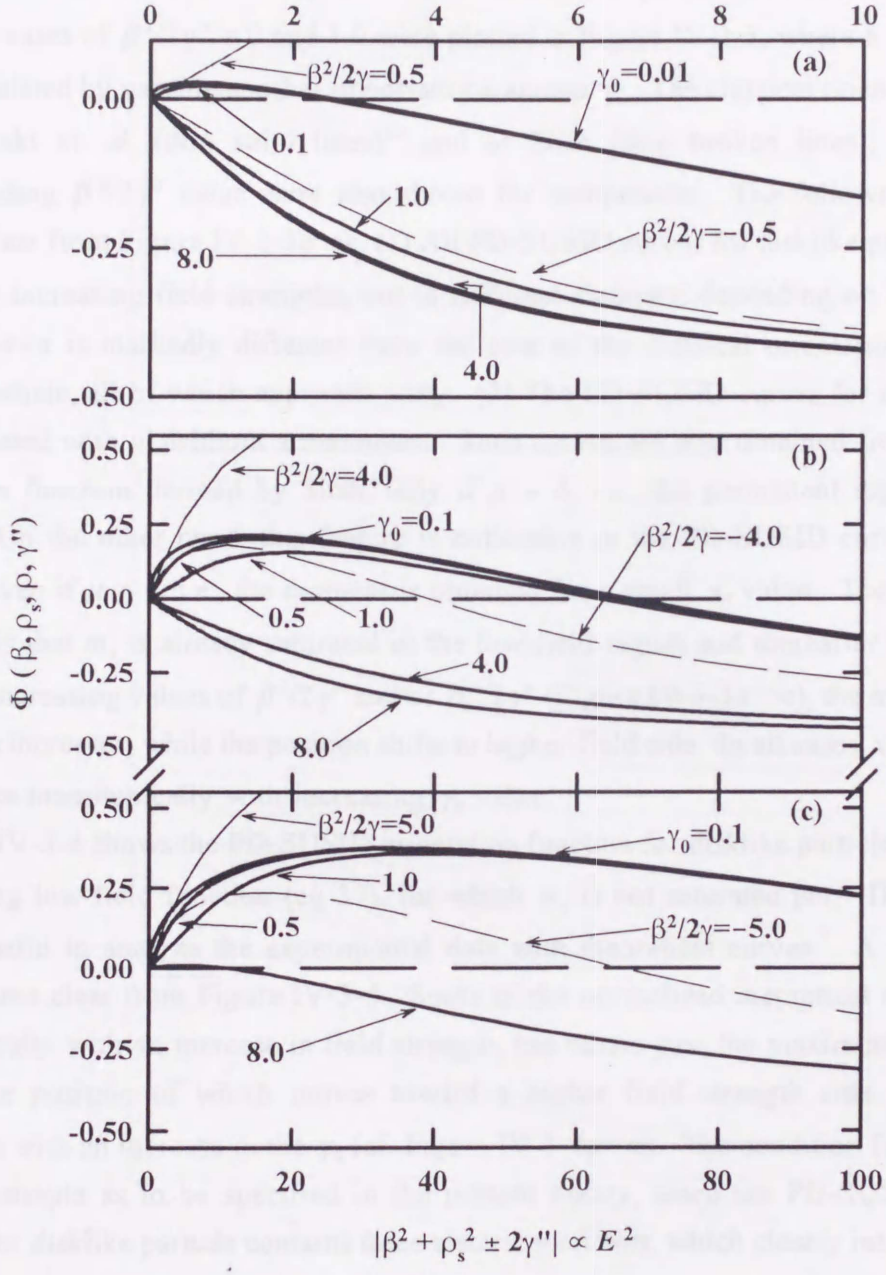

Figure IV-3-3. PD-SUSID orientation function for disklike particles, $\Phi(\beta, \rho_s, \rho, \gamma'')$ (solid lines). (a) $\beta^2/2\gamma'' = 0$, $\rho_s^2/2\gamma'' = 0.5$. (b) $\beta^2/2\gamma'' = 0$, $\rho_s^2/2\gamma'' = 4.0$. (c) $\beta^2/2\gamma'' = 1.0$, $\rho_s^2/2\gamma'' = 4.0$. Numerals in each figure denote values of γ_0, unless otherwise stated. The so-called classical orientation function, $\Phi(\beta, \gamma)$, for the rodlike model (thin solid line) with a positive $\beta^2/2\gamma$ and for the disklike model (thin broken line) with negative $\beta^2/2\gamma$. (a) $\beta^2/2\gamma = \pm 0.5$; (b) $\beta^2/2\gamma = \pm 4.0$; (c) $\beta^2/2\gamma = \pm 5.0$.

parameters $\beta^2/2\gamma''$ and $\rho_s^2/2\gamma''$ are the same as those used for the PD-SUSID orientation function for rodlike particles.[14] Each parameter represents the relative magnitude of three assumed electric moments and depends on the kind of a dispersed particle and its shape. Two particular cases of $\beta^2/2\gamma'' = 0$ and 1.0 were plotted in Figure IV-3-3, where a series of curves were calculated by varying another important parameter γ_0. The classical orientation functions of O'Konski *et. al.* (thin solid lines)[34] and of Shah (thin broken lines), $\Phi(\beta, \gamma)$, at a corresponding $\beta^2/2\gamma''$ value were also shown for comparison. The following three points became clear from Figure IV-3-3a—c. (1) All PD-SUSID curves for disklike particle approach −0.5 with increasing field strengths, but in different fashions, depending on the parameters. This behavior is markedly different from the case of the classical orientation functions for rodlike particle, all of which approach unity. (2) The PD-SUSID curves for disklike particle are associated with or without a maximum. Such curves are also obtained from the classical orientation function derived by Shah, only if $\mu \neq 0$; i.e., the permanent dipole moment is present. On the other hand, this feature is noticeable in the PD-SUSID curves for disklike particle, even if $\mu = 0$, i.e., the moment is obtained for a small γ_0 value. The reason for this behavior is that m_s is already saturated in the low-field region and thereafter behaves like μ. (3) With increasing values of $\beta^2/2\gamma''$ and/or $\rho_s^2/2\gamma''$ (Figure IV-3-3a—c), the magnitude of the maximum increases, while the position shifts to higher-field side. In all cases, values of Φ tend to decrease monotonically with increasing γ_0 value.

Figure IV-3-4 shows the PD-SUSID orientation function for disklike particle normalized by the limiting low-field function (eq 37), for which m_s is not saturated yet. This type of plot is very useful to analyze the experimental data with theoretical curves.[7] A few interesting facts became clear from Figure IV-3-4. Some of the normalized theoretical curves decrease monotonically with an increase in field strength, but others pass the maximum (Figure IV-3-4b, c), the position of which moves toward a higher field strength side and eventually disappears with an increase in the γ_0 (cf. Figure IV-3-4a—c). The condition for this behavior is not so simple as to be specified in the present theory, since the PD-SUSID orientation function for disklike particle contains three electric moments, which closely interplay with one another.

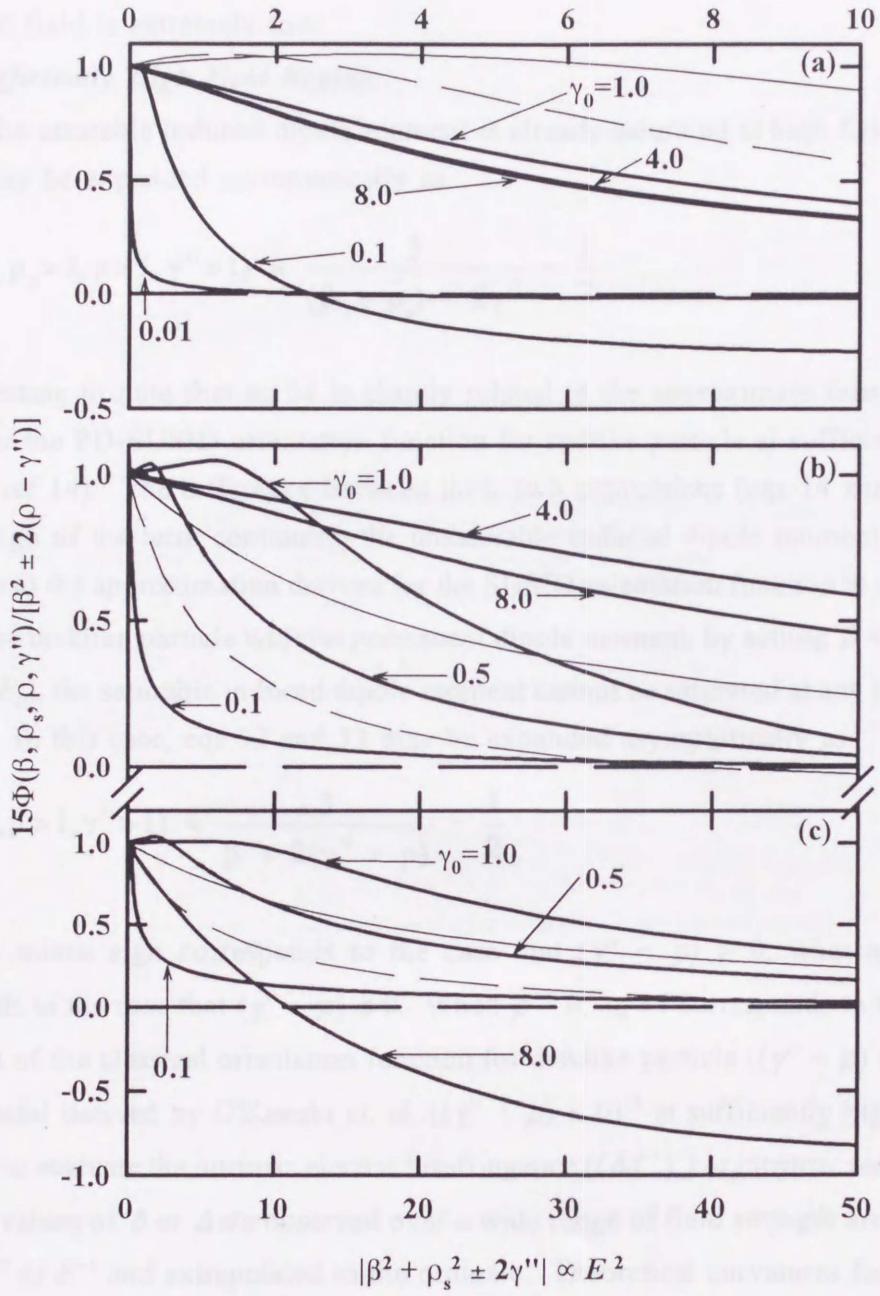

Figure IV-3-4. PD-SUSID orientation function for disklike particles, $15\Phi(\beta, \rho_s, \rho, \gamma'')/(\beta^2 \mp 2(\gamma'' - \rho))$. Parameters used for calculation are the same as in Figure IV-3-3. Note that the scale in (a) is expanded and different from (b) and (c).

IV. 3. 4. Two Limiting Cases of Field Orientation.

Approximate equations may be derived both for the sufficiently high field region, where the orientation of dispersed particles is about to be completed, and for the Kerr law region, where the applied field is extremely low.

The Sufficiently High Field Region.

When the saturable induced dipole moment is already saturated at high fields ($E \geq E_0$), eqs 21—29 may be expanded asymptotically as

$$\Phi(\beta \gg 1, \rho_s \gg 1, \rho \gg 1, \gamma'' \gg 1) \fallingdotseq \frac{3}{(\beta + \rho_s) - 2\gamma''} - \frac{1}{2} \tag{34}$$

It is interesting to note that eq 34 is closely related to the approximate formula, which was derived for the PD-SUSID orientation function for rodlike particle at sufficiently high fields (eq 12 of ref 14). The difference between these two expressions (eqs 14 and 12 (ref 14)) is only the sign of the term containing the unsaturable induced dipole moment. Moreover, eq 34 reduces to the approximation derived for the SUSID orientation function at sufficiently high field for the disklike particle without permanent dipole moment, by setting $\beta = 0$. If E_0 is very high ($E \leq E_0$), the saturable induced dipole moment cannot be saturated at any measurable field strengths. In this case, eqs 32 and 33 may be expanded asymptotically as

$$\Phi(\beta \gg 1, \rho \gg 1, \gamma'' \gg 1) \fallingdotseq \frac{3}{\beta \mp 2(\gamma'' - \rho)} - \frac{1}{2} \tag{35}$$

where the minus sign corresponds to the case that $(\gamma'' - \rho) \geq 0$, whereas the plus sign corresponds to the case that $(\gamma'' - \rho) \leq 0$. When $\rho = 0$, eq 35 corresponds to the approximate expression of the classical orientation function for disklike particle ($(\gamma'' - \rho) \geq 0$) and for the rodlike model derived by O'Konski *et. al.* ($(\gamma'' - \rho) \leq 0$)[34] at sufficiently high field.

In order to evaluate the intrinsic electric birefringence ($(\delta d^{-1})_\infty$) or intrinsic reduced dichroism ($(\Delta\epsilon/\epsilon)_s$), values of δ or $\Delta\epsilon/\epsilon$ observed over a wide range of field strength are usually plotted against E^{-2} or E^{-1} and extrapolated to the ordinate. Theoretical curvatures for this procedure may be visualized in Figure IV-3-5, where Φ is plotted against the parameter $(\beta^2 + \rho_s^2 \pm 2\gamma'')^{-1}$ (proportional to E^{-2}), and in Figure IV-3-6, where Φ is plotted against the parameter $(\beta^2 + \rho_s^2 \pm 2\gamma'')^{-0.5}$ (proportional to E^{-1}). In Figures IV-3-5 and 6, all theoretical curves approach either rapidly or slowly but finally to -0.5 in the extremely high field region. Therefore, if measurements can be carried out to such high fields that $\Phi(\beta, \rho_s, \rho, \gamma'') \geq |0.3|$, the intrinsic

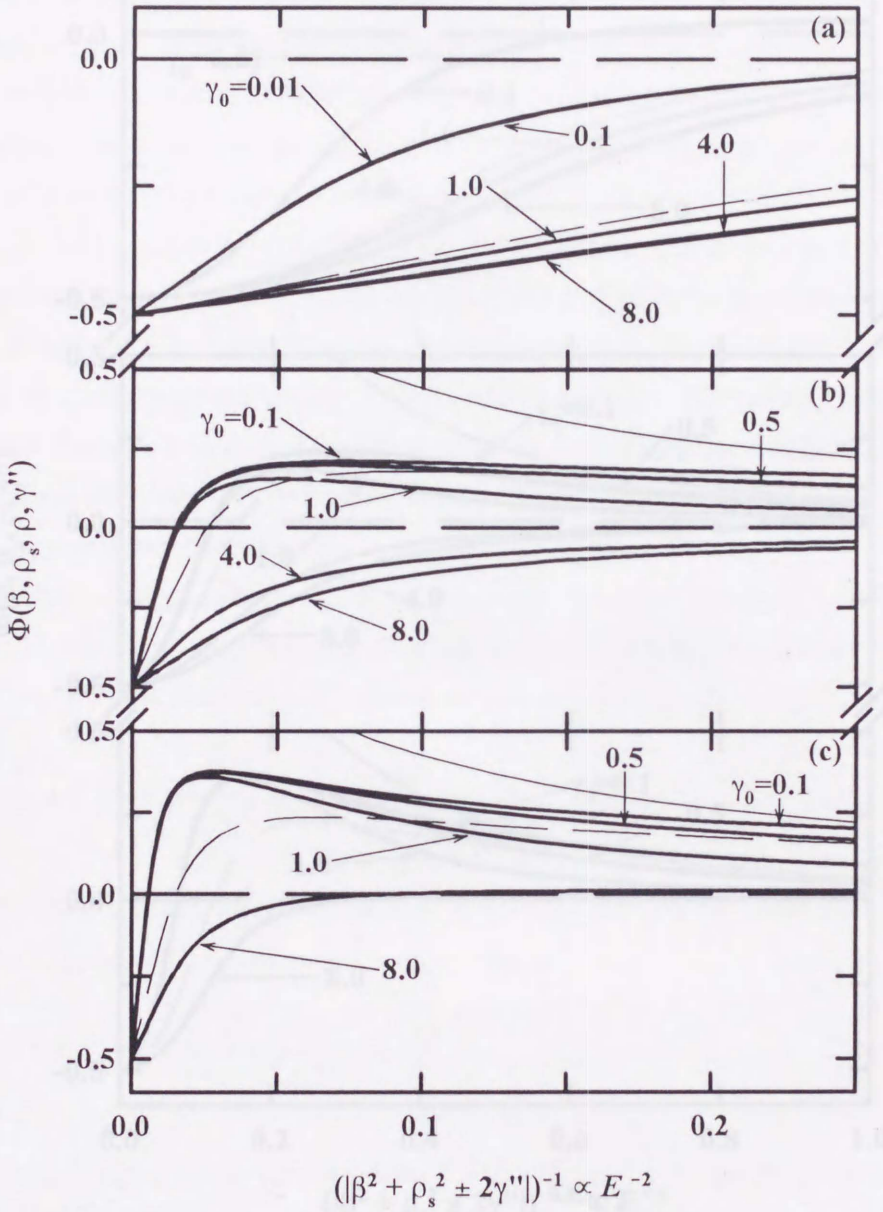

Figure IV-3-5. PD-SUSID orientation function for disklike particles, $\Phi(\beta, \rho_s, \rho, \gamma'')$, plotted against $(|\beta^2 + \rho_s^2 \pm 2\gamma''|)^{-1}$. Parameters used for calculation are the same as in Figure IV-3-3.

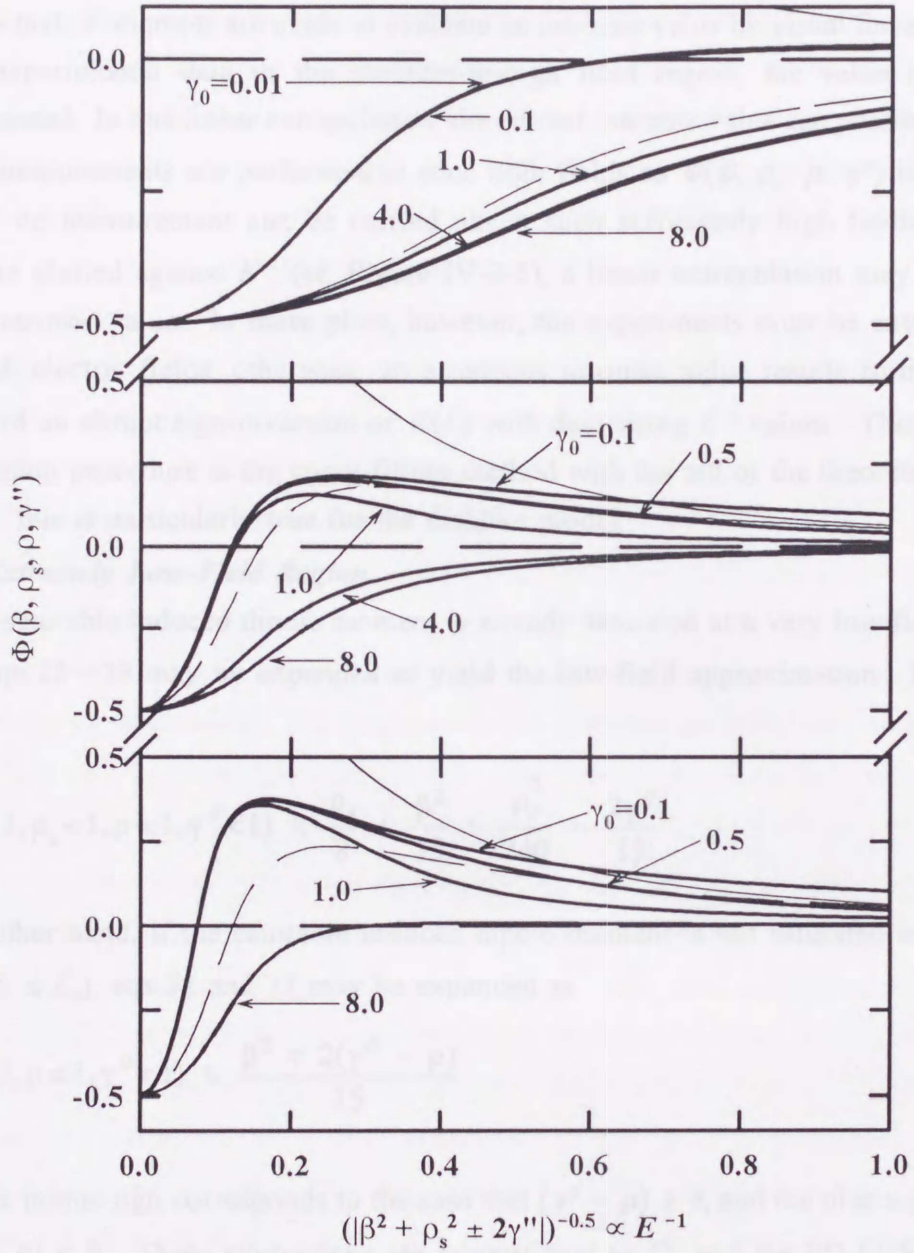

Figure IV-3-6. PD-SUSID orientation function for disklike particles, $\Phi(\beta, \rho_s, \rho, \gamma'')$, plotted against $(|\beta^2 + \rho_s^2 \pm 2\gamma''|)^{-0.5}$. Parameters used for calculation are the same as in Figure IV-3-3.

value may be evaluated at high accuracy, by extrapolating observed values to high fields by linear least squares method. Actually, it is impossible, however, to extend measurements to sufficiently high fields. Hence, the extrapolation procedure should be carried out with the aid

of the theoretical orientation function to evaluate the intrinsic birefringence.

The plots in Figures IV-3-5 and 6 have advantages as well as disadvantages. Each curve in Figure IV-3-6 approaches −0.5 slowly, after passing through an inflection point. This result indicates that, if attempts are made to evaluate an intrinsic value by visual linear extrapolation of the experimental data in the medium-to-high field region, the value is undoubtedly overestimated. In this linear extrapolation, the correct intrinsic value can possibly be obtained, only if measurements are performed in such high fields as $\Phi(\beta, \rho_s, \rho, \gamma'')$ is above $|0.48|$. Actually no measurement can be carried out at such sufficiently high fields. If observed points are plotted against E^{-2} (cf. Figure IV-3-5), a linear extrapolation may yield a nearly correct intrinsic value. In these plots, however, the experiments must be extended to cover very high electric fields, otherwise, an erroneous intrinsic value results from extrapolation because of an abrupt sign-inversion of $\Phi(E)$ with decreasing E^{-2} values. Therefore, the best extrapolation procedure is the curve-fitting method with the aid of the theoretical orientation function; this is particularly true for the disklike model.

The Extremely Low-Field Region.

If the saturable induced dipole moment is already saturated at a very low field strength ($E \geq E_0$), eqs 22—29 may be expanded to yield the low-field approximation. Equation 21 is given as

$$\Phi(\beta \ll 1, \rho_s \ll 1, \rho \ll 1, \gamma'' \ll 1) \fallingdotseq \frac{\rho_s}{8} + \frac{\beta^2}{15} + \frac{\rho_s^2}{240} - \frac{2\gamma''}{15} \tag{36}$$

On the other hand, if the saturable induced dipole moment is not saturated in the low-field region ($E \leq E_0$), eqs 32 and 33 may be expanded as

$$\Phi(\beta \ll 1, \rho \ll 1, \gamma'' \ll 1) \fallingdotseq \frac{\beta^2 \mp 2(\gamma'' - \rho)}{15} \tag{37}$$

where the minus sign corresponds to the case that $(\gamma'' - \rho) \geq 0$, and the plus sign corresponds to $(\gamma'' - \rho) \leq 0$. These expressions are proportional to E^2, and the PD-SUSID orientation function for disklike particles should also contain the Kerr region at extremely low fields in the same manner as the function for the rodlike model.[14] Equation 37 is identical to the approximation derived by O'Konski *et al.*,[34] if $(\gamma'' - \rho) \leq 0$, and by Shah,[23] if $(\gamma'' - \rho) \geq 0$, provided that ρ is set to nil. On the other hand, eq 36 is complex; the first term is proportional to E, but not to E^2, while the following three terms are proportional to E^2. These results are in accord with a previous report of the PD-SUSID orientation function for rodlike

particle.[14] Therefore, if the saturable induced dipole moment is already saturated in the extremely low-field region, the field-strength dependence of the steady-state electric birefringence (or electric dichroism) would show the non-Kerr-law behavior even at extremely low fields. In fact, Yamaoka and Charney[35] and Yamaoka *et al.*[7] have already observed this phenomenon (the steady-state electric birefringence is apparently proportional to E) with a high-molecular-weight DNA sample. However, no such anomalous trend has yet been observed for the disk-shaped particle. If β is set to zero, these equations all reduce to the SUSID orientation function for disklike particle in the low-field region.

IV. 3. 5. Comparison with Experimental Data of Montmorillonite.

The PD-SUSID orientation function for disklike particle derived in the preceding sections is now compared with the steady-state electric birefringence of montmorillonite dispersed in an aqueous medium, which shows an anomalous behavior of the sign inversion in steady-state electric birefringence in the low-field region.

Field Orientation of Montmorillonite.

Figure IV-3-7a shows the field-strength dependence of the steady-state electric birefringence of montmorillonite particle dispersed in a 0.1×10^{-3} moldm^{-3} NaCl aqueous medium. The concentration of the dispersed sample was determined to be 0.227 gdm^{-3} by measuring the dry weight of a clay suspension. The preparation and characterization of this sample suspension are described in ***Chapter V*** in detail. Electric birefringence measurements were performed at 25°C and 633 nm on a laser electric birefringence apparatus, which was constructed in our laboratory, and the details are given in ***Chapter III.*** The sign of δ values plotted against E^2 reverses from negative to positive at a low-field strength of E^2 of ca. 0.013 (kV/cm)^2 (cf. Insert in Figure IV-3-7a) with a minimum at ca. 52 V/cm. This field dependence is characteristic of the PD-SUSID curve for disklike particle under certain conditions. The agreement between the experimental points and the theoretical curve (solid line in Figure IV-3-7a) is excellent over the entire field region with a set of parameters $\beta^2/2\gamma''$, $\rho_s^2/2\gamma''$, and γ_0 being chosen to be 0, 0.1, and 0.01, respectively. The case that $\beta^2/2\gamma'' = 0$ clearly indicates that the electric permanent dipole moment μ is nil and that the PD-SUSID reduces to the SUSID orientation function for disklike particles. Thus, the montmorillonite particle possesses no permanent dipole moment, contrary to the original idea by Shah.[23] The best-fitted classical orientation function of Shah (dotted line, $\beta^2/2\gamma = -2$) was compared in Figure IV-3-7. The agreement between Shah's theoretical curve and the experimental data was not good, particularly in the low field region. The curve fitted to experimental values shows the sign inversion at ca. 114 V/cm with increasing field strengths, after the δd^{-1} values reach a minimum at extremely low

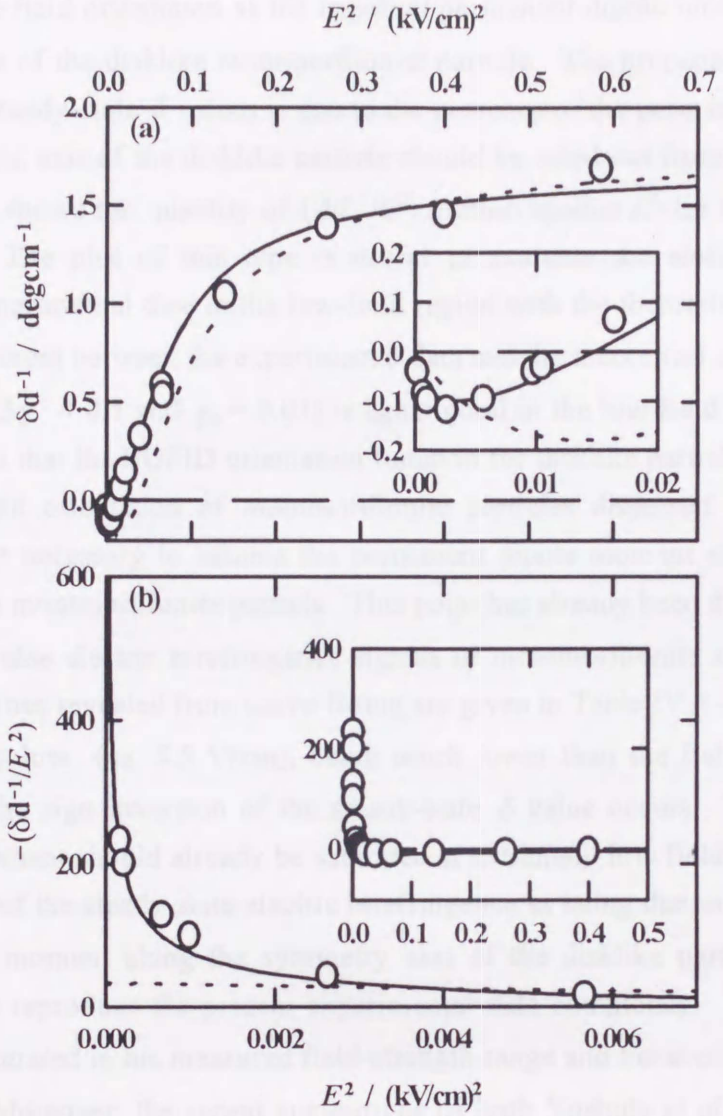

Figure IV-3-7. Field strength dependence of the steady-state electric birefringence of montmorillonite suspension: (a) the optical phase retardation per path length d of a Kerr cell, δd^{-1}, in deg cm^{-1}, versus the second power of applied electric field strength E^2; (b) the δd^{-1} divided by E^2, ($\delta d^{-1}/E^2$), in deg cm kV^{-2}; (○) the experimental data. The solid line is the best-fitted theoretical orientation function (see text for details). The dotted line is the best-fitted classical orientation function (see text for details). Inserts: The abscissa was expanded in (a) and contracted (b).

fields (ca. 52 V/cm). This behavior against field strengths is associated with the fact that the saturable induced dipole moment is already saturated in the extremely low-field region,

contributing to the field orientation as the *apparent* permanent dipole moment induced along the symmetric axis of the disklike montmorillonite particle. The proposal by Shah[23] that the sign inversion of steady-state δ values is due to the presence of the permanent dipole moment along the symmetric axis of the disklike particle should be ruled out from the present results.

Figure IV-3-7b shows the quantity of $(\delta d^{-1}/E^2)$ plotted against E^2 for the same data as in Figure IV-3-7a. The plot of this type is useful to evaluate the electric parameters, by comparing the experimental data in the low-field region with the theoretical curves in Figure IV-3-4. The agreement between the experimental data and the theoretical curve with a $\beta^2/2\gamma''$ value of zero ($\rho_s^2/2\gamma'' = 0.1$ and $\gamma_0 = 0.01$) is again good in the low-field region. This result supports the notion that the SUSID orientation function for disklike particles is also sufficient to explain the field orientation of montmorillonite particles dispersed in aqueous media. Therefore, it is not necessary to assume the permanent dipole moment along the symmetric axis of the disklike montmorillonite particle. This point has already been demonstrated clearly by the reversing-pulse electric birefringence signals of montmorillonite suspension.[26,27] The electrooptic properties revealed from curve-fitting are given in Table IV-3-2. The critical field strength E_0 is very low (ca. 5.5 V/cm), being much lower than the field strength (ca. 114 V/cm), at which the sign inversion of the steady-state δ value occurs. Thus, the saturable induced dipole moment should already be saturated at extremely low fields. Shah interpreted the sign inversion of the steady-state electric birefringence as being due to the presence of the permanent dipole moment along the symmetry axis of the disklike particle.[23] His theory, however, failed to reproduce the present experimental data completely. The fact is that the m_s was already saturated in his measured field-strength range and behaved like the permanent dipole moment. Moreover, the recent suggestions of both Yoshida *et al.*[24] and Yamaoka *et al.*[26,27] also support the present result.

Table IV-3-2. Electrooptical Properties of Montmorillonite Suspension Evaluated from Steady-State Electric Birefringence by the PD-SUSID Curve-Fitting Method

$\beta^2/2\gamma''$	$\rho_s^2/2\gamma''$	γ_0	μ	$\Delta\alpha''$	$\Delta\sigma$	E_0	$(\delta/cd)_\infty$[a]
			Cm	Fm^2	Fm^2	Vcm^{-1}	
0	0.1	0.01	0	5.4×10^{-29}	2.7×10^{-28}	5.5	-15.0

a) The unit of this value is in $degdm^3g^{-1}cm^{-1}$. This vaule is given by $(\delta d^{-1})(-2/c)$, where c is the mass concentration ($c = 0.227\ gdm^{-3}$).

IV. 4. Rotational Relaxation

The field-off electric birefringence decay signal yields information on the hydrodynamic size of dispersed particle. When a sample is monodisperse, the decay signal is usually expressed with a single-exponential curve. The decay signal of a polydisperse system, however, can not be expressed with such a curve because of the distribution of size, length, and so on. When the distribution is considered, the decay signal is given as[36]

$$\Delta n(t) = \sum_i \Delta n_{st,i} e^{-t/\tau_i} \tag{38}$$

where τ_i is the rotational relaxation time of the ith component, $\Delta n_{st,i}$ is the electric birefringence of the ith component at t = 0, i.e., the steady-state electric birefringence.

The decay signal is analyzed according to two methods: (1) the peeling method, which presumes that the signal is the sum of single exponential curves,[36] and (2) the area method, in which the area surrounded between the measured decay curve and the baseline yields the birefringence-average relaxation time, $<\tau>_{EB}$.[37] According to (1), the relaxation time $<\tau>_{EB}$ was defined as

$$<\tau>_{EB} = \sum_i a_i \tau_i, \quad \text{and} \quad \sum_i a_i = 1 \tag{39}$$

where a_i is the relaxation intensity of the ith component. In the case of (2), $<\tau>_{EB}$ is given as

$$<\tau>_{EB} = \int_0^\infty \frac{\Delta n(t)}{\Delta n_{st,i}} dt \tag{40}$$

Values of $<\tau>_{EB}$, obtained by either methods for the sample with a size distribution, show the field-strength dependence because of the different orientation degree of each component at a given field strength. In order to estimate the rotational relaxation time at complete orientation, the measured $<\tau>_{EB}$ values are extrapolated to infinitely high fields. The relaxation time obtained from such an extrapolation reduces to the weight-average rotational relaxation time τ_w. The weight-average diameter $<d>_w$ of a very thin oblate ellipsoid particle may be evaluated from τ_w as[37]

$$\langle d \rangle_w = \left[\frac{9kT\tau_w}{2\pi\eta_0} \right]^{1/3} \quad (41)$$

where η_0 is the viscosity of solvent, k is the Boltzmann coefficient, and T is the absolute temperature.

References

1. O'Konski, C. T.; Zimm, B. H. *Science* **1950**, *111*, 113.
2. Yoshioka, K.; Fujimori, M; Yamaoka, K.; Ueda, K. *Int. J. Biol. Macromol.* **1982**, *4*, 55.
3. Yamaoka, K.; Matsuda, K. *Macromolecules* **1981**, *14*, 595.
4. Yoshioka, K. In *molecular Electro-Optics*; O'Konski, C. T., Ed.; Marcel Dekker: New York, 1978; Part 2, Chapter 17, pp 601—643.
5. Yamaoka, K.; Fukudome, K. *J. Phys. Chem.* **1988**, *92*, 2779.
6. Yamaoka, K.; Fukudome, K. *J. Phys. Chem.* **1990**, *94*, 6896.
7. Yamaoka, K.; Fukudome, K.; Matsuda, K. *J. Phys. Chem.* **1992**, *96*, 7132.
8. Yamaoka, K.; Matsuda. K. *Macromolecules* **1980**, *13*, 1558.
9. Stellwagen, N. C. *Biopolymers* **1981**, *20*, 399.
10. Stellwagen, N. C. *Biophys. Chem.* **1982**, *15*, 311.
11. Matsuda, K.; Yamaoka, K. *Bull. Chem. Soc. Jpn.* **1982**, *55*, 69.
12. Charney, E.; Yamaoka, K. *Biochemistry* **1982**, *21*, 834.
13. Tanigawa, M.; Fukudome, K.; Yamaoka, K. *J. Sci. Hiroshima Univ. Ser. A* **1994**, *58*, 123.
14. Yamaoka, K.; Kimura, M; Okada, M. *Bull. Chem. Soc. Jpn.* **1992**, *65*, 129.
15. Krămer, U.; Hoffmann, H. *Macromolecules* **1991**, *24*, 256.
16. Soda, T.; Yoshioka, K. *Nippon Kagaku Zasshi* **1965**, *86*, 1019.
17. Yoshioka, K. *J. Chem. Phys.* **1983**, *79*, 3482.
18. Yamaoka, K.; Hino, Y. *Bull. Chem. Soc. Jpn.* **1989**, *62*, 251.
19. Yamaoka, K.; Yamamoto, S.; Kimura, M.; Kosako, I. *Polym. J.* **1991**, *23*, 1443.
20. Yamaoka, K; Ueda. K. *Chem. Lett.* **1983**, 545.
21. Tinoco, I., Jr. *J. Am. Chem. Soc.* **1955**, *77*, 4486.
22. O'Konski, C. T.; Bergmann, K. *J. Chem. Phys.* **1962**, *37*, 1573.
23. Shah, M.J. *J. Phys. Chem.* **1963**, *67*, 2215.
24. Yoshida, M.; Hayashi, M; Kikuchi, K.; Watanabe, H. In *Dynamic Behavior of Macromolecules, Colloids, Liquid Crystals and Biological Sytems by Optical and Electrooptical Methods*; Hirokawa: Tokyo, 1989; pp 349—355.
25. Yamagishi, A.; Soma, M. *J. Phys. Chem.* **1981**, *85*, 3090.
26. Yamaoka, K.; Sasai, R.; Ikuta, N. *Chem. Lett.* **1994**, 563.
27. Yamaoka, K.; Tanigawa, M.; Sasai, R. *J. Chem. Phys.* **1994**, *101*, 1625.

28. Tinoco, I., Jr.; Yamaoka, K. *J. Phys. Chem.* **1959**, *63*, 423.

29. Takezoe, H.; Yu, H. *Biochemistry* **1981**, *20*, 5275.

30. Takezoe, H.; Yu, H. *Biophys. Chem.* **1981**, *13*, 49.

31. Yamaoka, K.; Matsuda, K. *J. Phys. Chem.* **1985**, *89*, 2779.

32. Szabo, A.; Haleem, M.; Eden, D. *J. Chem. Phys.* **1986**, *85*, 7472.

33. Oosawa, F. *Polyelectrolytes*; Marcel Dekker: New York, 1971; Chapter 5, pp 51—70.

34. O'Konski, C. T.; Yoshioka, H.; Orttung, W. H. *J. Phys. Chem.* **1959**, *63*, 1558.

35. Yamaoka, K.; Charney, E. *Macromolecules* **1973**, *6*, 66.

36. Fredericq, E.; Houssier, C. *Electric Dichroism and Electric Birefringence*; Clarendon Press: Oxford, 1973.

37. Yamaoka, K.; Fukudome, K.; Matsumoto, S.; Hino, Y. *J. Colloid Interface Sci.* **1994**, *168*, 349.

38. Perrin, F. *J. Phys. Radium* **1934**, *5*, 497.

— *Chapter V.* —

Effect of Particle Concentration, Ionic Strength, and Valence of Electrolyte on Electrooptical Properties of Montmorillonite Particles in Aqueous Media

V. 1. Introduction

The electrooptical study of montmorillonite particles in aqueous media was initiated by O'Konski and Zimm with a DC electric field.[1] They observed a sign reversal of steady-state electric birefringence from negative to positive with increasing field strengths.[1-5] Subsequently, Shah *et al.* have explained this phenomenon by assuming the out-of-plane transverse *permanent dipole moment* in the disklike particle.[2] From electric birefringence measurements with samples at various concentrations and diameters of particles, Yoshida *et al.*, however, suggested that the particle possessed no such transverse *permanent dipole moment*.[3] Using a new reversing-pulse generator, we have also studied the electrooptical properties of montmorillonite dispersed in aqueous media by the reversing-pulse electric birefringence method (hereafter abbreviated as RPEB).[5-7] These results indicated that montmorillonite particle has no *permanent dipole moment*, and that the ion-induced dipole moment, which is slowly induced with applied field and saturated at a certain field strength, was responsible for the anomalous sign-reversal, i.e., the phenomenon that the sign of the steady-state electric birefringence reverses from negative to positive.[5-7] On the basis of these results,[5-7] we suggested that the field orientation of montmorillonite particle results from the following mechanism. At extremely low fields (steady-state electric birefringence is negative), the symmetric axis of the particle is parallel to the direction of an applied electric field, but this symmetric axis turns to be perpendicular to the field direction at moderately high-fields (steady-state electric birefringence is positive). Effects of particle concentration, ionic strength, and valence of added electrolyte on these phenomena and properties of montmorillonite, however, have not been clear yet. Clarifying these effects may be important to know the origin and mechanism of static electric phenomena on the clay surface, colloidal chemical properties of clay, and so on. In this chapter, quantitative studies by the new RPEB apparatus will be presented on the effects of the concentration of montmorillonite particles, and the ionic strength and valence of added electrolyte on the field orientation.

V. 2. Experimental

V. 2. 1. Preparation of Montmorillonite Suspension.

A montmorillonite sample (K10), purchased from Aldrich Chemical Co., was used. The suspension of montmorillonite was prepared in the following steps. (1) The K10 sample was added to double-distilled water under stir and the suspension was kept being stirred for two days. (2) To convert the counterion to sodium ions, the solvent was first replaced with 0.3 $moldm^{-3}$ NaCl, by adding a high concentration NaCl solution to sample (1) under stir, and the suspension was stirred for an additional day. (3) To dissociate and disperse aggregated particles, the suspension was sonicated at 0 °C at a power level of 200 W (20 kHz) for 20 min. (4) To remove the remaining metal ions, ethylenediaminetetraacetic acid disodium salt (Na_2EDTA) was added to the suspension, which was then dialyzed against 0.3 $moldm^{-3}$ NaCl for one day to remove excess Na_2EDTA. (5) To make the suspension salt-free, dialysis against the double-distilled water (8 dm^3) was continued for four days. (6) To dissociate and disperse particles re-aggregated in the course of the dialysis against 0.3 $moldm^{-3}$ NaCl, sample (5) was sonicated under the same condition as (3). (7) To remove the remaining aggregates or large-size particles, centrifugation was performed at 3,000 rpm for 20 min. The supernatant was collected and used as the stock suspension. This supernatant was then stored at room temperature.

The concentration of stock suspension was estimated to be 0.29 gdm^{-3}, by measuring the weight of the anhydrous sample prepared by the freeze-drying and subsequently heat-drying method *in vacuo*. For RPEB measurements, the stock suspension was diluted with double-distilled water (the concentration dependence) and with NaCl solution (the ionic-strength dependence). Na^+ counterions were replaced with Mg^{2+} ions by dialyzing the stock Na-montmorillonite suspension first against 0.1 $moldm^{-3}$ $MgCl_2$ solution for a day, and then against the double-distilled water (8 dm^3) for four days. This dialyzed suspension was used as the salt-free Mg-montmorillonite suspension, to which $MgCl_2$ solution was added to prepare samples at various ionic strengths.

V. 2. 2. Electron Microscopic Photograph of Montmorillonite Particles.

From an electron-microscopic photograph, the average diameter of Na-montmorillonite particles was estimated to be ca. 275 nm.[8] Particles are not a truly circular disk but rather fractal, showing no specific shape, and also are not monodisperse, but polydisperse in size in the dried suspension.[8]

V. 3. Na-montmorillonite Suspensions.

In this section, descriptions are given of the effect of the particle concentration and the ionic strength of the sodium ion on the electrooptical and hydrodynamic properties of Na-montmorillonite particles.

V. 3. 1. Reversing Transition Signals.

In Figure V-3-1, typical RPEB transient signals of Na-montmorillonite suspension (c = 0.029 gdm^{-3} and Is = 0) are illustrated. Signals of the *negative* sign with deep dip (thick

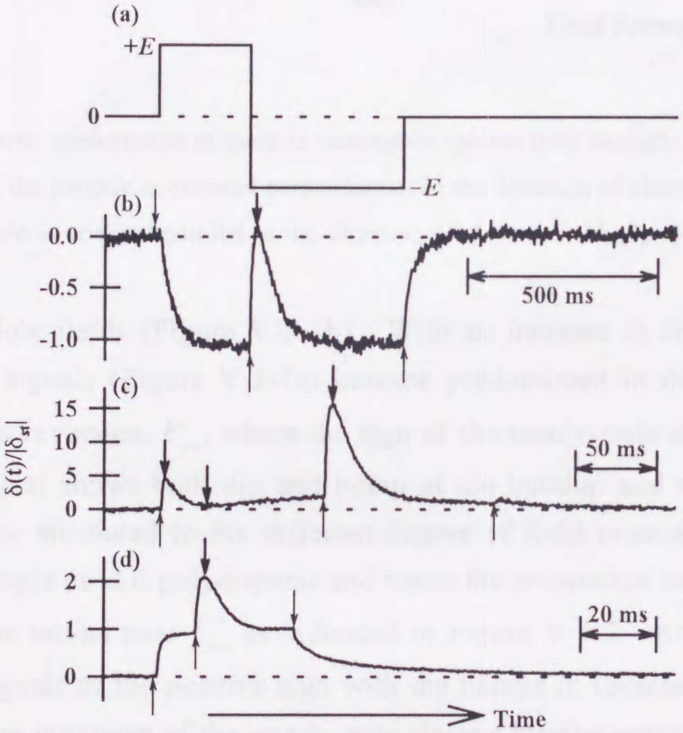

Figure V-3-1. RPEB signals of Na-montmorillonite suspension normalized by the absolute magnitude of steady-state phase retardation $|\delta_{st}|$. A schematic reversing-pulse pattern (a). RPEB signals without added sodium ion at c = 0.029 gdm^{-3} (b—d): (b), E = 22 Vcm^{-1} and δ_{st}/cd = -0.42 degdm^{3}g^{-1}cm^{-1}; (c), E = 91 Vcm^{-1} and δ_{st}/cd = 0.12 degdm^{3}g^{-1}cm^{-1}; (d), E = 179 Vcm^{-1} and δ_{st}/cd = 2.89 degdm^{3}g^{-1}cm^{-1}. Thick arrows indicate the positions of maximum and minimum. Thin arrows show the field-on, reverse, and field-off points of applied electric pulses. Note the change of time scale of signals in parts.

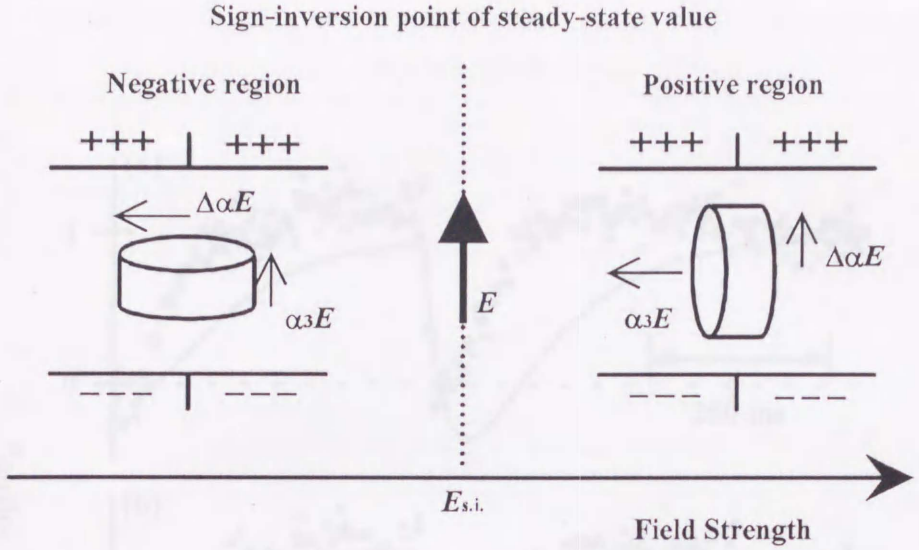

Figure V-3-2. Schematic presentation of particle orientation against field strength. Below the sign-inversion field $E_{s.i.}$, the plane of the particle is oriented perpendicular to the direction of electric field (left). Above $E_{s.i.}$, the plane of the particle is oriented parallel to the direction of electric field (right).

arrow) appear at low fields (Figure V-3-1b). With an increase in field strength, however, anomalous RPEB signals (Figure V-3-1c) become predominant in the vicinity of the field strength of the sign inversion, $E_{s.i.}$, where the sign of the steady-state electric birefringence is reversed. This signal shows both dip and hump at the buildup and reverse portions. This observation may be attributed to the different degree of field orientation of particle in the suspension; the sample used is polydisperse and hence the orientation axes of disklike particles of various sizes are mixed near $E_{s.i.}$ as indicated in Figure V-3-2. At field strengths higher than $E_{s.i.}$, RPEB signals of the *positive* sign with the humps in reverse process (thick arrow) appear after the sign inversion of the steady-state electric birefringence (Figure V-3-1d). The hump monotonically decreases with further increasing field strength, disappearing at higher field strengths. This disappearance of hump is probably due to the fact that the instantaneously induced dipole moment proportional to the field strength becomes predominant in field orientation. Similar phenomena are observed at higher concentrations of particles and added sodium ions.

Figure V-3-3 shows the analysis of a RPEB signal of the Na-montmorillonite suspension (c = 0.029 gdm^{-3}, Is = 0, E = 11 Vcm^{-1}) with two RPEB theories.[5,6,9] The solid line in Figure V-3-1a is the theoretical curve calculated from the TY theory (eq 1 in ***Chapter IV.***), by assuming the presence of the permanent dipole (μ) and induced dipole ($\Delta\alpha$) moments with a

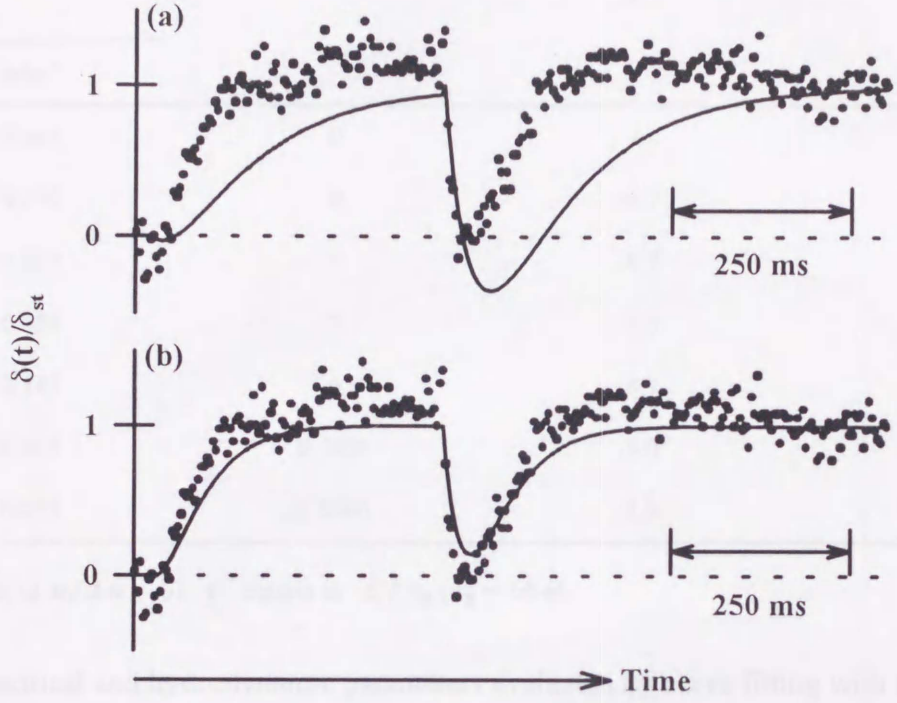

Figure V-3-3. Measured and simulated RPEB signals of Na-montmorillonite suspension. Dots: measured signal (b) in Figure V-3-1. The sampling time between two successive points in observed signal is 0.4 ms. Solid lines: simulated signals. Parameters for simulated curves: $<\tau>_{EB}$ = 39.8 ms and Q = -6.7 from the Tinoco-Yamaoka theory (eq 1) in (a) and $<\tau>_{EB}$ = 39.8 ms, τ_1 = 59.7 ms, and q = -6.7 from the Yamaoka-Tanigawa-Sasai theory (eqs 7—9) in (b).

ratio ($Q \equiv \mu^2/\Delta \alpha kT$ of −6.7).[9] This theoretical curve could reproduce no measured RPEB signals at any particle and added sodium ion concentrations. Thus, this result should be taken as the evidence that the Na-montmorillonite particle possesses no *permanent dipole moment.* The solid line in Figure V-3-3b is the theoretical curve calculated with eqs 7—9 in ***Chapter IV.***; it is in good agreement with all measured RPEB signals of the Na-montmorillonite suspension under the present condition. These results lead to the conclusion that the orientation of the Na-montmorillonite particle is due to the electric moment induced by *ion polarization* within the finite time after an application of electric pulse field.

Table V-3-1. Electrical and Hydrodynamic Properties of Na-montmorillonite Particles in Aqueous Media Estimated from RPEB Signals

c / gdm^{-3}	Is	q [a]	τ^* [b]
0.005	0	—	—
0.010	0	-6.7	1.4
0.029	0	-6.7	1.5
0.058	0	-5.0	1.9
0.145	0	-6.7	1.3
0.029	0.0001	-5.0	0.89
0.029	0.0005	-2.9	0.60

a) q equals to $\alpha_3/\Delta\alpha'$. b) τ^* equals to τ_1 / τ_θ ($\tau_\theta = 1/6\Theta$).

The electrical and hydrodynamic parameters evaluated by curve fitting with the YTS theory are given in Table V-3-1. The polarizability ratio, q, and the reduced relaxation time $\tau^* = \tau_1/\tau_\theta$ ($\tau_\theta = 1/6\Theta$), are nearly constant with particle concentration but decreased with increasing concentrations of added sodium ions. This result reflects that sodium ions trapped in cation-exchangeable sites become immobilized with the increase in ionic strengths, probably because of the predominant adsorption of the sodium ions onto the site. The result also supports the notion that the fluctuation of the trapped sodium ions on cation-exchangeable sites is responsible for the ion-atmosphere polarizability α_3.

V. 3. 2. Field-Strength Dependence of Steady-State Electric Birefringence.

Figure V-3-4 shows the field-strength dependence of the steady-state electric birefringence at various concentrations of particles and added sodium ions. The sign inversion of the steady-state electric birefringence was observed for all Na-montmorillonite samples in the low field region (cf. inserts of Figure V-3-4). The difference in the field strength dependence of the steady-state electric birefringence of each sample becomes obvious at increased particle concentrations and increased field strengths (Figure V-3-4a); moreover, the normalized quantity δ_{st}/cd at a given field strength decreases with increasing particle concentration. The decrease of the transmissivity of incident light with the increase in particle concentrations is observed; therefore, the origin of this decrease of δ_{st}/cd may be due to the increase in the

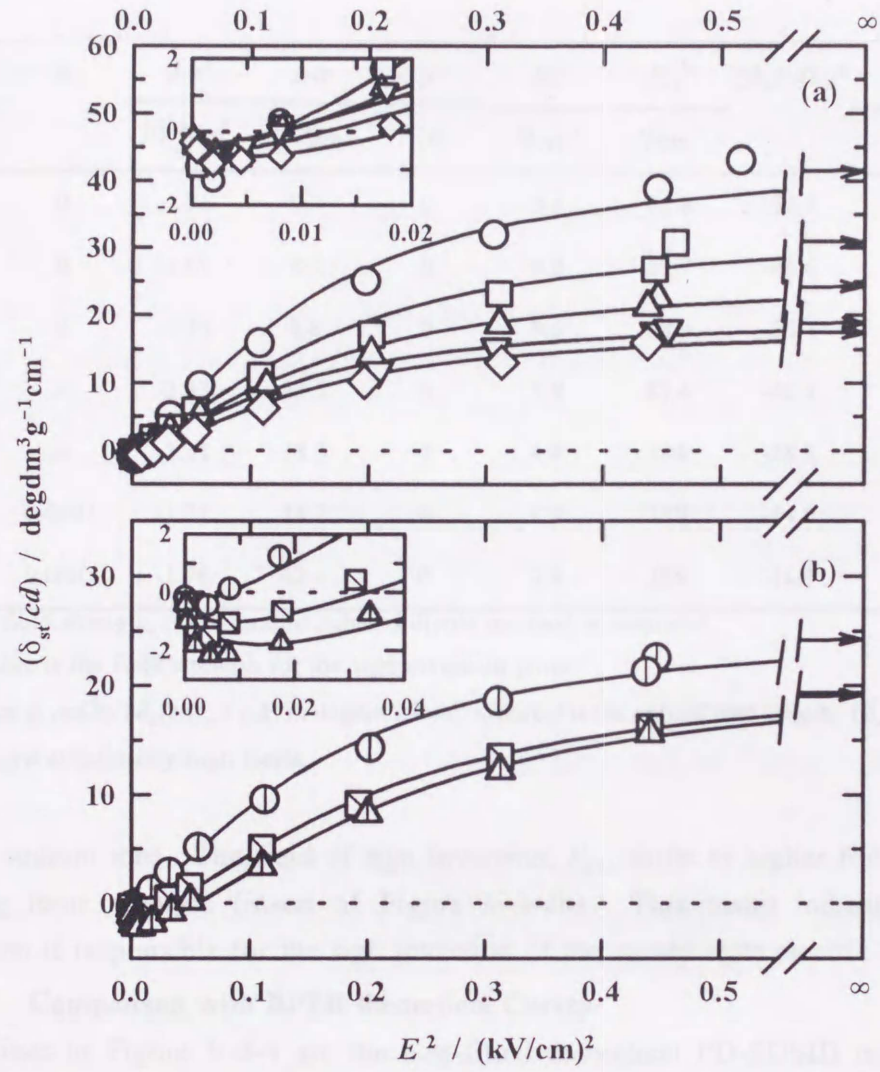

Figure V-3-4. Field-strength dependence of the steady-state electric birefringence of montmorillonite suspensions. The optical phase retardation per path length d of a Kerr cell (4 cm) normalized by the concentration of montmorillonite suspension c, (δ_{st}/cd) in degdm^{3}g^{-1} cm^{-1}, is plotted against the second power of applied electric field strength E^2. Symbols: experimental data. Solid lines: the best-fitted theoretical SUSID orientation functions. (a): data measured without added sodium ion; c = 0.005 gdm^{-3} (○), 0.010 (□), 0.029 (△), 0.058 (▽), 0.145 (◇). (b): data measured at various ionic strength Is of added sodium ion at a constant c (= 0.029 gdm^{-3}). Is = 0 (◑), 0.0001 (◪), 0.0005 (◭). Inserts in (a) and (b): the abscissa on an expanded scale. Values of δ_{st}/cd at infinite fields are indicated with arrows on the right ordinate.

forward light scattering intensity at higher particle concentrations. Figure V-3-4b shows the field strength dependence of the steady-state electric birefringence at various ionic strengths

Table V-3-2. Electrooptical and Hydrodynamic Properties of Na-montmorillonite Particles in Aqueous Media Evaluated from Field-Strength Dependence of Steady-State Electric Birefringence and Relaxation Time

c	Is	$\Delta\alpha'$	$\Delta\sigma$	μ	E_0 [a]	$E_{s.i.}$ [b]	$(\delta_{st}/cd)_{intr}$ [c]	τ_w	$\langle d\rangle_w$
gdm^{-3}		10^{-29}Fm^2	10^{-29}Fm^2	Cm	Vcm^{-1}	Vcm^{-1}		ms	nm
0.005	0	-1.86	9.3	0	9.3	65.8	-92.5	4.6	298
0.010	0	-1.69	8.5	0	9.8	69.7	-66.6	5.7	321
0.029	0	-1.75	8.8	0	9.6	68.3	-55.1	4.7	300
0.058	0	-2.33	23.3	0	5.9	83.4	-40.7	4.6	298
0.145	0	-2.22	33.3	0	4.9	104	-38.2	3.8	280
0.029	0.0001	-1.71	34.2	0	4.9	139	-44.0	4.2	290
0.029	0.0005	-1.78	62.4	0	3.9	179	-44.1	5.8	322

a) At this field strength, the saturable induced dipole moment is saturated.

b) This value is the field strength for the sign-inversion point.

c) Values are given by $(\delta_{st}/cd)_\infty \times (-2)$ in degdm^{3}g^{-1}cm^{-1}, where d is the optical path length. $(\delta_{st}/cd)_\infty$ is the limiting value of δ_{st}/cd at infinitely high fields.

of added sodium ions. The field of sign inversion, $E_{s.i.}$, shifts to higher field strengths with increasing ionic strength (insert of Figure V-3-4b). This result indicates that the ion polarization is responsible for the sign inversion of the steady-state electric birefringence.

V. 3. 3. Comparison with RPEB theoretical Curves.

Solid lines in Figure V-3-4 are the best-fitted theoretical PD-SUSID orientation curves calculated for the disklike particle.[7] The experimental field strength dependence of the steady-state electric birefringence was reproduced well with the PD-SUSID function in each case, even if the concentrations of particle and added sodium ions are varied widely. The electrooptical properties of the Na-montmorillonite particle, estimated from these best-fitted theoretical curves, are given in Table V-3-2. The result again indicates that the Na-montmorillonite particle possesses no *permanent dipole moment*; the notion already supported by RPEB data (Figure V-3-3b). This conclusion agrees with the previous reports,[5-7] and also with a report by Yoshida *et al.*,[3] in contrast with the results reported by Shah.[2] The polarizability, $\Delta\alpha'$, due to an unsaturable induced dipole moment and the polarizability, $\Delta\sigma$, responsible for a saturable induced dipole moment are constant in the low concentration range (at $c \leq 0.029$ gdm^{-3}), indicating that no interparticle electrostatic and hydrodynamic interaction

exists. However, the reduced saturated steady-state electric birefringence $(\delta_{st}/cd)_{intr}$ of dispersed particles, which reflects the optical property free from electric property, is largely changed. This decrease may be due to the increase in the forward light scattering at higher particle concentrations. In $c > 0.029$ gdm^{-3}, both $\Delta\alpha'$ and $\Delta\sigma$ are increased probably because of the occurrence of the interparticle electrostatic interactions between electric double layers of dispersed particles.

When the ionic strength of added sodium ions is increased, the $\Delta\alpha'$ value remains constant, whereas $\Delta\sigma$ is increased to saturation. This result indicates that $\Delta\sigma$ is associated with ion polarization; the saturation of ion-induced dipole moment is probably due to the predominant adsorption of added sodium ions onto cation-exchangeable sites. Since $\Delta\sigma$ values are larger than those of $\Delta\alpha'$, a large electric dipole moment transverse to the disk plane should be induced. The critical field strength, E_0, where the saturable induced dipole moment is saturated, is extremely low (cf. Table V-3-2). This result leads to the conclusion that Na ions adsorbed onto cation-exchangeable sites are responsible for the saturable induced dipole moment, $\Delta\sigma E$, and this dipole moment can easily be saturated at extremely low fields (ca. 4—10 Vcm^{-1}) because of the immobility of sodium ions on cation-exchangeable site. At low fields ($E \leq E_0$), the plane of disk is oriented perpendicular to the direction of applied external field because of predominant contribution of the saturable induced dipole moment $\Delta\sigma E$ to the field orientation (cf. Figure V-3-2a). At $E \geq E_0$ but $E \leq E_{s.i.}$, the saturable induced dipole moment is saturated, but the plane of disk is still oriented perpendicular to the field direction. Since the unsaturable induced dipole moment $\Delta\alpha' E$ is smaller than the saturable moment $\Delta\sigma E$, the plane of disklike particle changes at $E_{s.i.}$ from the perpendicular to parallel direction of applied field and remains as such at higher field (Figure V-3-2a). The sign inversion point $E_{s.i.}$ becomes higher with increasing sodium ions added to solution (Table V-3-2). This increase of $E_{s.i.}$ with ionic strength corresponds to the increase of the $\Delta\sigma$, indicating that the polarization of sodium ions adsorbed onto the cation-exchangeable sites is responsible for the sign-inversion phenomenon. The saturated steady-state electric birefringence $(\delta_{st}/cd)_{intr}$ is slightly decreased with increasing ionic strengths, which is probably due to formation of aggregates.

V. 3. 4. Field-Strength Dependence of $<\tau>_{EB}$.

Figure V-3-5 shows the field-strength dependence of the electric birefringence-average rotational relaxation time $<\tau>_{EB}$ of Na-montmorillonite particles. Since $<\tau>_{EB}$ values vary with field strengths, the present Na-montmorillonite sample should have the hydrodynamic size distribution; a fact clearly supported by electron microscopic observation. Values of $<\tau>_{EB}$

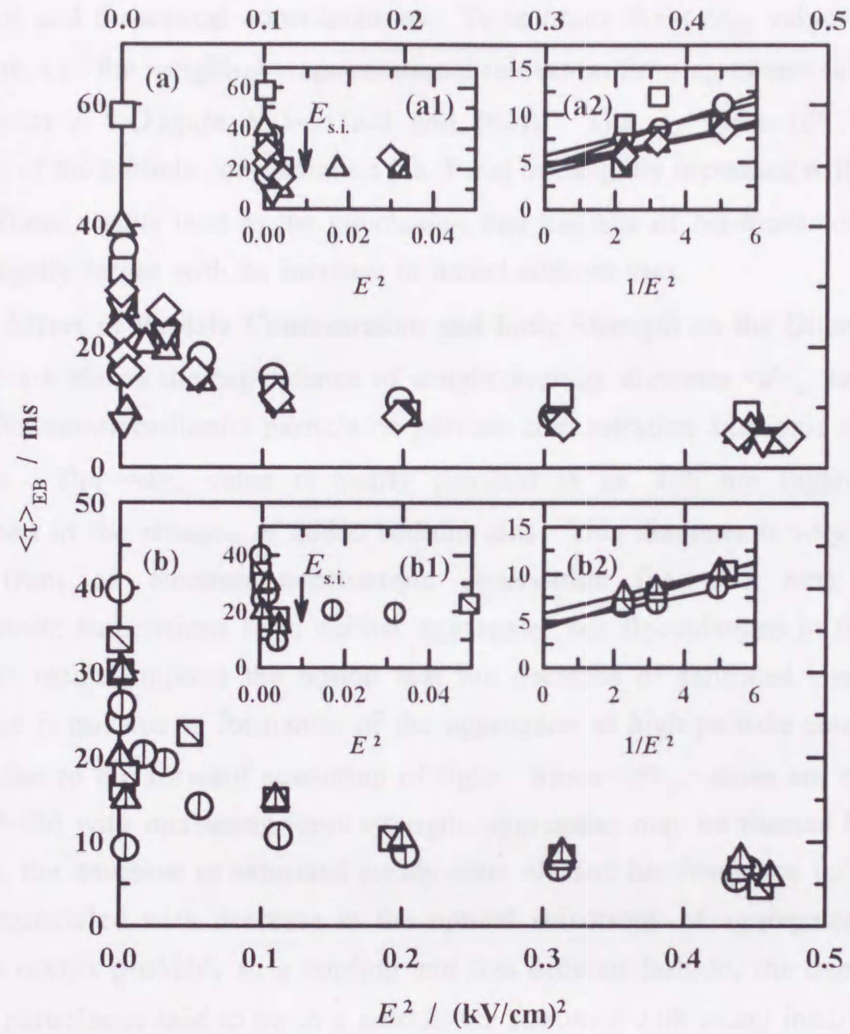

Figure V-3-5. Field-strength dependence of the electric birefringence-average rotational relaxation time $<\tau>_{EB}$ evaluated from the decay signal. (a): $<\tau>_{EB}$ at various concentrations of Na-montmorillonite particles in the absence of added sodium ion. (b): $<\tau>_{EB}$ at various ionic strengths at a constant Na-montmorillonite concentration (c = 0.029 gdm^{-3}). Symbols are the experimental data as given in Figure V-3-4. Inserts (a1) and (b1): the expanded abscissa. $E_{s.i.}$: the electric field strength at the sign inversion point. Inserts (a2) and (b2): $<\tau>_{EB}$, plotted against $1/E^2$ (in kV^{-2}cm^{-2}) at high fields. Four measured points at high fields are linearly extrapolated to infinitely high fields by the one-dimensional least squares method (solid lines).

show an anomalous field dependence near the $E_{s.i.}$, as indicated with arrows in (a1) and (b1). This anomaly is probably due to the change of an orientational axis (cf. Figure V-3-2a), since symmetry axis of disklike particle changes from the parallel to perpendicular direction of

applied electric field at $E_{s.i.}$, as noted in the above section. The hydrodynamic size distribution, however, may also lead to such an anomalous behavior, which is left open to further experimental and theoretical considerations. To estimate the $<\tau>_{EB}$ value at infinitely high field strength, i.e., the weight-average rotational relaxation time τ_w, observed $<\tau>_{EB}$ values are plotted against E^{-2} (Figure V-3-5 (a2) and (b2)). The τ_w value (cf. Table V-3-2) is independent of the particle concentration (ca. 5 ms) but slightly increased with increasing ionic strength. These results lead to the conclusion that the size of Na-montmorillonite particles becomes slightly larger with an increase in added sodium ions.

V. 3. 5. Effect of Particle Concentration and Ionic Strength on the Diameter.

Figure V-3-6 shows the dependence of weight-average diameter $<d>_w$, calculated from eq 41, of the Na-montmorillonite particle on particle concentration and ionic strength of added sodium ion. The $<d>_w$ value is nearly constant at ca. 300 nm regardless of particle concentrations in the absence of added sodium ions. This diameter is very close to the one estimated from an electron microscopic observation (ca. 275 nm); therefore, Na-montmorillonite suspensions form neither aggregates nor flocculations in this concentration range. This result supports the notion that the decrease of saturated steady-state electric birefringence is not due to formation of the aggregates at high particle concentrations (*vide supra*) but due to the forward scattering of light. Since $<d>_w$ values are slightly increased (Figure V-3-6b) with increasing ionic strength, aggregates may be formed by added sodium ions. Thus, the decrease in saturated steady-state electric birefringence (cf. Figure V-3-4b) should be associated with decrease in the optical anisotropy of aggregated particles. The aggregation occurs probably in a random and less ordered fashion; the overall shape of the aggregated particles is said to be in a *card-house structure* with many inner cavities.[10,11]

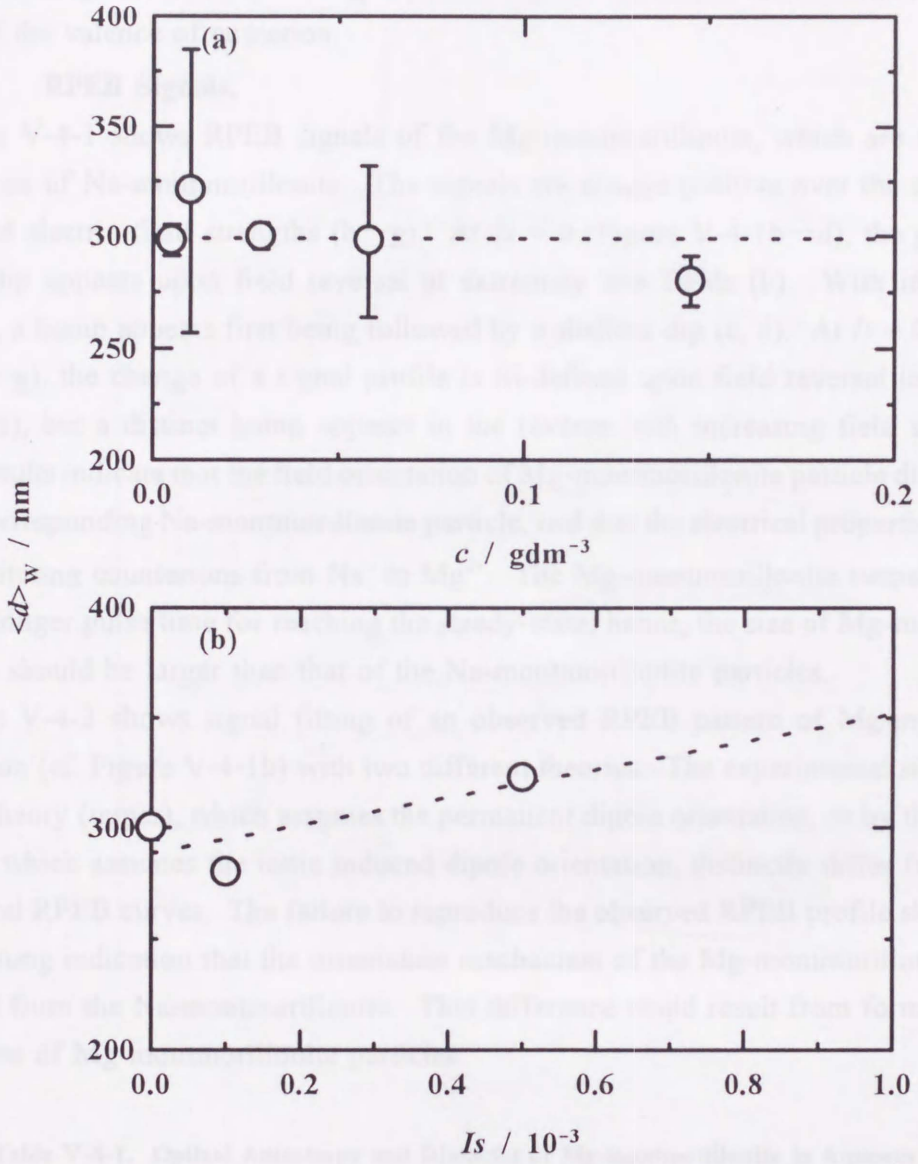

Figure V-3-6. Dependence of the weight-average diameter $\langle d \rangle_w$ of Na-montmorillonite particle on particle concentration and ionic strength. (a): $\langle d \rangle_w$ at various particle concentrations in the absence of added sodium ions. (b): $\langle d \rangle_w$ at various ionic strengths and at a constant particle concentration (c = 0.029 gdm^{-3}).

V. 4. Mg-montmorillonite Suspension.

The birefringence behavior of Mg-montmorillonite suspension is described to ascertain the effect of the valence of couterion.

V. 4. 1. RPEB Signals.

Figure V-4-1 shows RPEB signals of the Mg-montmorillonite, which are quite different from those of Na-montmorillonite. The signals are always positive over the entire range of measured electric field strengths (b—g). At Is = 0 (Figure V-4-1b—d), the positive signal with a dip appears upon field reversal at extremely low fields (b). With increasing field strength, a hump appears first being followed by a shallow dip (c, d). At Is = 0.0001 (Figure V-4-1e—g), the change of a signal profile is ill-defined upon field reversal in the low field region (e), but a distinct hump appears in the reverse with increasing field strength (f, g). These results indicate that the field orientation of Mg-montmorillonite particle differs from that of the corresponding Na-montmorillonite particle, and that the electrical properties are changed by substituting counterions from Na^+ to Mg^{2+}. The Mg-montmorillonite suspension requires a much longer pulse time for reaching the steady-state; hence, the size of Mg-montmorillonite particles should be larger than that of the Na-montmorillonite particles.

Figure V-4-2 shows signal fitting of an observed RPEB pattern of Mg-montmorillonite suspension (cf. Figure V-4-1b) with two different theories. The experimental signal, fitted by the TY theory (upper), which assumes the permanent dipole orientation, or by the YTS theory (lower), which assumes the ionic induced dipole orientation, distinctly differ from these two theoretical RPEB curves. The failure to reproduce the observed RPEB profile should be taken as the strong indication that the orientation mechanism of the Mg-montmorillonite particle is different from the Na-montmorillonite. This difference could result from formation of large aggregates of Mg-montmorillonite particles.

Table V-4-1. Optical Anisotropy and Diameter of Mg-montmorillonite in Aqueous Media

c	Is	$(\delta_{st}/cd)_{intr}$ [a]	τ_w	$\langle d \rangle_w$ [b]
gdm^{-3}		$degdm^3g^{-1}cm^{-1}$	ms	μm
0.065	0	-51.9	235	1.11
0.065	0.0001	-78.1	322	1.23

a) This value is given by $(\delta_{st}/cd)_\infty \times (-2)$, where d is the optical path length. $(\delta_{st}/cd)_\infty$ is δ_{st}/cd at infinitely high fields.

b) The diameter of disk obtained from Perrin's equation (eq 41) for an oblate ellipsoid of revolution.

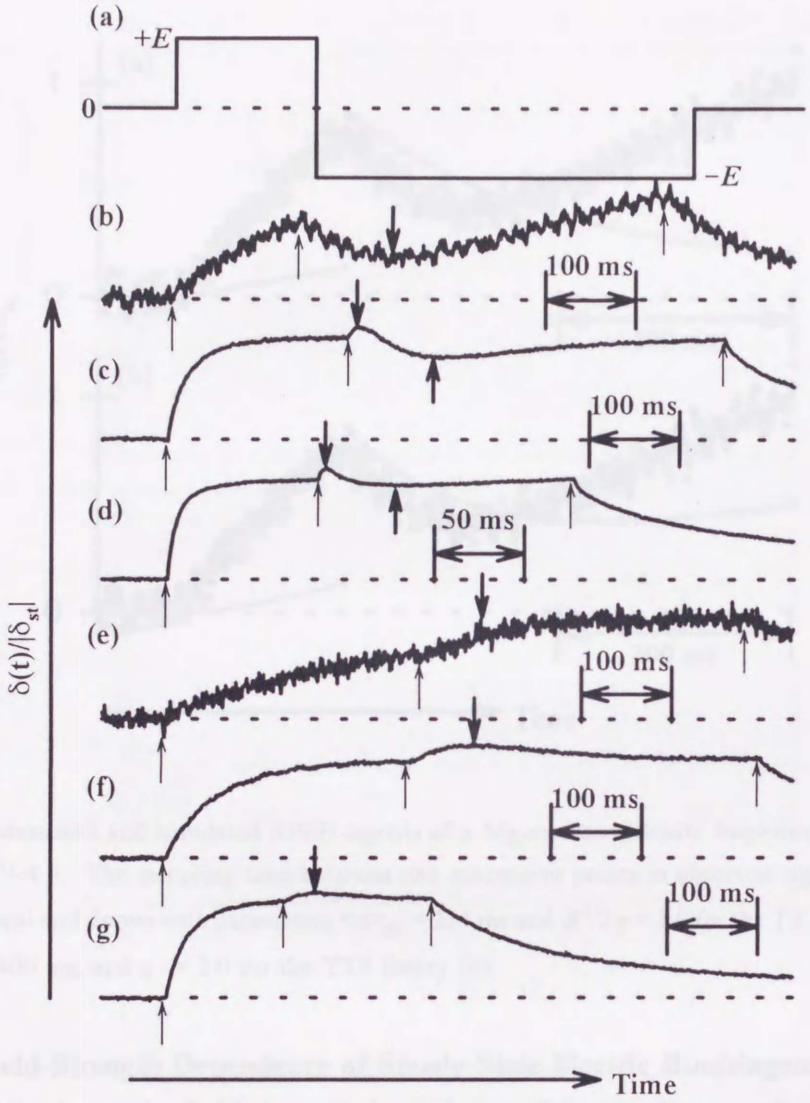

Figure V-4-1. Normalized RPEB signals of Mg-montmorillonite suspensions. (a): schematic reversing-pulse pattern. (b-d): RPEB signals measured at c = 0.065 gdm^{-3} and Is = 0; (e-g): c = 0.065 gdm^{-3} and Is = 0.0001. Applied field strength E in Vcm^{-1} and reduced saturated steady-state electric birefringence δ_{st}/cd in degdm^{3}g^{-1}cm^{-1}: 14 and 0.09 (b); 94.6 and 8.63 (c); 238 and 14.1 (d); 13 and 0.48 (e); 102 and 11.7 (f); 236 and 22.2 (g). Thin arrows indicate points of field switching, while thick arrows show either hump or dip. Note the change of time scale of signals in parts.

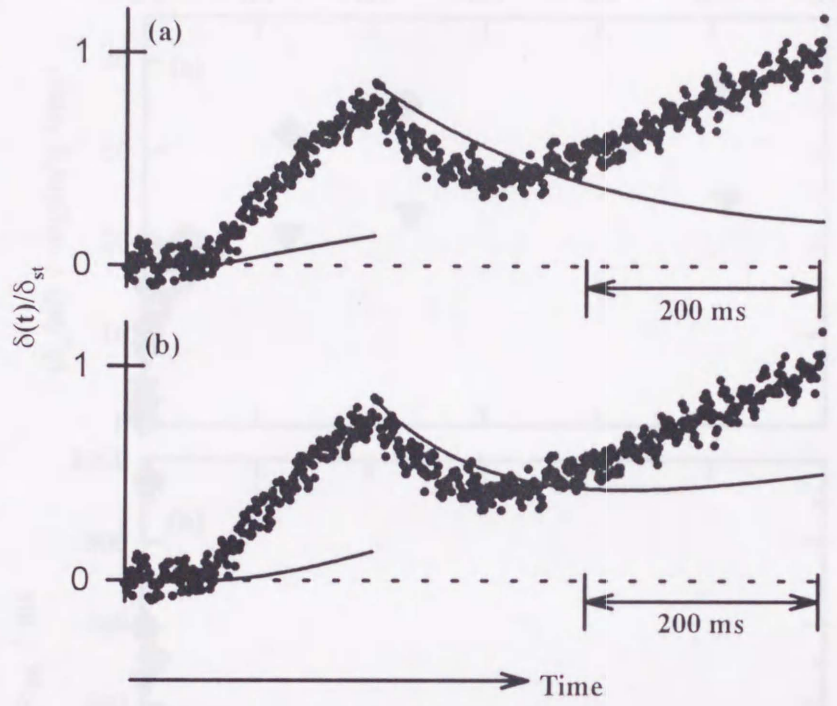

Figure V-4-2. Measured and simulated RPEB signals of a Mg-montmorillonite suspension. Measured signal is (b) in Figure V-4-1. The sampling time between two successive points in observed signal is 0.2 ms. Solid lines are theoretical and drawn with parameters $<\tau>_{EB}$ = 234 ms and $\beta^2/2\gamma$ = 3.0 for the TY theory (a) and $<\tau>_{EB}$ = 234 ms, τ_1 = 400 ms, and q = 2.0 for the YTS theory (b).

V. 4. 2. Field-Strength Dependence of Steady-State Electric Birefringence.

Figure V-4-3a shows the field strength dependence of the steady-state electric birefringence of Mg-montmorillonite suspensions, the sign of which is always positive without sign inversion. At higher magnesium ions, the steady-state electric birefringence is higher at a given field strength, two sets of measured field strength dependence (Figure V-4-3a) are superimposed by multiplying a factor of 1.5. Therefore, with increasing ionic strength, the optical property, but not the electric property, of Mg-montmorillonite is altered. Interestingly, these measured values could not be fitted by any PD-SUSID orientation functions for the disklike particle; therefore, the orientation behavior of Mg-montmorillonite particles cannot be described by the simple PD-SUSID orientation mechanism. The formation of aggregates by added magnesium ions could be responsible for the apparently anomalous field orientation of Mg-montmorillonite particles. Table V-4-1 shows the saturated reduced steady-state electric

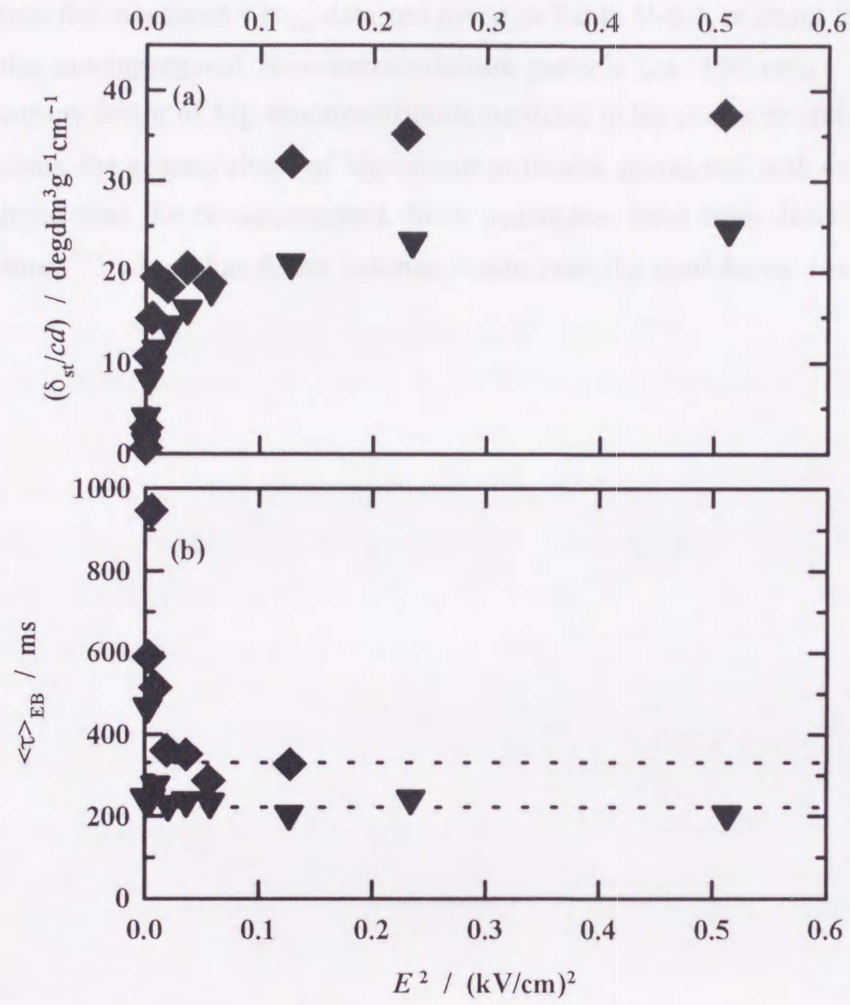

Figure V-4-3. Field-strength dependence of the steady-state electric birefringence (a) and electric birefringence-average rotational relaxation time $<\tau>_{EB}$ (b) of Mg-montmorillonite. (▼) c = 0.065 gdm^{-3} and Is = 0, (◆) c = 0.065 gdm^{-3} and Is = 0.0001.

birefringence, $(\delta_{st}/cd)_{intr}$, evaluated from the data measured at high fields where a gradual leveling-off is apparent. Values of $(\delta_{st}/cd)_{intr}$ are higher at higher ionic strength of magnesium ions, indicating that the optical anisotropy of the Mg-montmorillonite particle increases with increasing ionic strength of the magnesium ions.

V. 4. 3. Field-Strength Dependence of $<\tau>_{EB}$.

Figure V-4-3b shows the field-strength dependence of $<\tau>_{EB}$. Values of $<\tau>_{EB}$ are markedly larger for the Mg-montmorillonite particle than for Na-montmorillonite, indicating that the Mg-

montmorillonite particles no doubt form large aggregates, which grow with an increase in ionic strength. The average diameter $\langle d \rangle_w$ of Mg-montmorillonite particles (ca. 1.2 μm), evaluated from the measured $\langle \tau \rangle_{EB}$ data and given in Table V-4-1, is about four times as large as that of the nonaggregated Na-montmorillonite particle (ca. 300 nm). Judged from the optical anisotropy factor of Mg-montmorillonite particles in the presence and absence of added magnesium ions, the general shape of Mg-montmorillonite aggregates with excess of Mg^{2+} ions is more ordered than the Na-counterpart. Such aggregates have been described as the *book-house structure*,[10,11] which has fewer cavities inside than the *card-house structure*.

References

1. O'Konski, C. T.; Zimm, B. H. *Science* **1950**, *111*, 113.
2. Shah, M. J. *J. Phys. Chem.* **1963**, *67*, 2215.
3. Yoshida, M.; Hayashi, M.; Kikuchi, K.; Watanabe, H. In *Dynamic Behavior of Macromolecules, Colloids, Liquid Crystals and Biological Systems by Optical and Electrooptical Methods*; Hirokawa Publ. Co.: Tokyo, 1989; pp 249—355.
4. Yamagishi, A.; Soma, M. *J. Phys. Chem.* **1981**, *85*, 3090.
5. Yamaoka, K.; Sasai, R.; Ikuta, N. *Chem. Lett.* **1994**, 563.
6. Yamaoka, K.; Tanigawa, M.; Sasai, R. *J. Chem. Phys.* **1994**, *101*, 1625.
7. Sasai, R.; Yamaoka, K. *J. Phys. Chem.* **1995**, *99*, 17754.
8. Sasai, R.; Ikuta, N.; Yamaoka, K. *J. Phys. Chem.* **1996**, *100*, 17269.
9. Tinoco, I., Jr.; Yamaoka, K. *J. Phys. Chem.* **1959**, *63*, 423.
10. *Clay Handbook*; Giho-do Co., Ltd.: Tokyo, 1976.
11. Chernia, Z.; Gill, D.; Yariv, S. *Langmuir* **1994**, *10*, 3988.

— *Chapter VI.* —
Conclusions

In order to study the electrical, optical, and hydrodynamic properties of montmorillonite particles suspended in aqueous media by the RPEB method, the new reversing-pulse generator, which is applicable to the RPEB measurement of large colloidal particles such as clays, was designed and constructed with the following specifications: the maximum applied voltage is limited to 300 V, but the long pulse duration is continuously variable up to 1.2 s. The improved driver amplifier and final discharge units deliver either a single square-wave pulse or double pulses of opposite polarities with very fast time constants to high ionic strength solutions without appreciable voltage sagging. The new pulse generator uses MOS-FET transistors with a high electric-current endurance as the switching element.

To estimate electrical properties of the disk-shaped particle, such as montmorillonite, from RPEB data obtained, two electrooptical theories, which explain the field orientation of particles dispersed in media, were newly derived. One is the transient RPEB theory for the RPEB signal obtained at low fields. By extending the transient electric birefringence theory, proposed by Szabo *et al.* on a basis of the polarization distortion of ion-atmosphere, the new RPEB theory was derived, in which an additional interaction was considered between the applied electric field and the induced electric moment due to the time-independent intrinsic polarizability anisotropy for axially symmetric particle. Another is the new PD-SUSID orientation function for disklike model. This orientation function was derived in order to explain the field strength dependence of the steady-state electric birefringence of disk-shaped montmorillonite particles dispersed in aqueous media. These presently derived theoretical curves were compared with the experimental data of montmorillonite suspension. This comparison shows that these curves reproduce quite well the experimental RPEB data (RPEB signal profile and field strength dependence of steady-state electric birefringence). Therefore, these theoretical curves may be utilized to analyze the experimental electrooptical data not only of montmorillonite but also of other ionized disk-shaped molecules or aggregates in aqueous media and to evaluate the electric, optical, hydrodynamic properties accurately and quantitatively.

In order to clarify the electrical, optical, and hydrodynamic properties of montmorillonite and the effect of particle concentration, ionic strength, and valence of electrolyte on these properties, the RPEB measurement of montmorillonite suspended in aqueous media was performed by using the newly constructed apparatus and derived theories. This study revealed the following facts: (1) The Na-montmorillonite particle possesses no *permanent electric dipole*

moment. Therefore, the observed sign inversion of the steady-state electric birefringence is not due to the *permanent dipole moment* but to the *counterion-induced polarization*. (2) Over the entire range of particle concentrations, Na-montmorillonite particles form no aggregates, but there is the interparticle interaction between the electric double layers of particles in $c > 0.029$ gdm^{-3}. (3) Over the entire of ionic strength range, the sodium ions in aqueous media are primarily adsorbed onto the cation-exchangeable sites of Na-montmorillonite, which forms aggregates with the *card-house structure* at higher ionic strengths. (4) The Mg-montmorillonite particles form aggregates with the *book-house structure*, whose orientation mechanism could be described neither by the YTS theory for transient RPEB signals nor by the PD-SUSID orientation function for the disklike particle. The origin of these anomalies may be attributed qualitatively to complex aggregate formation.

The present study has confirmed that the reversing-pulse electrooptical methods are very useful to characterize the structure and properties of clay particles. These findings give us some fundamental informations for application of clay particles. In the future, the analysis methods of reversing-pulse electric birefringence newly developed in this study will be successfully extended to many colloidal particle system, other than clay particles.

— *Acknowledgments* —

The author wishes to express gratefully his acknowledgment to Professor Emeritus Kiwamu Yamaoka (Hiroshima University) for helpful discussion and encouragement in the course of this study. The author is very grateful to Professor Kunihiko Gekko (Hiroshima University) for his support and valuable suggestions. The author thanks Professors Setsuo Takeno and Ryuji Kitagawa (Hiroshima University) for kindly taking electron micrographs of our samples and valuable advice on the montmorillonite properties. The author is indebted to Professor Kiyohiro Fukudome (Kagoshima University) for useful discussion and suggestions. The author is deeply grateful to Dr. Masato Tanigawa (Joint Research Center for Atom Technology) for his support and help in derivation of the new RPEB theories. The author would like to express sincere thanks to Mr. Natsuki Ikuta (Hiroshima University) for his help and collaboration in design and construction of the new reversing-pulse generator. The author is also very grateful to all coworkers of his laboratory (Hiroshima University) for their helps and collaborations.

公表論文・原著論文等

(1) Reversing-Pulse Electric Birefringence of Disklike Suspensions in the Low Electric Field Region; An Extension of the Ion-Fluctuation Model
(低電場領域での円板状懸濁粒子の反転パルス電気複屈折;イオン揺らぎモデルの拡張)

1 冊

著者 Kiwamu Yamaoka, Masato Tanigawa, and Ryo Sasai
山岡　究、谷川雅人、笹井　亮

(学会誌) The Journal of Chemical Physics, Vol. 101, No. 2, pp. 1625—1631
1994年7月15日出版　(アメリカ物理学会)

(2) Electrooptics in Dispersed Systems. 4. Steady-State Electric Birefringence of Disk-Shaped Particles with Various Electric Moments and the Orientation Function: Case of Montmorillonite in Aqueous Media
(分散系の電気光学４。様々な電気的モーメントをもつ円板状粒子の電気複屈折定常値と配向関数：水分散系におけるモンモリロナイトの場合)

1 冊

著者 Ryo Sasai and Kiwamu Yamaoka
笹井　亮、山岡　究

(学会誌) The Journal of Physical Chemistry, Vol. 99, No. 48, pp. 17754—17762
1995年11月30日出版　(アメリカ化学会)

(3) Reversing-Pulse Electric Birefringence of Montmorillonite Particles Suspended in Aqueous Media. Instrumentation and the Effect of Particle Concentration, Ionic Strength, and Valence of Electrolyte on Field Orientation
(水分散系におけるモンモリロナイト粒子の反転パルス電気複屈折。装置と電場配向への粒子濃度、イオン強度、イオン価の効果)

1 冊

著者 Ryo Sasai, Natsuki Ikuta, and Kiwamu Yamaoka
笹井　亮、育田夏樹、山岡　究

(学会誌) The Journal of Physical Chemistry, Vol. 100, No. 43, pp. 17266—17275
1996年10月24日出版　(アメリカ化学会)

参考論文

(1) Reversing-Pulse Electric Birefringence of Montmorillonite Particles Suspended in Aqueous Media
(水分散系におけるモンモリロナイト粒子の反転パルス電気複屈折)

1 冊

著者 Kiwamu Yamaoka, Ryo Sasai, and Natsuki Ikuta
山岡　究、笹井　亮、育田夏樹

(学会誌) Chemistry Letters, 1994, No. 3, pp. 563—566
1993年3月5日出版　(日本化学会)

(2) Reversing-Pulse Electric Birefringence of β-FeOOH Particles Dispersed in Aqueous Media
(水分散系におけるβ-FeOOH粒子の反転パルス電気複屈折)

1 冊

著者 Viktor Peikov, Ryo Sasai, and Kiwamu Yamaoka
Viktor Peikov, 笹井　亮、山岡　究

(学会誌) Chemistry Letters, 1995, No. 3, pp. 177—178
1995年3月5日出版　(日本化学会)

(3) Low-Field Expressions for Reversing-Pulse Electric Birefringence of Ionized Polyions with Permanent, Ionic, and Electronic Dipole Moments. A Further Extension of the Ion Fluctuation Theory and the Application to Poly(α, L-glutamic acid)
(永久、イオン、電子双極子モーメントをもつ電離性高分子の反転パルス電気複屈折のための低電場域の表式。イオン揺らぎ理論のさらなる拡張とポリ(α, L-グルタミン酸)への適用)

1 冊

著者 Kiwamu Yamaoka, Ryo Sasai, and Kazuhiro Kohno
山岡　究、笹井　亮、河野一博

(学会誌) The Journal of Chemical Physics, Vol. 105, No. 19, pp. 8958—8964
1996年11月15日出版　(アメリカ物理学会)

(4) Electric Birefringnece of Na-Montmorillonite Suspended in Water-Ethanol Mixed Solvent
(水－エタノール混合溶媒中に懸濁されたナトリウム型モンモリロナイトの電気複屈折)

1 冊

著者 Ryo Sasai, Kunihiko Gekko, and Kiwamu Yamaoka
笹井　亮、月向邦彦、山岡　究

(学会誌) Chemistry Letters　　現在印刷中。
1997年1月11日　受理(日本化学会)